

Thesis Title: Maturation Enhancement of Cardiac Myocytes *In Vitro*:
Development of a loading protocol

Author: S.A.E. Langeslag
1178202

Institute: Delft University of Technology
Faculty of Mechanical, Maritime and Materials Engineering
Department of Biomedical Engineering

Specialization: Tissue Biomechanics and Implants

Examination Board: Prof.dr.ir. F. van Keulen TU Delft
Precision Microsystems Engineering

Dr.ir. J.F.L. Goosen TU Delft
Precision Microsystems Engineering

Prof.dr.ir. R. Dekker TU Delft/Philips Research
Electronic components, Technology and
Materials

Dr. S.R. Braam LUMC
Anatomy and Embryology

This study has been accomplished in cooperation with:



Preface

This document presents the research work done on the development of a loading protocol for realization of enhanced maturity of cardiac myocytes *in vitro*. The presented study is performed in terms of a graduation thesis at the Delft University of Technology, between May 2010 and January 2011. This graduation study is part of a running project performed by the department of Anatomy and Embryology at the Leiden University Medical Centre and the department of Electronic Measurement at Philips Research.

Cytostretch is a multi-disciplinary project; it combines biological, electronic and mechanical knowledge. The project is performed on the area of agreement of cell biology, microelectronics and mechanics. The primary goal of the Cytostretch project is the development of an *in vitro* cell based model for cardiac drug screening purposes. To ensure a properly matured cell based model, mechanical stimulation is introduced. The presented study in this document focuses on the analysis of the introduced mechanical stimulation for the realization of an accurate cell based model.

This thesis project introduced me to many new challenges. The main challenge in which was to define my place in the project. It took some time for me to cope with the various inputs I obtained at the different locations where the project was performed. The project however became very satisfying when my contribution to the project became apparent. Although it took me some time to cope with the variety of inputs, I really enjoyed the multi-disciplinary nature of the project. It gave me the opportunity to gain insight in very interesting fields of science and at the same time gave me the opportunity to contribute to this progressive project.

During the time I spend on the Cytostretch project, I received help from a lot of people, for which I am very grateful. First, I would like to thank Hans Goosen for his everlasting support and time to discuss the project with me. I also would like to thank Fred van Keulen for sharing his broad knowledge in non-linear mechanics with me; it was very pleasant to see his increasing enthusiasm during the study. Thanks also to Ronald Dekker for his impelling enthusiasm about the project, and to Stefan Braam for introducing me into the cell biology, and for his patience with an ignorant technical student in working with living material.

I want to send a special thanks to Patrick van Holst and Harry Jansen with their help in the design and great effort in the realization of the experimental setup. Furthermore, I would like to thank my friends and especially study-mates for their critical view on the project during discussions but most of all for their encouragement and never-ending supply of coffee. I would like to thank my family for their support and interest during my entire study. Finally my boyfriend Rutger, thank you for your great optimism during difficult periods and your way of toning me down when I was stressed, you were of great support.

Stefanie Langeslag
Delft, January 2011

Abstract

One of the major challenges in drug development is the development of a drug-screening model that closely resembles the adult human heart. Currently many drugs are rejected in late stages of development and even withdrawn from the market due to possible cardiac tissue damaging side effects. The corresponding delay in drug development is mainly due to a lack in drug-screening methods, to determine these life-threatening side effects. Cultivation of human cardiac cells *in vitro* could provide such a drug-screening model. Human cardiac muscle cells can be derived from human embryonic stem cells. However, the cardiac muscle cells derived by culturing these human embryonic stem cells into cardiomyocytes (cardiac muscle cells) appear to be immature in relation to cardiac muscle cells taken directly from the adult human body. This immaturity results in a drug-screening model with limited predictability.

The hypothesis of the Cytostretch project, a collaborative project between Leiden University Medical Centre and Philips Research, is that *in vitro* cultured cardiomyocytes subjected to *in vivo* mimicking mechanical stimuli (stretch), will show enhanced maturation. These mature cell cultures provide a good basis for future drug-screening models.

A chip is developed containing a polydimethylsiloxane (PDMS) thin-film as a substrate for cardiomyocyte culturing. A pressure difference is applied to the membrane to obtain a strained membrane, which with anchored cardiomyocytes will result in cardiomyocyte stretch. In order to stretch cardiac myocytes *in vitro*, the development of an *in vivo* mimicking loading protocol is essential. The main goal for the presented study, therefore, is the development of a proper loading protocol for *in vitro* stretching of cardiomyocytes. To reach this goal two study objectives have been defined; investigation of *in vivo* cardiac muscle strain during a normal cardiac cycle and the determination of the PDMS thin-film behavior.

For the determination of the *in vivo* cardiac muscle strain, the left ventricle was modelled mathematically. Assumed was a homogeneous stress distribution along the left ventricular wall, corresponding to a fiber direction course along the wall, consistent with anatomical findings. The relation between left ventricular fiber stress and left ventricle pressure showed to depend mainly on the ratio of cavity volume over wall volume. The left ventricle mechanics can be approximated by:

$$\frac{\sigma_f}{P_{lv}} = 1 + 3 \frac{V_{lv}}{V_w}$$
$$\Delta \varepsilon_f = \frac{1}{3} \Delta \ln \left(1 + 3 \frac{V_{lv}}{V_w} \right)$$

Where σ_f is the left ventricular fiber stress, P_{lv} the left ventricular pressure. V_{lv} is the left ventricular cavity volume, V_w the left ventricular wall volume and $\Delta \varepsilon_f$ the natural fiber strain. The outcome of the mathematical left ventricle model led to the conclusion that the absolute left ventricular fiber strain between end systole (reference volume) and end diastole equals an approximate 14.7% for a healthy adult human heart during normal cardiac cycle.

The PDMS thin-film behavior is modelled analytically with use of classical thin plate mechanics, considering large deformations. The analytical derived outcomes were subsequently compared with numerical and experimental results. The thin-film mechanics appeared to depend mainly on strain due to the extension of the membrane, and only little on strain related to bending. Moreover, the bending strain could be neglected when a pressure of $3kPa$ or more was applied to the membrane.

It was concluded that an analytical model, simply supported around the edges, assuming a linear elastic homogeneous isotropic material, describes the membrane behavior properly. An analytical model with clamped edges was not able to deal with the small radius curvature at the edges due to the great flexibility of the membrane. The displacement field corresponding with the supported boundary condition was consistent with both the numerical approximation and the experimental data.

The results of the analytical model showed that the order of the in plane displacement function u has major influence on the strain outcomes of the model. An in plane displacement function with two terms showed a great strain variation across the membrane, whereas an in plane displacement function containing 5 terms showed a relatively homogeneous strain distribution, consistent with the numerical approximation.

From the results of the analytical model the conclusion was drawn that the pressure-strain behavior of the two membrane configurations (circular and dogbone) differs. In order to obtain a maximum membrane strain of 14.7%, the applied pressure for the dogbone membrane should be 3.725kPa, whereas for the circular membrane the applied pressure should be 5.375kPa. Moreover, on the circular membrane, the transverse strain differs from the radial strain. The radial strain showed to be homogeneously distributed over the entire membrane, resulting in longitudinal equally stretched cardiomyocytes. The transverse strain however decreased from the centre outwards. In the centre section this will result in cells equally stretched longitudinal as well as transverse, however in the edge sections the cells will receive considerably lower stretch in the transverse direction.

Some preliminary testing has been performed in stretching beating areas (clogs of cardiomyocytes) *in vitro* while applying the amount of pressure to the membranes as described above. The first set of experiments showed a maintained cell anchorage to the moving substrate for a long period of time (>120 hours). The second set of experiments showed detachment of the cells at increased pressures up to approximately 7kPa (for both configurations). From this we were able to conclude that a moving substrate has no detrimental impact on cardiomyocyte anchorage. Furthermore, from the detachment of cells at higher pressures than derived we are able to conclude that the pressure protocol will be in a correct range.

The fact that the moving substrate has no detrimental impact on the cardiomyocytes indicates the great opportunities for the Cytostretch project.

Table of Contents

PREFACE	v
ABSTRACT	vii
PART I: INTRODUCTION	1
CHAPTER 1 INTRODUCTION	3
1.1 BIOLOGICAL BACKGROUND	4
1.1.1 CARDIAC TOXICITY	4
1.1.2 PLURIPOTENT HUMAN EMBRYONIC STEM CELLS (hESCs)	5
1.1.3 CARDIOMYOCYTE MATURATION	5
1.2 STRETCHABLE MICROELECTRODE ARRAY	6
1.2.1 POLYDIMETHYLSILOXANE	7
1.2.2 CELL ALIGNMENT	8
1.2.3 CYTOSTRETCH CHIP	10
1.3 STUDY OBJECTIVES	12
PART II: LEFT VENTRICLE MECHANICS	13
CHAPTER 2 LEFT VENTRICULAR FIBER STRAIN	15
2.1 INTRODUCTION	15
2.2 MODELLING THE LEFT VENTRICLE	16
2.2.1 CALCULATIONS FOR A THIN-WALLED STRUCTURE	17
2.2.2 CALCULATIONS FOR A THICK-WALLED STRUCTURE	21
2.2.3 LEFT VENTRICULAR FIBER STRAIN	22
2.3 DISCUSSION	25
2.4 CONCLUSIONS	27
PART III: MEMBRANE MECHANICS	29
CHAPTER 3 THIN PLATE MECHANICS	31
3.1 KINEMATIC EQUATIONS	31
3.1.2 SMALL DEFLECTIONS	32
3.1.3 LARGE DEFLECTIONS	35
3.2 CONSTITUTIVE EQUATIONS	36
3.2.1 SMALL DEFLECTIONS	36
3.2.2 LARGE DEFLECTIONS	37
3.2.3 DERIVATION OF THE ABD-MATRIX	38
3.3 EQUILIBRIUM EQUATIONS	40
3.3.1 POTENTIAL ENERGY	40
3.3.2 EQUILIBRIUM	42

CHAPTER 4	MEMBRANE LOAD-DEFLECTION	43
4.1	MEMBRANE DISPLACEMENT FIELD	43
4.1.1	DOGBONE CONFIGURATION	43
4.1.2	CIRCULAR CONFIGURATION	47
4.2	MEMBRANE POTENTIAL ENERGY	49
4.2.1	DOGBONE CONFIGURATION	49
4.2.2	CIRCULAR CONFIGURATION	51
4.3	MEMBRANE DEFLECTION	54
4.3.1	DOGBONE CONFIGURATION	54
4.3.2	CIRCULAR CONFIGURATION	55
4.4	MEMBRANE STRAIN	58
4.4.1	DOGBONE CONFIGURATION	58
4.4.2	CIRCULAR CONFIGURATION	66
4.5	EXPERIMENTAL VERIFICATION	74
4.5.1	MATERIALS AND METHODS	74
4.5.2	DEFLECTION w	75
4.5.3	DISPLACEMENT U	77
4.6	DISCUSSION	80
4.6.1	EXPERIMENTAL VERIFICATION	80
4.6.2	GROOVE STRAIN	81
4.7	CONCLUSIONS	85
PART IV: PRELIMINARY EXPERIMENTS		89
CHAPTER 5	PRELIMINARY EXPERIMENTS	91
5.1	MATERIALS AND METHODS	91
5.1.1	CONSTRUCT PREPARATION	91
5.1.2	EXPERIMENTAL SETUP	91
5.2	RESULTS	94
5.2.1	FIRST SET OF EXPERIMENTS	94
5.2.2	SECOND SET OF EXPERIMENTS	95
5.3	DISCUSSION	97
5.4	CONCLUSIONS	98
5.4.1	EXPERIMENTAL SETUP	98
5.4.2	CARDIAC MYOCYTE RESULTS	99
PART V: CONCLUDING		101
CHAPTER 6	CONCLUSIONS AND RECOMMENDATIONS	103
6.1	CONCLUSIONS	103
6.1.1	LEFT VENTRICLE MECHANICS	103
6.1.2	MEMBRANE MECHANICS	104
6.1.3	PRELIMINARY EXPERIMENTS	105
6.1.4	OVERALL CONCLUSIONS	105
6.2	RECOMMENDATIONS	107
6.2.1	LEFT VENTRICLE MECHANICS	107
6.2.2	MEMBRANE MECHANICS	107
6.2.3	PRELIMINARY EXPERIMENTS	108
6.2.4	OVERALL RECOMMENDATIONS	109

BIBLIOGRAPHY	111
PART VI: APPENDICES	115
APPENDIX 1 NUMERICAL MODEL	117
APPENDIX 2 ADDITIONAL PLATE CALCULATIONS	119
APPENDIX 3 MEMBRANE THICKNESS	121
APPENDIX 4 HYPERELASTICITY	125
APPENDIX 5 CIRCUIT DIAGRAM	127
APPENDIX 6 SENSOR DATA	129

PART I: INTRODUCTION

1 Introduction

Drug development is being significantly delayed due to a lack in functional drug testing models. Cardiac safety risks have become a principal area of concern in this area, since drug side effects influencing the cardiac system can be immediately life threatening. Drugs affecting heart tissue, also called cardiac toxicity, has become the most common cause for drug rejection in late stages of drug development, and even for withdrawal of previously approved drugs from the market.

Cardiac toxicity often results in the development of fast cardiac rhythms that arise within the heart ventricles. The primary risk factor in the development of these so-called arrhythmias is the prolongation of the QT-interval on a surface electrocardiogram (Section 1.1.1).

Drug failures in the past have led to strong regulatory guidelines. To date, new molecular entities must be evaluated in specialized clinical trials (TQT-study) to determine the effect of a drug on the QT-interval, mostly done on human volunteers (HVs). This TQT study serves to assess the potential arrhythmia liability of a drug. Many drugs get rejected, leading to high costs for the pharmaceutical industry, costs that later shift to the consumer by price increments. Not only costs are involved, drug development is dramatically delayed due to this problem, with many patients waiting for a cure.

Animal models used for drug screening have constraint reliability, as human differs from animal physiology.

A major challenge in drug development is the development of an early drug-screening model that closely resembles the human heart. Cultivation of human cardiac cells *in vitro* could provide such a drug-screening model. *In vitro* cultivation of human cardiac cells shows not only potential for drug screening related to cardiac toxicity, but could also provide disease models for specific drug testing. Nowadays human cardiac cells are derived from human embryonic stem cells. However, the cardiac muscle cells derived by culturing these human embryonic stem cells into cardiomyocytes appear to be immature as compared to cardiac muscle cells taken directly from the human body. Cardiomyocytes cultured using conventional methods do not align and remain poorly differentiated[1]. This immaturity will result in a drug-screening model, which has a limited predictability of adverse drug reactions in the human body.

In this field directing the cells to establish the physiological structure and function of mature human heart tissue needs to be explored. The goal of the research project Cytostretch is to develop a method for this further maturation of cardiomyocytes *in vitro*. Cytostretch is a chip consisting of a stretchable thin film for the stretching of cardiomyocytes. The hypothesis of the project is that cardiomyocytes subjected to stimuli comparable to *in vivo* stimuli, like cell stretch, will show enhanced maturation.

The aim of this study is the development of a loading protocol for the stretching of cardiac myocytes *in vitro*.

This report is subdivided into five parts, this first introductory part, consists of one chapter which will provide the reader some background information, Section 1.1 provides an introduction into the biological background of the project. The matter of cardiac toxicity will be discussed. Furthermore, the potential of human embryonic stem cells for the application of drug-screening models will be presented, and the problem with cardiomyocyte maturation will be discussed. In Section 1.2 the project description will be presented, the introduction of a stretchable MicroElectrode array will be discussed with the current design considerations. Finally Section 1.3 contains the objectives of this study.

PART II discusses the left ventricle mechanics, for the establishment of left ventricular fiber strain *in vivo*. A mathematical model will be introduced to determine the left ventricular fiber stress, and its relating strain. PART III will provide the reader a detailed insight in the currently produces membranes for *in vitro* testing. In Chapter 3 the mechanics of a thin plate will be discussed for the application to the Cytostretch membranes discussed in Chapter 4.

In addition to the determination of an *in vitro* loading protocol, preliminary experiments on the straining of cardiomyocytes *in vitro* have been performed with use of a developed measurement setup. PART IV presents these preliminary experiments, including information about the used measurement setup and the first test results. Finally, conclusions and recommendations relating the entire process are presented in PART V, containing a chapter with a concluding section (Section 6.1), and a section of recommendations for future work (Section 6.2).

1.1 Biological background

Stem cells have the capability to differentiate into specialized cells in the human body. Adult stem cells are called multipotent; they are able to differentiate into limited types of specialized cells. In contrary, embryonic stem cells (ESCs) derived from early embryos have the capacity to differentiate into any of the three germ layers in the body (pluripotent). The ability exists to cultivate contracting cardiomyocytes from embryonic stem cells, under defined conditions. These contracting outgrowths show potential for early drug-screening purposes.

1.1.1 Cardiac toxicity

Cardiac toxicity often results in the development of fast cardiac rhythms that arise within the heart ventricles. The primary risk factor for the development of these so-called arrhythmias is the prolongation of the QT-interval on a surface electrocardiogram (ECG). The QT-interval denotes the period between the beginning of the Q- and the end of the T-wave, and represents the depolarization and repolarization of the ventricles; the total duration of electrical ventricular activity (Figure 1).

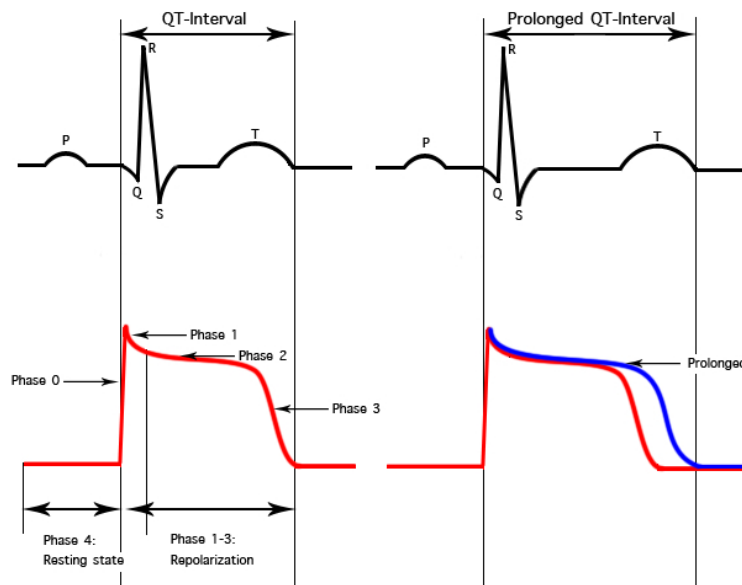


Figure 1: ECG (top) and action potential (bottom) of normal and prolonged QT-interval. Adverse drug effects can cause these prolonged QT-intervals, which result in fast cardiac rhythms. The blue line indicates a prolonged QT-interval, which becomes apparent in the action potential.

Prolongation of the QT-interval can be most easily observed by measurement of the action potential (Figure 1, bottom). The action potential relates to a voltage difference that exists across the cell membrane, resulting from an interaction between ion-pumps and ion-channels in the cell membrane. During contraction, cardiac cells undergo a fast rising and falling in this membrane potential due to ion currents, for a joint contraction of the heart. The prolongation of the QT-interval becomes apparent in the prolongation of the repolarization phase (blue line Figure 1).

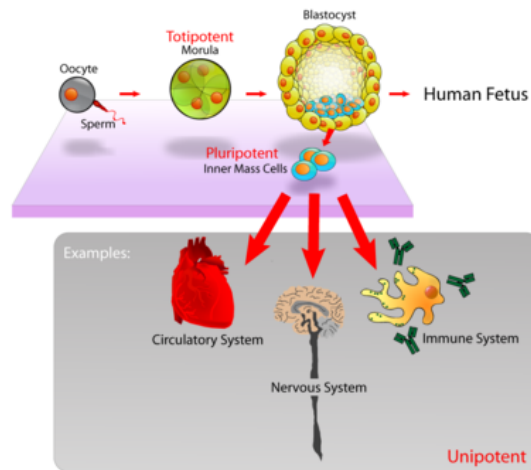


Figure 2: Pluripotent embryonic stem cells can differentiate into any of the 3 germ layers; endoderm, mesoderm and ectoderm. These cells are harvested from the inner cell mass of an early blastocyst, and can thus differentiate into cardiac muscle cells.



Figure 3: Contracting outgrowth plated on a glass substrate. Notice the stressed fibers providing cell attachment to the substrate.

1.1.2 Pluripotent Human Embryonic Stem Cells (hESCs)

Human embryonic stem cells can be cultured indefinitely, and have the ability to differentiate into any of the three germ layers; endoderm (gastrointestinal tract, lungs), mesoderm (muscle cells, bone, blood) or ectoderm (epidermis, neural cells) (Figure 2). This pluripotency makes them ultimately suitable for these *in vitro* models for drug screening purposes.

The pluripotent cells are harvested from the inner cell mass of the early blastocyst in the development of the embryo (Figure 2). The human embryonic stem cells are then co-cultured with fibroblasts (inactivated for cell division); to keep the cells in their undifferentiated pluripotent state. The fibroblasts achieve this through the secretion of growth factors and synthesis of an extra cellular matrix as framework[2].

For the differentiation of the embryonic stem cells into cardiomyocytes (cardiac muscle cells) previous experiments have mostly relied on spontaneous differentiation to form contracting outgrowths. A range of different cardiomyocyte cell types can be obtained from these differentiation processes, including nodal-like, atrial-like and ventricular-like cells (Figure 3). For the enrichment and purification of these different populations of cardiomyocytes, the use of certain cytokines or growth factors is used.

1.1.3 Cardiomyocyte maturation

MicroElectrode Array's (MEA) have been used in the past to perform early drug screening on the *in vitro* cultured contracting outgrowths. These MEA's consist of a glass substrate embedded with titanium-nitride electrodes for measuring the cells' membrane potentials. On the glass substrate a culturing ring is positioning for containing nutritious fluid. The reliability of these models however shows not to be significantly higher than the reliability of animal models, mainly due to poor maturation of the cardiomyocytes in *in vitro* cultures.

The *in vitro* cultured contracting outgrowths show stressed plated cardiomyocytes on the glass substrates (Figure 3). The substrate lacks in elasticity to comfort cardiomyocytes *in*

vitro. Furthermore, the substrate lacks in mechanical stimuli, a probable cue in cardiac maturation.

Analysis of ultra-structural cell organization, electrophysiology, and gene- and protein expression has led to the conclusion that the derived cardiomyocytes derived from human embryonic stem cells are relatively immature compared to adult human cardiomyocytes.

The probable cause for the poor maturation of cardiomyocytes in *in vitro* cultures is the lack in normal *in vivo* environmental input. The cardiomyocytes appear to need external stimuli for further maturation. For further maturation processes, the cultivation should mimic the heart and its environment.

Cardiomyocytes in the developing heart are exposed to several stimuli, chemical stimuli as well as mechanical stimuli. Although the exact nature and effects of these stimuli are not fully known, it is thought that chemical stimuli include probable stimuli for cardiomyocyte alignment, resulting in *in vivo* resembling anisotropic contraction. Mechanical environmental stimuli among others include elastic, moving foundations and with that mechanical stretch due to the extension of the foundation.

Earlier studies have showed that induction and sensing of stretch appears to be crucial for proper development and assembly of sarcomeres. Cardiac constructs exposed to cyclic stretch assembled myofibrils with compact, aligned sarcomeres. Sarcomeres are the smallest functional unit of a myofibril (muscle bundle), repeating units along the length of a myofibril. Serial alignment and parallel bundling of sarcomeres is required for temporal and spatial synchronization required for uniform contraction[3].

However, not only aligned and bundled sarcomeres indicate matured cardiomyocytes. Maturation progression can be assessed at four levels: molecular, cellular, ultra-structural and functional. On molecular level, the progression can be seen from the distribution of cardiac proteins. For example a high doze of contractile proteins (actin, myosin) indicates high contraction density. On cellular level, the cell number, viability of the cells and the metabolism indicate stages in maturation[1].

Ultra-structural, maturation can be assessed among others by morphology of cells and nuclei, development and volume fractions of the earlier mentioned sarcomeres, development and frequency of mitochondria. The mitochondria are the cells energy supply; they generate most of the cell's supply of adenosine triphosphate (ATP), used as a source of chemical energy. A high mitochondrial density indicates a high energy-usage, relating to active contracting cells. Moreover, aligned, elongated multinucleated cells are indicative of cell maturation.

On functional level we can assess the maturation by amplitude of contractions, maximum capture rate and transmembrane potentials. With maximum capture rate the maximum pacing rate for synchronous construct contractions is meant. A high maximum capture rate indicates functional coupling between cells[1].

1.2 Stretchable MicroElectrode Array

The development of a stretchable MicroElectrode Array could provide a solution for further maturation and functional analysis of cardiomyocytes *in vitro*. A stretchable MicroElectrode Array could accommodate the cells in proper contraction. Furthermore, mechanical straining of the stretchable MicroElectrode Array could enhance cardiomyocyte maturation.

The introduced stretchable MicroElectrode Array consists of a polydimethylsiloxane (PDMS) thin-film spin-coated on a silicon wafer. By wet etching a part of the thin layer of PDMS has been exposed, resulting in a flexible membrane clamped in a rigid silicon surrounding. On the chip a culture container is positioned to contain the culture medium for cell nourishment (Figure 4).

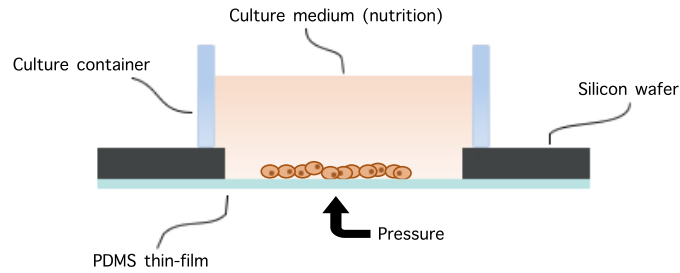


Figure 4: Cross-section of the cystretch device. A membrane is attached to the bottom of a silicon wafer with an etched hole in the centre. On the silicon wafer a culture container is situated for contain nutritious fluid for the cardiomyocytes. The cardiomyocytes anchor themselves on the membrane. Applying pressure to the bottom surface of the membrane will now result in straining the cardiomyocytes.

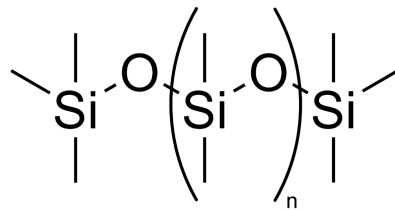


Figure 5: PDMS' repeating unit, creating the polymer's backbone.

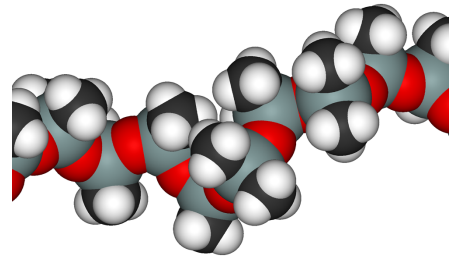
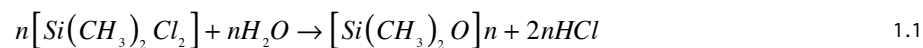


Figure 6: A three-dimensional representation of polydimethylsiloxane, consisting of a Siliconoxide backbone with additional methyl groups.

1.2.1 Polydimethylsiloxane

Cytostretch is based on a spin-coated thin-film flexible silicone rubber, polydimethylsiloxane (PDMS), within a rigid silicone structure. PDMS is used frequently for the production of microfluidic chips, its gas-permeability and biocompatibility makes it very suitable as a substrate for culturing cells. Previous experiments have shown the suitability of PDMS as a substrate for cardiomyocytes[4].

PDMS is a commonly used organosilicon compound, an organic compound containing carbon silicon bonds. PDMS contains repeating $(\text{CH}_3)_2\text{SiO}$ units (Figure 5 & Figure 6), where alteration of the repeating units in the chain and the degree of cross-linking (tying multiple chains together) generates polymers with altering physical properties. Silicon-chlorine bonds are very susceptible to cleavage by water, making that PDMS can be synthesized by hydrolyzing dichloromethylsilane:



Initially, the hydrolysis reaction (Eq. 1.1) generates a silanol $\text{Si}(\text{CH}_3)_2(\text{OH})_2$ which directly, due condensation, loses water and forms a siloxane polymer. The polymer is able to retain some hydroxyl groups since dichloromethylsilane is bifunctional (it contains two chlorines). The hydroxyl groups are able to react with boric acid $\text{B}(\text{OH})_3$, forming Si-O-B linkages. Boric acid on its turn is trifunctional, and can link three polysiloxane chains together, cross-linking the polysiloxane chains. The cross-linking results in a high molecular weight solid elastic polymer with interesting properties[5].

This high molecular weight solid elastic polymer (PDMS) can be produced in colorless, transparent form, very suitable for cell constructs, as the transparency accommodates for the use of conventional microscopy[6]. PDMS is marketed as a kit that consists of a base and a curing agent.

PDMS has a wide range of advantageous properties, making it extremely suitable as stretchable, flexible cell culture substrate[4-8]:

- PDMS has shown great biocompatibility in earlier studies.
- PDMS' gas-permeability ensures gas flow towards cells (non-polar gasses e.g. O₂).
- PDMS shows to be chemically inert.
- PDMS has the ability to conform to the surface of the substrate over a large area, and its deformability makes that it can achieve this conformable contact even on surfaces that are non-planar on micrometer scale.
- PDMS can be released easily from complex and fragile structures, thus easy to release from the mould.
- PDMS is homogeneous, isotropic and shows optical transparency down to 300nm.
- The elasticity modulus of PDMS is low, facilitating a great flexibility for the cardiac myocytes.

We should take in consideration that the Young's modulus of PDMS depends on various factors, many of which are processing parameters. The elasticity modulus strongly depends on the thickness of the membrane, with increasing stiffness with decreasing thickness. Furthermore, the stiffness of the PDMS layer depends on the speed of spin coating. With larger spinning speeds, the PDMS polymer chains get unraveled and aligned, resulting in a higher Young's modulus[9, 10]. These parameters enlarge each other; as result of the higher spin speeds to obtain thinner membranes.

Moreover, the ratio base over curing agent also affects the stiffness of the PDMS thin film[11]. Another method, which can be used when very thin PDMS layers are required, is the addition of thinner to the mixture (lowering the materials viscosity). With additional thinner, the PDMS' thin-film stiffness will decrease[10, 12].

In this study we assume an elasticity modulus of 1MPa, considering a membrane thickness of 25 μ m[13]. However, for a proper description of the thin-film's stiffness properties one should determine the elasticity modulus experimentally. One could assess the stiffness of the membrane by means of an indentation test.

Whereas the elasticity modulus of PDMS is fairly low, the PDMS film will dictate the stiffness of the cell-film construct, and its structural integrity will not allow the cells to freely contract. The elastic modulus for a PDMS elastomer (thinly spin-coated) is 1MPa, whereas the elastic modulus of for cardiomyocytes is in the range of 30kPa, two orders of magnitude difference[4].

To accumulate the anchorage of the cardiac myocytes on the PDMS thin-film, the PDMS membrane will be coated with fibronectin. Fibronectin is a glycoprotein (plays a role in cell-cell interaction) present in blood, connective tissue and at cell surfaces. Fibronectin has shown that when on a polymer surface, it enhances the attachment of various types of cells to that surface. Fibronectin, through it's binding to collagen and to the cell surface, forms a bridge between the cell and its surrounding matrix, with that participating in the formation of the extracellular matrix in tissues[14].

1.2.2 Cell alignment

Although alignment and parallel bundling of sarcomeres mark cardiomyocyte maturation, the alignment of cardiomyocytes can also accommodate for the enhancement of maturation. Cardiomyocyte alignment provides anisotropic synchronous contraction seen in mature cardiac muscle, accommodating contraction coupling. Moreover, the alignment of the cardiac muscle cells is essential for directional stretching, and with that accurate modeling of the cardiomyocyte behavior.

The most used method in cell patterning is extracellular matrix protein patterning, guiding the direction of cell attachment. Fibronectin is a commonly used protein for this so called microcontact printing (Figure 7). A polymer (commonly PDMS) stamp is created containing the desired pattern, consequently depositing the fibronectin pattern on the substrate. Although microcontact printing results in patterns with a lateral resolution down to 1 μ m, and

the process is very cost effective to create chemically micropatterned surfaces for cell biological applications, it is very labour intensive and not suitable for large scale cardiomyocyte alignment. Furthermore, the difficulty arises to exactly align the stamp in the desired direction.

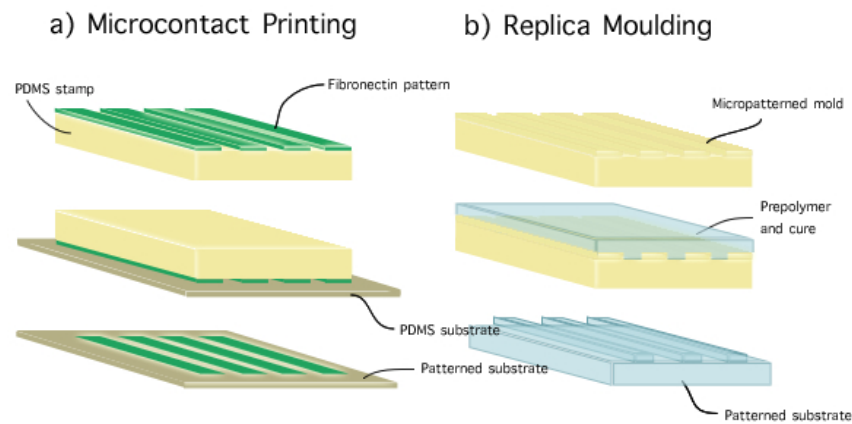


Figure 7: Cell patterning methods; Microcontact printing is the most commonly used method for cell alignment. Fibronectin is stamped onto the substrate for easy anchorage of the cells. However, microcontact printing is very labour intensive and exact alignment with the small substrate fairly difficult. Currently replica moulding is used; grooves are created by using a mold, cells are subsequently able to align along these grooves as they react to geometrical cues.

Previous studies have shown that cardiomyocytes react to geometrical cues[3, 15]. Shapes were engineered by introducing adhesive islands (coated with fibronectin). The cells spread to take on the shape of the islands. Cells on round islands extended cell processes at random points along their circumference. Cells on square islands seemed to preferentially extend these processes from their corners[15]. Physical constraint of cells within square islands may cause them to focus cytoskeleton-based tractional forces in their corners. The actin-containing stress fibers (mechanically supporting the cells) of the cells preferentially align diagonally over the squared islands. The mechanism by which cells redirect the position of their leading edge appears to involve a change in mechanical stress distributions in the cells. A relative increase in cell distortion (stretch) along the diagonal may promote actin filament formation, in a manner analogous to the way in which actin bundles align with the applied stress field when cells are exposed to mechanical stress.

Cells apparently want to generate tension to support mechanical stiffening in the cytoskeleton. Therefore, we should also be able to guide cell alignment by geometrical cues. In the PDMS membrane, grooves are formed by replica moulding for topological alignment of the cardiomyocytes, guiding the attachment of the cells (Figure 7). Replica moulding has the big advantage that it can be incorporated in the process-flow of the Cytostretch chip in the clean room, making it less labour intensive. Fibronectin coating before cell plating can now be realised by normal coating mechanisms (submersion by a fibronectin containing solution), creating a thin fibronectin layer on the entire membrane.

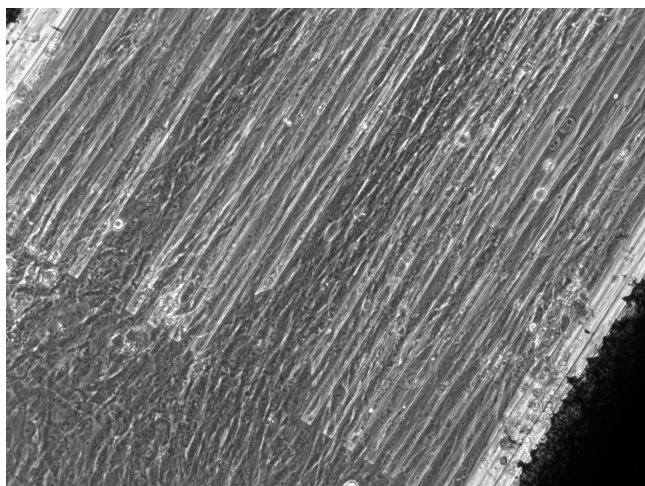


Figure 8: A grooves substrate with plated cardiomyocytes. Notice the alignment of the cardiomyocytes to the replica moulded grooves. The cells clearly react to the geometrical cues. Notice also the poor alignment in the small section where no grooves are situated.

Figure 8 shows the topological alignment of cardiomyocytes on a PDMS membrane. Notice that the alignment in the region containing grooves is in the direction of the grooves, which will introduce anisotropic contraction of the cardiomyocytes.

1.2.3 Cytostretch chip

For the measurement of the cells' membrane potentials, in order to determine arrhythmias during drug testing, the stretchable MicroElectrode Array should contain electrodes (Figure 11). Furthermore, from the cells' membrane potential we are able to determine the stage of maturity. Whereas we need the total substrate to remain flexible, we also need interconnect flexibility.

In a parallel project the insertion of interconnects into the membrane, with electrodes to the surface is assessed, preserving the flexibility of the membrane and maintaining the titanium nitride interconnects' function.

Three membrane configurations have been proposed for cardiomyocyte straining. The first configuration is based on a circular membrane, with grooves running radially. This membrane configuration is designed for multi-axial straining purposes, mimicking *in vivo* loading conditions. The transverse strain of the membrane will result in transverse strain on the cardiomyocytes, while the radial elongation of the membrane will result in a longitudinal cell stretch.

The interconnect design in this configuration is proposed in a helical manner, showing uncoiling with increasing pressure. We should however note, that this helical formed interconnects will dramatically constrict the transverse strain, transforming the multi-axial straining configuration into a uni-axial straining configuration.

The other two chip configurations are based on the same membrane shape. A dogbone membrane shape has been proposed. The inflation of a dogbone shaped membrane will result in a cylindrical centre section, producing uni-axial membrane strain in this section. Elongation (in plane) of the membrane will only exist in the direction of the short axis. This will result in a uni-axial strain on the cardiomyocytes. Grooves are directed in two manners in order to obtain two separate loading conditions. One configuration results in a transverse loading, while on the other a longitudinal load to the cells is applied. With these two design configurations, the effect of transverse and longitudinal stress can be separated for determination of the influence of directed mechanical load (transverse vs. longitudinal).

The interconnect design in the dogbone configuration contains four meander shapes. Because in the central membrane region only stretching over the short axis exists, interconnects are

safe to run parallel to the long axis. An earlier study has proven that both ends of the dogbone membrane contain two low strain pathways, interconnects are guided along these pathways with a superimposed meander shape to further minimize direct interconnect loading[16]. Moreover, all interconnects are isolated in a layer of parylene (Figure 11), further absorbing stress (stress shielding).

Currently two configurations are being processed, the circular membrane and the dogbone membrane with grooves along the major axis (transverse cell loading). The produced chips contain grooves, however, due to further study on interconnects positioning, the current chips lack interconnects for membrane potential measurements. For preliminary testing we are however able to use the currently produced chips. The first tests concern the determination if further maturation occurs when cultured cardiomyocytes are mechanically stimulated. Maturity stage can be determined by many factors (Section 1.1.3), making membrane potential measuring electronics redundant for preliminary testing. During this thesis the currently produced configurations are considered, the circular and the long axis grooved dogbone chip without electrodes and interconnects.

Figure 11 shows the proposed Cytostretch system, containing a flexible PDMS membrane attached to a rigid silicon wafer chip. To the silicon's upper side a transparent culture medium container is attached. Cut-outs are created in the upper side of the membrane for the topological alignment of the cardiomyocytes. In between the cut-outs the interconnects are situated, wrapped in isolating parylene, which lead to electrodes with parylene openings to the surface. The interconnect ends lead to a bond pad, connected to a circuit board for membrane potential readout.

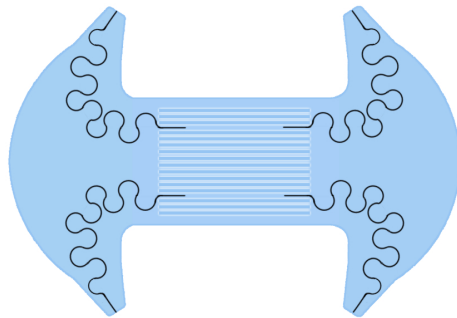


Figure 9: Dogbone configuration Cytostretch for an approached uni-axial loading condition, here a transverse loading condition will be applied, cells will presumably align with the grooves.

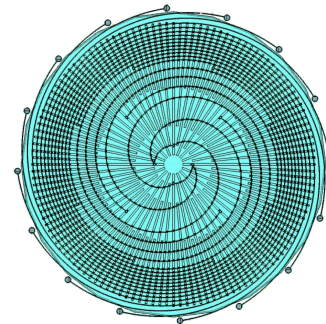


Figure 10: Circular configuration Cytostretch for a multi-axial loading condition. The grooves run radial, in order to obtain transverse and longitudinal strain.

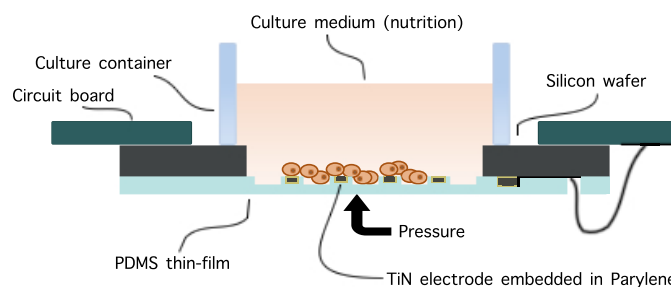


Figure 11: Proposed Cytostretch system, containing of a chip including membrane with grooves, interconnects and electrodes (titanium-nitride embedded in parylene) and a culture container for culture medium. The electrical signals are transferred via a bondpad towards a circuit board for electrical readout.

1.3 Study objectives

Cytostretch development is a collaborative project between Philips Research, Eindhoven and the Leiden University Medical Center in Leiden. A research group situated at Philips, Eindhoven, performs research on the development of the Cytostretch chip. The cell biology of the cardiac myocytes with focus on cultivation protocols is studied at the LUMC in Leiden.

The integration of the cultivation protocol into the Cytostretch chip development has yet to be made. Measurement of stretched cardiac myocytes *in vitro* is one of the main goals of the Cytostretch project. However, in order to stretch cardiac myocytes *in vitro* the development of an *in vivo* mimicking loading protocol is essential.

The main goal of this thesis is the discussion of a proper loading protocol for the straining of cardiomyocytes *in vitro*. For the development of a proper cardiomyocyte loading, two main objectives have to be fulfilled:

- The first objective of this study is to gain insight in the strain cardiomyocytes have to endure *in vivo*.
- The second objective of this study is to determine the membrane behavior of both Cytostretch configurations, in order to determine how the amount of applied pressure relates to membrane stretch.

For the determination of *in vivo* cardiomyocyte strain, use is made of a mathematical model in the calculation of left ventricular mechanics. Moreover, for the determination of the Cytostretch membrane behavior an analytical model is introduced.

PART II: LEFT VENTRICLE MECHANICS

2 Left Ventricular Fiber Strain

This chapter describes the strain in the fibers of the left ventricle of an adult human heart. The left ventricular fiber strain is simulated by a rotationally symmetric thick-walled mathematical model considering an anisotropic fluid-fiber continuum subjected to large deformations.

The Analytical left ventricular Model results in a predicted strain in fiber direction analogous with the strain in human cardiac fibers during a normal cardiac cycle. Together with the membrane strain behavior described in Chapter 4, these predicted strain values lead to a natural pressure protocol for the experimental setup.

2.1 Introduction

In vivo measurement of the left ventricular wall mechanics has proven to be very difficult. Transducers inserted into the wall to measure stress, damage the tissue at the site of measuring [17].

When modelling the left ventricle in a mathematical manner to describe wall mechanics, simplifications concerning the characteristics of the ventricle are required. Each simplification is a compromise between accuracy and calculation time.

Initially, most calculations on the left ventricular wall are based on the classical theory of elasticity [18, 19] using Hooke's law or the Laplace Law. Laplace's Law relates the pressure difference across a membrane to its curvature and surface tension, but is only valid for thin walled structures, and Hooke's law assumes that elastic deformations are small, i.e., less than approximately 5% of their initial unloaded dimensions. It is well known, however, that deformation of the left ventricular wall material during a normal cardiac cycle is not small, and the left ventricular wall thickness can neither be assumed small. It is therefore apparent that the classical theory is not appropriate to describe the mechanical behavior of the left ventricular wall.

Wong and Rautaharju [20] and Falsetti [21] proposed thick-walled models of the left ventricle, considering an ellipsoidal shell with the myocardium assumed as passive material. They assumed deformation as a result of intraventricular pressure only. The entire cardiac cycle was analyzed, and stress components were computed according to the coordinate system dictated by total ventricular geometry rather than according to fiber orientations and sarcomere lengths at various wall layers. Wong later [22] proposed a similar computational method, however now considering a computed sarcomere distribution across the ventricular wall. Both models proposed by Wong still made of the linear elasticity theory, assuming small deformations.

Mirsky [23] was the first to compute ventricular stresses based on large deformation theory. Mirsky first assumed the geometry of the left ventricle to be spherical, and found that the tangential stress at the endocardial surface was ten times as high as obtained using small deformations elasticity theory. Several different shapes of the left ventricle have been considered. Janz [24] developed formulas for estimating local average circumferential stress in spherical, cylindrical, conical and ellipsoidal shapes, but again considered the classical elasticity theory. Chaudry *et al.* [25-27] combined the work of the above researchers and developed models for the calculation of stresses and strains using spherical and conical thick-walled shells applying large deformation analysis. He concluded that a truncated conical model

leads to more realistic results than the spherical model and enables one to evaluate stresses and strains from base to apex instead of only at the equatorial region.

Taber [28] approximated the ventricle as a thick-walled cylinder consisting of incompressible laminae of equal thickness, which resulted in a non-linear shell theory to describe the stresses in the left ventricular wall (accuracy dropped with increasing lamina thickness).

The researchers mentioned above, however, all assumed the left ventricular wall material isotropic and homogeneous. One can imagine that this is an assumption, which may have a big impact on the results, as the left ventricular heart wall consists of a fiber structure embedded in an incompressible fluidic material. According to Feit [29] a realistic model of the left ventricle should take into account the known anatomic structure of the left ventricular wall and the key mechanical properties of its muscle fibers. Feit developed a model that consists of a hollow cylindrical mass of muscle bound between two plates of negligible mass that takes into account non-negligible wall thickness, incompressibility, finite deformation, nonlinear elastic effects and the known fiber architecture. The muscle fibers follow a helical course in the wall, with a fiber angle (i.e. helical pitch) changing smoothly across the wall [30, 31]

Feit uses a simplification for the model; it accommodates for an increase in chamber volume without undergoing twisting. To realise this zero rotation, Feit assumes a second system containing fibers with an opposite helical pitch angle. However, such a counter system seems not to exist, and twisting of the apex with respect to the base during ejection cannot be eliminated [32].

The model used here for the calculation of left ventricular fiber strain is based on the models of Arts *et al.* [32-35] and Chadwick [36-38]. These researchers determine the relation between left ventricular pressure and left ventricular volume on the one hand and the transmural distribution of sarcomere length and fiber stress on the other. Chadwick describes the compact region of the left ventricle by a cylindrical geometry including torsion. For simplification reasons Chadwick neglects non-linear effects, such as finite deformation and a strain-dependent stiffness. Transmural stress and strain distributions are obtained with use of a quasi-static equilibrium. The upper surface must be in force equilibrium and moment equilibrium, integration over the total left ventricular wall results in a stress distribution. Arts *et al.* [32], describes the transmural stress and strain in a similar manner. They simulated the left ventricle by a thick-walled cylinder composed of 8 concentric shells, with the advantage that each shell has a constant fiber angle. Again transmural distributions were obtained by force and moment equilibrium.

2.2 Modelling the left ventricle

The compact region of the left ventricle has a shape, which can be roughly described as a thick-walled, truncated, prolate ellipsoid. In a section through the wall (Figure 12) the projection of the direction field onto a meridional plane defines a continuum of nested closed curves. These curves are then rotated about the axis of revolution, defining a system of closed toroidal surfaces. A fiber path lies on one of these toroids and winds around its surface in a helical manner. This is all based on a computation of Chadwick [37], who utilized Streeter's [30] measurements and assumed axial symmetry. Muscle fiber orientation in the left ventricular wall is quantified by the helix fiber angle, defined as the angle between the muscle fiber direction and the local circumferential direction. The helical pitch angle runs from a negative angle in the outer layers (epicardium) to a positive angle in the inner layers (endocardium).

The shape of the modelled ventricular wall is an important factor in resulting stress contribution in the wall [39]. Furthermore, when introducing anisotropic properties in the thick wall, the transmural course of fiber stress appeared to be qualitatively and quantitatively different [32, 37] mainly due to choice of fiber orientation. With a proper choice of the transmural course of fiber orientation close to anatomical findings [30], and assuming torsional deformation, fiber stress was calculated to be homogeneous [35] under a wide variety of loading conditions. Such homogeneity in mechanical load is supported by an

experimental study [40] in which transmural differences in strain along the fiber direction were found to be below the level of significance. In terms of evolution one can imagine this homogeneity of fiber stress, optimization of fiber direction will occur to lower peak stresses, resulting in a fiber direction accommodating a homogeneous stress distribution[41]. The homogeneity of fiber stress simplifies the model and drastically reduces calculation time.

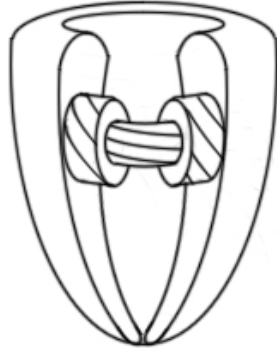


Figure 12: Section through the left ventricular wall, showing a representation of the fiber direction. The fibers run in a helical manner around the ventricle's circumference, with elongating helix toward the centre section of the wall. This results in transmural fiber direction with negative angles at the outer section of the wall towards positive angles at the inner sections of the wall.

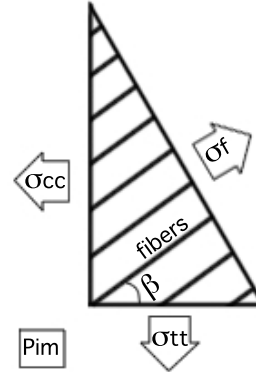


Figure 13: Section of a fiber bundle, indicating the direction of several stress components. Fiber stress in the circumferential direction is indicated with σ_{cc} , in the axial direction, the t-direction with σ_{tt} , and perpendicular to the surface, in the h-direction with σ_{hh} .

Previous numerical approximations have shown that to obtain a homogeneous fiber stress, the transmural course of the helix fiber angle should go from $+60^\circ$ at the endocardium (innermost tissue layer) through $+15^\circ$ in the midwall layers to -60° at the epicardium (outermost tissue layer)(Figure 12)[42].

In the present calculations, myocardial material is considered to be a soft incompressible material, described by a hydrostatic pressure (implying a fluid like behavior of the soft non-fibrous tissue) embedding muscle fibers (fluid-fiber continuum). Fiber stress is assumed homogeneous over the left ventricular wall, and calculated for a rotationally symmetric geometry, thus excluding geometry effects. Fiber strain is calculated for a human left ventricle during a normal cardiac cycle.

2.2.1 Calculations for a thin-walled structure

We first consider the fiber stress in a thin-walled rotationally symmetric chamber. During systole, when fiber stress is high, in the soft bulk of the material hydrostatic pressure is the only stress component (denoted by P_m). For the stress along the fiber direction (σ_1) perpendicular to the fiber direction (σ_2) it holds:

$$\sigma_1 = -P_m + \sigma_f \quad 2.1$$

$$\sigma_2 = -P_m \quad 2.2$$

When we consider this thin-walled structure, the fibers are directed parallel to the surface. Arts *et al.* [32] showed that for the components of the fiber stress in the circumferential direction (σ_{cc}), in the axial direction, t-direction (σ_{tt}), and perpendicular to the surface, h-direction (σ_{hh}) (Figure 13), it holds that:

$$\sigma_{cc} = -P_m + \sigma_f \cos^2 \beta \quad 2.3$$

$$\sigma_{tt} = -P_m + \sigma_f \sin^2 \beta \quad 2.4$$

$$\sigma_{hh} = -P_{im} \quad 2.5$$

From Equations 2.3, 2.4 and 2.5 the fiber stress can be obtained:

$$\sigma_{cc} + \sigma_{tt} = \sigma_{hh} + \sigma_{hh} + \sigma_f \cos^2 \beta + \sigma_f \sin^2 \beta \quad 2.6$$

with (goniometry)

$$\cos^2 \beta + \sin^2 \beta = 1 \quad 2.7$$

results in:

$$\sigma_f = \sigma_{cc} + \sigma_{tt} - 2\sigma_{hh} \quad 2.8$$

Which means that fiber stress can be expressed in terms of (resultant) perpendicular stress components of the material, irrespective of the fiber orientation.

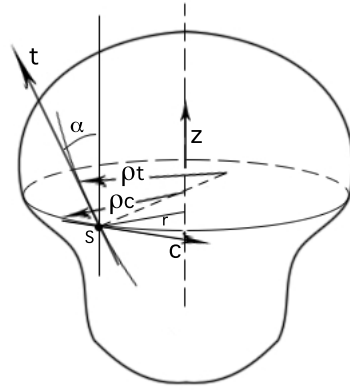


Figure 14: Thin-walled rotationally symmetric shell. The variables r and z are the radial and axial coordinate, c and t are the circumferential and tangential coordinate in point S . ρ_c and ρ_t refer to circumferential and tangential radius of curvature[43].

If we now consider any rotationally symmetric thin-walled chamber (Figure 14) where r is the radial coordinate, c is the circumferential coordinate and z the axial coordinate. The geometry of this chamber is described by a function $r(z)$, where obviously the radius of the shell is a function of the height. In a point P on the surface of the chamber, t is the coordinate tangential to the surface (perpendicular to the c -direction). The symbol α is defined as the angle between the t -direction and the z -direction, furthermore ρ_c and ρ_t represent the radii of curvature along respectively circumferential- and t -direction.

We assume a pressure difference (ΔP) across the thin wall, and take it that the average of cavity pressure and outer pressure is zero; from which follows that σ_{hh} can be neglected. In this case the stress component in axial direction (along the t -coordinate), σ_{tt} delivers a force in z -direction on the cross-sectional area (because of the thin-walled structure, here only an edge) of the area times the force on that area:

$$F_z = 2\pi r h \sigma_{tt} \cos \alpha \quad 2.9$$

Where h represents the wall-thickness.

This force, in terms of equilibrium, must be equal to the pressure difference across the wall acting on the cross-sectional area:

$$F_z = \Delta P \pi r^2 \quad 2.10$$

Resulting in:

$$\sigma_{tt} = \frac{\Delta P r}{2h \cos \alpha} \quad 2.11$$

The angle α depends on the function $r(z)$, and can be described as follows:

$$\cos \alpha = \pm \frac{1}{\sqrt{1 + \tan^2 \alpha}} \quad 2.12$$

and $\tan \alpha$ obviously is the tangent to the curve $r(z)$:

$$\tan \alpha = \frac{dr}{dz} \quad 2.13$$

leading to:

$$\cos \alpha = \frac{1}{\sqrt{1 + \left(\frac{dr}{dz}\right)^2}} = \left[1 + \left(\frac{dr}{dz}\right)^2\right]^{-0.5} \quad 2.14$$

Because we consider a thin-walled structure, we can use Laplace's law. Laplace's law describes the relationship between the transmural pressure difference and the tension and radii of the wall. Laplace's law describes this as an average over the wall, which makes the law only valid for thin-walled structures. Laplace's law states that wall tension can be related to transmural pressure in the following manner:

$$T = \Delta P \left(\frac{1}{r_1} + \frac{1}{r_2} \right)^{-1} \quad 2.15$$

Which means that for the case of the rotationally symmetric shell it holds that:

$$\Delta P = \frac{\sigma_{tt} h}{\rho_t} + \frac{\sigma_{cc} h}{\rho_c} \quad 2.16$$

The radius of curvature at any point x for a curve described by $y=f(x)$ is given by:

$$\rho = \frac{\left[1 + \left(\frac{dy}{dx}\right)^2\right]^{3/2}}{\left|\frac{d^2y}{dx^2}\right|} \quad 2.17$$

[44]

and considering Equation 2.14 above we obtain:

$$\frac{1}{\cos^3 \alpha} = \left[1 + \left(\frac{dr}{dz}\right)^2\right]^{3/2} \quad 2.18$$

From Equation 2.18 it follows that:

$$\rho_t = -\frac{1}{\frac{d^2 r}{dz^2} \cos^3 \alpha} = -\left[\frac{d^2 r}{dz^2} \cos^3 \alpha \right]^{-1} \quad 2.19$$

In which a negative sign is introduced because the radius of curvature increases with decreasing r .

For the radius of curvature in circumferential direction, Meusnier's theorem [45] is used. Meusnier proved that the radius of any inclined section is equal to the radius of curvature of a normal section times the cosine of the angle between the sections:

$$\frac{1}{R_w} = \frac{\cos \theta}{R} \quad 2.20$$

In which R is the radius of the curve, R_w is the radius of curvature of the normal section of the surface in the direction w , and θ is the angle between the normal of the surface and the principal normal of the curve. For the radius of curvature of the thin-walled rotationally symmetric chamber in circumferential direction, Equation 2.20 leads to:

$$\rho_c = \frac{r}{\cos \alpha} \quad 2.21$$

For a cylinder, where r is constant, from Equations 2.14, 2.19 and 2.21 it follows that:

$$\cos \alpha = 1 \quad 2.22$$

thus:

$$\alpha = 0 \quad 2.23$$

and obviously:

$$\rho_t = 0 \quad 2.24$$

$$\rho_c = r \quad 2.25$$

We can now express the thickness h in terms of the function $r(z)$, the pressure and the fiber stress, by eliminating the stress component $\sigma_{\theta\theta}$ in Equation 2.16 by using Equation 2.8 and $\sigma_{\theta\theta} = 0$. Furthermore, we can eliminate σ_{zz} with use of Equation 2.11. Substitution of Equations 2.14, 2.19 and 2.21 leads to the following function for the wall thickness:

$$h = \frac{\Delta \text{Pr}}{2\sigma_f} \left[3 + 3 \left(\frac{dr}{dz} \right)^2 + r \frac{d^2 r}{dz^2} \right] \left[1 + \left(\frac{dr}{dz} \right)^2 \right]^{-1/2} \quad 2.26$$

When assuming the homogeneous distribution of fiber stress (σ), we obtain for the volume of the shell:

$$V_{sh} = \int_{z_{\min}}^{z_{\max}} \frac{2\pi r h}{\cos \alpha} dz \quad 2.27$$

Integrating the cross-sectional area of the wall over the axial length of the rotationally symmetric geometry.

When including the expression for h (Eq. 2.26) we obtain:

$$V_{sh} = \int_{z_{min}}^{z_{max}} \frac{\Delta P \pi r^2}{\sigma_f} \left[3 + 3 \left(\frac{dr}{dz} \right)^2 + r \frac{d^2 r}{dz^2} \right] dz \quad 2.28$$

$$V_{sh} = \frac{3\Delta P}{\sigma_f} \int_{z_{min}}^{z_{max}} \pi r^2 dz + \frac{\pi \Delta P}{\sigma_f} \int_{z_{min}}^{z_{max}} \left[3r^2 \left(\frac{dr}{dz} \right)^2 + r^3 \frac{d^2 r}{dz^2} \right] dz \quad 2.29$$

Notice that the first integral equals the inner cavity volume V , leading to:

$$V_{sh} = \frac{3\Delta P V}{\sigma_f} + \frac{\pi \Delta P}{4\sigma_f} \left\{ \left[\frac{d(r^4)}{dz} \right]_{z_{min}}^{z_{max}} \right\} \quad 2.30$$

From Equation 2.30 the following relation between cavity volume, shell volume, transmural pressure and fiber strain can be obtained:

$$V_{sh} = \frac{3\Delta P(V + V_{err})}{\sigma_f} \quad 2.31$$

In Equation 2.31 V_{err} is defined as the error volume introduced by the last integral term. This error volume equals zero, if at both ends; for $z=z_{max}$ and $z=z_{min}$ the derivative $dr/dz=0$, which is the case if the cavity is closed with a finite radius of curvature, or if it is open at the ends with $dr/dz=0$.

We assume a closed cavity with a finite radius and can now state that, for a rotationally symmetric thin-walled chamber, the following holds:

$$\frac{\Delta P}{\sigma_f} = \frac{V_{sh}}{3V} \quad 2.32$$

Notice that Equation 2.32 implies that the dimensionless ratio of transmural pressure to fiber stress depends solely on the dimensionless ratio of shell volume to cavity volume, whereas the actual shape of the shell is irrelevant as long as it is rotationally symmetric and $dr/dz=0$ at both ends.

2.2.2 Calculations for a thick-walled structure

As we have determined that the left-ventricle cannot be considered a thin-walled structure, we have to convert the formulations to a thick-walled rotationally symmetric chamber.

The relation between fiber stress and left-ventricular cavity pressure (P_v) in a thick-walled rotationally symmetric chamber is found by integration of pressure increments over a sufficient number of thin fitting shells.

Assuming again a homogeneous fiber stress in the thick wall, with fibers directed parallel to the isobaric surfaces, we obtain by using Equation 2.32 inside the wall, for the derivative of the hydrostatic pressure with respect to the enclosed volume:

$$\frac{dP_{im}}{dV} = \frac{-\sigma_f}{3V} \quad 2.33$$

Equation 2.33 contains a negative sign, resulting from the negative pressure gradient towards the outer wall. Integration from the outer wall surface ($V=V_w+V_c$) where the pressure is assumed to be zero, to the inner wall surface ($V=V_c$) results in:

$$\frac{P_{lv}}{\sigma_f} = \frac{1}{3} \ln \left(1 + \frac{V_w}{V_{lv}} \right) \quad 2.34$$

Which can be approximated by:

$$\frac{\sigma_f}{P_{lv}} = 1 + 3 \frac{V_w}{V_w} \quad 2.35$$

Notice that for a very small wall volume:

$$\frac{V_w}{V_{lv}} \ll 1 \quad 2.36$$

Equation 2.34 reduces to Equation 2.32.

The equation for a thick-walled structure, implies that, when assuming that the fibers run parallel to the isobaric surfaces, and the fiber stress being homogeneous, the dimensionless ratio of cavity pressure to fiber stress depends solely on the dimensionless ratio of wall volume to cavity volume, and again appears to be independent of other geometric factors [43].

Several research groups showed similar results despite wide variations in model setups. Regen [46] derived a similar equation between ventricular pressure, wall volume over cavity volume and left-ventricular fiber stress of a prolate spheroid. Arts *et al.* [35] defined a linear expression for left-ventricular fiber stress, using homogeneous fiber stress. Later, Arts *et al.* [34] simulated the left ventricle with mitral valve and right ventricular asymmetry of fiber orientation by a cylindrical model. Also the isotropic models described by Mirsky [23] and Falsetti *et al.* [21], show equal results.

Relative fiber stress increases with increasing radius of curvature and with increasing wall thickness. Geometry of the left-ventricular wall shows to have little effect on the result; the left-ventricular wall stress is mainly determined by the cavity pressure and the relative wall volume to cavity volume. Inhomogeneity shows to have little effect on the stress distribution across the wall, however, when calculating fiber strain, we should take into account that fiber orientation does affect the outcome [32]. Further prove for the orientation of the myofibers to accommodate homogeneity should be obtained.

2.2.3 Left ventricular fiber strain

For the derivation of the left-ventricular fiber strain we use the principle of conservation of energy. The mechanical work generated by the myocardial fibers in the entire wall is equal to the pumping work of the left ventricular chamber:

$$\int_{V_c} \sigma_f \Delta \varepsilon_f dV = P_{lv} \Delta V_{lv} \quad 2.37$$

In Equation 2.37 ε_f represents the natural fiber strain $\left(\ln \left[\frac{l}{l_{ref}} \right] \right)$ and Δ here is associated with a small increment.

Using the earlier stated assumption that fiber stress and strain are homogeneously distributed leads to the following differential form:

$$\frac{d\varepsilon_f}{d\frac{V_{lv}}{V_w}} = \frac{P_{lv}}{\sigma_f} \quad 2.38$$

The natural fiber strain in the left ventricle wall can be obtained by integration of Equation 2.38 with respect to relative cavity volume (ratio cavity volume over wall volume):

$$\frac{V_{lv}}{V_w} \quad 2.39$$

and applied to Equation 2.34. Which results in the following integral:

$$\varepsilon_f = \int_{V_0}^{V_e} \frac{1}{3} \ln \left(1 + \frac{V_w}{V_{lv}} \right) d \frac{V_{lv}}{V_w} \quad 2.40$$

$$\varepsilon_f = \left[\frac{1}{3} \left\{ \ln \left(\frac{V_w}{V_{lv}} + 1 \right) + \ln \left(\frac{V_{lv}}{V_w} \right) + \frac{V_{lv}}{V_w} \ln \left(\frac{V_w}{V_{lv}} + 1 \right) \right\} \right]_{V_0}^{V_e} \quad 2.41$$

When taking reference volume $V_0=0$ Equation 2.41 results in:

$$\varepsilon_{f(V_0=0)} = \frac{1}{3} \left\{ \left(1 + \frac{V_{lv}}{V_w} \right) \ln \left(1 + \frac{V_{lv}}{V_w} \right) - \frac{V_{lv}}{V_w} \ln \left(\frac{V_{lv}}{V_w} \right) \right\} \quad 2.42$$

Similar as for the left ventricular fiber stress, for the left ventricular fiber strain a simple approximation can be made:

$$\Delta\varepsilon_f = \frac{1}{3} \Delta \ln \left(1 + 3 \frac{V_{lv}}{V_w} \right) \quad 2.43$$

In Equation 2.42 zero strain is assumed at end systolic left-ventricular volume, the smallest volume during the normal cardiac cycle. This state is chosen as strain free state, because this is the state we assume the cells are in when the membrane is flat (deflated). This reference state results in positive strain at end diastolic volume (end of filling phase).

One could also take end diastolic left-ventricular volume as strain free state, because at that moment the fibers are fully relaxed (not contracting), and consider a state of negative strain at end systole, thus compression of the fibers. For this purpose either one can be chosen as reference state, as we want to know the relative length change during the cardiac cycle for mimicking purposes.

Initially we want to witness the adaptation of the cardiomyocytes to a normal cardiac cycle, assuming that the cells adjust their contraction pattern to the movement of the membrane, resulting in contraction of cells when the membrane is in a flat state, and assuming cell-relaxation when the membrane is inflated. The value we need to obtain is the absolute strain between end systolic and end diastolic state of the heart, making the choice of reference state, end diastolic or end systolic, irrelevant.

A reference end systolic volume results in a typical reference volume over wall volume ratio in the range between 0.2 and 0.4. For the derivation of the following figures, we have considered a left-ventricular end systolic volume of 63ml and an incompressible wall volume of 200ml [33], leading to a reference volume over wall volume ratio of 0.315.

Thus we assume that:

$$\varepsilon_f = 0 \quad 2.44$$

at

$$V_0 = LVESV = 63ml$$

$$V_w = 200ml$$

resulting in:

$$\frac{V_0}{V_w} = 0.315$$

Left ventricular cavity volume over wall volume typically increases from 0.2 to 0.8 from end systole to end diastole, with end systole volume ratio ranging from 0.2 to 0.4 and end diastole volume ratio ranging from 0.6 to 0.8. Here we consider an end-diastolic volume of 143ml [33], resulting in an end-diastolic relative cavity volume of:

$$\frac{V_{hr}}{V_w} = 0.715$$

The absolute increase in fiber strain with increasing relative cavity volume from 0.315 to 0.715 is plotted in Figure 15.

The absolute strain approximated by this mathematical left-ventricular model considering homogeneous stress distribution, for left-ventricular fibers during a normal human cardiac cycle is 0.147, thus an approximate 14,7%.

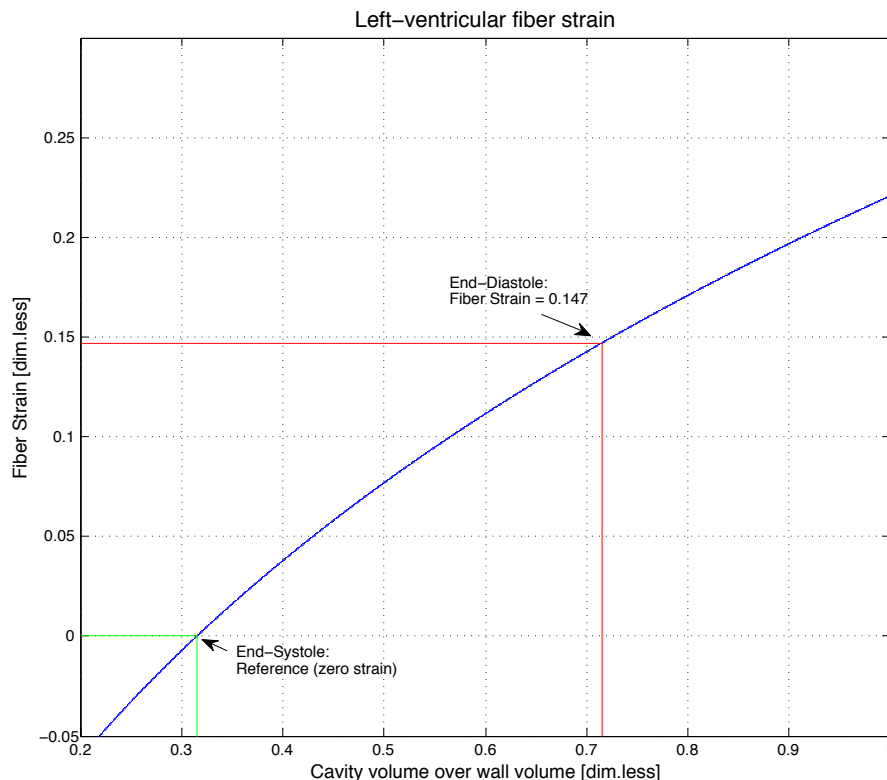


Figure 15: Graph indicating the left ventricular fiber strain as calculated by a rotationally symmetric mathematical model. Assumed is a homogeneous stress (and relating strain), resulting in a unique strain number. End systolic volume is taken as reference, as we want to obtain the absolute strain increase on the muscle fibers in the left ventricle.

2.3 Discussion

Early in the derivation of the left ventricle volume to fiber stress relation for the thin-walled rotationally symmetric chamber, the assumption is made that the average of inner and outer pressure equals zero. From the expressions 2.2 and 2.5 it follows that σ_{th} and P_m both are zero too. When adding a hydrostatic pressure to both the inner and the outer pressure, σ_{th} and P_m both increase.

The outcome of Equation 2.32:

$$\frac{\Delta P}{\sigma_f} = \frac{V_{sh}}{3V} \quad 2.32$$

remains unaffected as the hydrostatic pressure is not able to store deformation energy in incompressible structures [43].

Obviously, the accuracy of Equation 2.32 is essential for the derivation of accurate fiber stress and strain. The error in the equation is expressed by the term V_{err} in Equation 2.31:

$$V_{sh} = \frac{3\Delta P(V + V_{err})}{\sigma_f} \quad 2.31$$

This error term equals zero if the volume is closed with a finite radius or the derivative dr/dz is zero at the boundary. This, however, is not the case at the basal boundary of the left-ventricle, where the basal boundary is open without the derivative dr/dz being zero at that boundary.

The left-ventricle can be seen as a prolate ellipsoid, being cut-off at the upper end, with a long to short axis ratio of 2 or more [43]. If we consider a minor axis of $2R$ and a major to minor axis ratio of a , with the centre at the origin and cut-off at $z=z_{max}$.

A prolate ellipsoid with both short axes a and long axis c can be expressed in Cartesian coordinates in the following manner:

$$\frac{x^2 + y^2}{b^2} + \frac{z^2}{c^2} = 1 \quad [47] \quad 2.45$$

The total volume of the prolate ellipsoid (without a part being cut-off) is defined as:

$$V_{ellipsoid} = \frac{4}{3}\pi b^2 c \quad [48] \quad 2.46$$

In this particular case, with:

$$b = R \quad \text{and} \quad \frac{c}{b} = a \quad \text{leading to} \quad c = Ra \quad 2.47$$

It follows that:

$$V_{ellipsoid} = \frac{4}{3}\pi R^3 a \quad 2.48$$

The volume of an ellipsoidal cap can be defined by:

$$V_{cap} = \pi b^2 \left(\frac{2c}{3} - z_{max} + \frac{z_{max}^3}{3c^2} \right) \quad [49] \quad 2.49$$

With 2.47 it follows that:

$$V_{cap} = \frac{1}{3} \pi a R^3 \left(2 - \frac{3z_{max}}{aR} + \left(\frac{z_{max}}{aR} \right)^3 \right) \quad 2.50$$

The volume of the truncated-ellipsoid can be defined as:

$$V_{truncated_ellipsoid} = V_{ellipsoid} - V_{cap} \quad 2.51$$

and shows to be:

$$V_{truncated_ellipsoid} = \frac{4}{3} \pi R^3 a - \frac{1}{3} \pi a R^3 \left(2 - \frac{3z_{max}}{aR} + \left(\frac{z_{max}}{aR} \right)^3 \right)$$

$$V_{truncated_ellipsoid} = \frac{1}{3} \pi a R^3 \left(2 + \frac{3z_{max}}{aR} - \left(\frac{z_{max}}{aR} \right)^3 \right) \quad 2.52$$

Giving the a volumetric error of:

$$V_{error} = \frac{\pi R^3}{3a} \left(\frac{z_{max}}{aR} - \left(\frac{z_{max}}{aR} \right)^3 \right) \quad 2.53$$

The maximum error occurs when $V_{error}/V_{truncated_ellipsoid}$ is at a maximum, when the tangent to this curve equals zero. This maximum error can be found when we differentiate the ratio $V_{truncated_ellipsoid}/V_{error}$ with respect to z_{max} (for positive z_{max}) and solve the equation for:

$$\frac{dV_{error}}{dV_{truncated_ellipsoid}} = 0$$

resulting in a maximum error at:

$$z_{max} = \frac{1}{2} aR$$

At this maximum error V_{err} (eq. 2.53) becomes:

$$V_{error} = \frac{3}{8} \frac{\pi R^3}{3a} = \frac{\pi R^3}{8a}$$

with $a \geq 2$ (long to short axis ratio of the left ventricle) we obtain:

$$V_{error} \leq \frac{\pi R^3}{16} \quad 2.54$$

We now express the stress in fiber direction in terms of V (simplified volume) and in terms of $V+V_{error}$ (true volume), we obtain with Equation 2.54 for $a \geq 2$, an error of less than 2.78%.

2.4 Conclusions

The left ventricle is assumed to be a rotationally symmetric thick-walled structure. The thick-walled structure is assumed to be build-up out of a, in soft incompressible material embedded, fibrous structure. In the calculations of the fiber stress of the left ventricle, the fiber stress is assumed homogeneous over the entire left ventricle wall.

The assumption of considering the left ventricular fiber stress to be homogeneously distributed can be validated in terms of evolution, the normal heart myofiber structure and geometry adapt, until load is evenly distributed. Furthermore, the fiber direction related to a homogeneous stress distribution corresponds with experimentally derived values [40]. This way we are able to conclude that the left ventricular fiber stress (and corresponding fiber strain) can be approximated by a single value. For the determination of a proper loading protocol for the Cytostretch experiments this is a desired circumstance, as we are able to consider one strain value for the cardiomyocytes.

We can conclude out of the left ventricle calculations, that when assuming a homogeneous stress distribution, the fiber stress to ventricle pressure depends mainly on the ratio of cavity volume over wall volume. Moreover, we are able to conclude that the shape of the left ventricular representation is of minor importance.

The relation between fiber stress and cavity volume leads to the fiber strain with use of the principle of conservation of energy. The conclusion can be made that the left ventricle mechanics can be approximated by the simple approximations of:

$$\frac{\sigma_f}{P_{lv}} = 1 + 3 \frac{V_{lv}}{V_w} \quad 2.35$$

$$\Delta \varepsilon_f = \frac{1}{3} \Delta \ln \left(1 + 3 \frac{V_{lv}}{V_w} \right) \quad 2.43$$

In Equations 2.35 and 2.43, σ_f is the left ventricular fiber stress, P_{lv} the left ventricular pressure. V_{lv} is the left ventricular cavity volume, V_w the left ventricular wall volume and $\Delta \varepsilon_f$ the natural fiber strain.

The calculations of the left ventricular fiber strain in section 2.2.3 leads to the conclusion that for a healthy adult heart the absolute strain between end systole and end diastole equals an approximate 14.7 percent. We should however note that this strain is calculated for a healthy adult heart, for there is much MRI (magnetic resonance imaging) data available containing cavity and wall volume measures. The cardiomyocytes, which are going to be used for the experiments, are however in a much lower maturation stage. From literature however it is assumed that the left ventricular cavity volume over wall volume is in a specific range, valid for any stage of development [33]. It is assumed that the left ventricle wall growth is proportional to the left ventricular cavity increase during development.

Salameh *et al.* [50] uni-axially strained cardiomyocytes at three different values, 5%, 10% and 20%. After 24 hours cyclic mechanical stretch resulted in an increased percentage of cells with an elongated phenotype. They discovered that the percentage of elongated cells was dependent on the intensity of the stretch, 10% and 20% stretch generated significantly more elongated cells than 5% stretch. There was no significant difference in percentage of elongated cells between 10% and 20% stretch. We can thus state that the calculations lead to reasonable fiber strains, applicable for the Cytostretch experiments.

Although the outcome of the calculations seems reasonable, we should take into account that various simplifications have been made in order to describe the mechanics of the left ventricle with reduced calculation time. Biological tissue contains many structural components. In the derivation of the left ventricle mechanics, the material is assumed as a fluid-fiber continuum, as the incompressible fluid like material and muscle fibers are the most distinct components. The next component, which provides consistency of the left ventricle material, is collagen. Collagen exists in the left ventricular wall in a matrix structure, and

could have effect on the left ventricular fiber mechanics. For increased accuracy a fluid-fiber-collagen continuum could be considered in the derivation of the left ventricular strain.

Chadwick *et al.* [38] described the left ventricle mechanics according to the model of Arts *et al.* [32] with an additional collagen matrix, compared the two material models [36-38] and discovered that the contribution of the collagen matrix to the elasticity of the material is critically dependent on the helical pitch angle of the collagen matrix, the effect shows to be maximal when the pitch angle of the collagen matrix equals that of the muscle fiber (Section 2.2). Moreover, the collagen matrix appears to affect stiffness in end systole as well as end diastole (reference is taken at dead volume $45ml$). The elongation between end systole and the reference volume (dead volume) deviates by less than 8 percent from the elongation between end diastole and reference volume when assuming homogeneity in fiber strain over the wall. Incorporation of collagen in the material model could thus result in a lowered fiber strain by maximum 8 percent.

To be on the safe side when stretching the cardiomyocytes we should consider the 14.7 percent as a ceiling value.

PART III : MEMBRANE MECHANICS

3 Thin Plate Mechanics

This chapter describes the mechanical behavior of a thin plate, for the derivation of the load-deflection behavior of both membrane configurations in Chapter 4. The mechanical behavior of a thin plate is generally described in differential equations.

For the derivation of the differential equations in plate mechanics, we apply the classical plate theory. In this theory three relationships are used for the determination of the mechanical behavior. The kinematic equations of the thin plate describe the relation between the plate's displacement and its strain, the constitutive equations describe the relation between strain and tension of the plate, and the relation between tension and load is described by means of equilibrium (Figure 16)[51]. Equilibrium is determined by looking for a stationary point in the potential energy of the system.

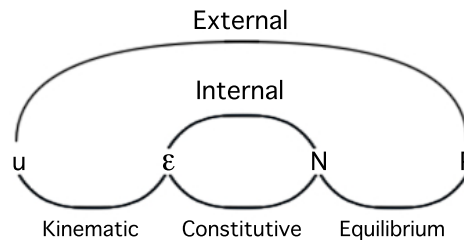


Figure 16: Scheme of three basic equations. The kinematic equations describe the relation between the plate's displacement and strain. The constitutive equations describe the relation between strain and tension and the relation between load and tension is described by means of equilibrium. Externally these equations relate the plate's load to the displacement, internally the equations describe the plate's strain and tension[51].

The first section describes the kinematics of thin plate or shell elements, considering moderate rotations. The kinematics of thin plates can be applied to membranes when considering stretch of the neutral line, due to in-plane displacement additional to pure bending strains, due to perpendicular displacement. Section 3.2 describes the constitutive equations of the plate, which result in a stiffness matrix that can be used easily for the determination of the potential energy of the system. In Section 3.3 the equilibrium equations will be derived finalizing the thin plate characteristics.

The final description between load, tension, strain and displacement will be used in Chapter 4 for the determination of the load-deflection behavior of both membrane configurations.

3.1 Kinematic Equations

The kinematics of a membrane can be derived with use of the classical plate theory; the classical plate theory consists of mathematical descriptions (differential equations) that describe the mechanics of a thin plate (one side much smaller than the two other sides). The kinematics of classical plates relates the plate's displacements to its strains. As mentioned earlier, the total membrane kinematics contains the bending strain as well as the extensional strain, when considering large displacements.

Thus we consider the kinematics of thin plate as follows:

$$\underline{\varepsilon}_{total} = \underline{\varepsilon}_{mid-plane} + z\underline{\kappa} \quad 3.1$$

In Equation 3.1 $\underline{\varepsilon}_{mid-plane}$ is defined as the strain in the middle plane of the plate (neutral line) and $\underline{\kappa}$ is the curvature of the middle plane. Notice that if the in-plane strain is zero (small deflections), that the total strain is defined as:

$$\underline{\varepsilon}_{total} = z\underline{\kappa} \quad 3.2$$

Thus considering pure bending.

3.1.2 Small deflections

In order to derive the strain as relation of displacement for a thin plate, we first consider this pure bending state. Figure 17 represents the bending of a small section of a beam in response to transverse load. The z-direction is here chosen positive downwards.

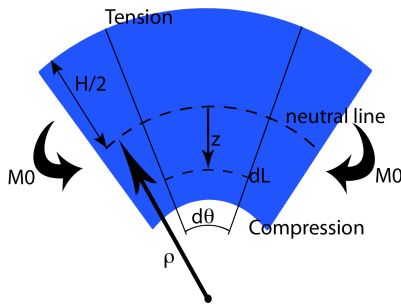


Figure 17: Representation of a small bended section of a beam in response to transverse load. The z-direction is taken positive downwards. In pure bending the middle plane does not undergo extension, in positive z-direction the plane will undergo a compression and in negative z-direction the plane will undergo extension.

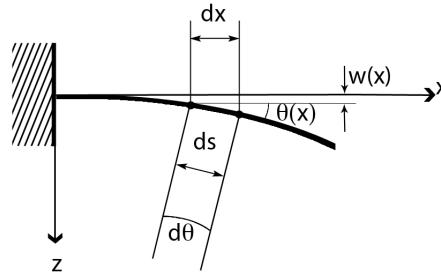


Figure 18: Representation of a part of the neutral axis. ds represents a small part of the neutral axis, and $\theta(x)$ represents the incremental angle.

During pure bending the lateral sides remain plane and rotate about the neutral axes, to remain normal to the deflected middle surface. In pure bending, the middle plane (neutral plane) does not undergo any extension. However the angular segment $d\theta$ varies with the distance from the neutral line, due to the small change in radius of curvature (ρ) from top surface to bottom surface of the beam, as the portions above the neutral line are in tension and the portions below the neutral line in a state of compression. Specifically, the length of an element dL at a distance z from the neutral axis is defined by:

$$dL = (\rho - z)d\theta \quad 3.3$$

At the position of the neutral axis, the corresponding segment is equal to dx , the differential length of the segment when the beam is not bend:

$$dx = \rho d\theta \quad 3.4$$

from which we obtain:

$$dL = dx - \frac{z}{\rho} dx \quad 3.5$$

Since the unbend length of the segment is dx we can derive that the axial strain ϵ_x at position z is:

$$\epsilon_x = \frac{dL - dx}{dx} = \frac{dx - \frac{z}{\rho} dx - dx}{dx} = -\frac{z}{\rho} \quad 3.6$$

We consider only the neutral axis (Figure 18). It follows that an increment of beam length ds along the neutral axis is related to dx by:

$$ds = \frac{dx}{\cos \theta} \quad 3.7$$

And the slope of the neutral axis:

$$\frac{dw}{dx} = \tan \theta \quad 3.8$$

The relation between ds and the incremental angle is, from Equation 3.4:

$$ds = \rho d\theta \quad 3.9$$

If we now use small angle approximation (moderate rotations) for the small increment we obtain:

$$\frac{d\theta}{dx} \approx \frac{1}{\rho} \quad 3.10$$

$$\theta \approx \frac{dw}{dx} \quad 3.11$$

From Equations 3.10 and 3.11 it follows that:

$$\frac{1}{\rho} \approx \frac{d^2w}{dx^2} \quad 3.12$$

The unit elongation in x-direction of a two-dimensional element at distance z (positive downwards) from the normal surface can thus be represented by:

$$\epsilon_x = -\frac{z}{\rho_x} \quad (\epsilon_x = z\kappa_x) \quad 3.13$$

The same holds for the y -direction:

$$\epsilon_y = -\frac{z}{\rho_y} \quad 3.14$$

Equations 3.12, 3.13 and 3.14 lead to:

$$\varepsilon_x = -z \frac{\partial^2 w}{\partial x^2} \quad 3.15$$

$$\varepsilon_y = -z \frac{\partial^2 w}{\partial y^2} \quad 3.16$$

when considering pure bending.

If the directions x and y do not coincide with the principal planes of curvature we will also obtain a shearing strain, due to twisting of the plate. For the couple of shear strains;

$$\varepsilon_{xy} \text{ \& } \varepsilon_{yx}$$

we obtain:

$$\varepsilon_{xy} = 2z \frac{\partial^2 w}{\partial x \partial y} \quad 3.17$$

With Equation 3.2, we can state that the curvatures of a plate are defined as:

$$\kappa_x = -\frac{\partial^2 w}{\partial x^2} \quad 3.18$$

$$\kappa_y = -\frac{\partial^2 w}{\partial y^2} \quad 3.19$$

$$\kappa_{xy} = 2 \frac{\partial^2 w}{\partial x \partial y} \quad 3.20$$

The sign changes in Equations 3.15 to 3.20 are due to the fact that for the moments related to these curvatures (Equations 3.36 - 3.38) the signs are chosen as such that the positive values of these moments are represented by vectors in the positive direction of x and y if the rule of the right hand screw is used [52].

3.1.3 Large deflections

Secondly we assume large deflections, for the determination of the strain due to the stretch of the membrane. Figure 19 represents a segment of the neutral axis in the initial state and the deformed state.

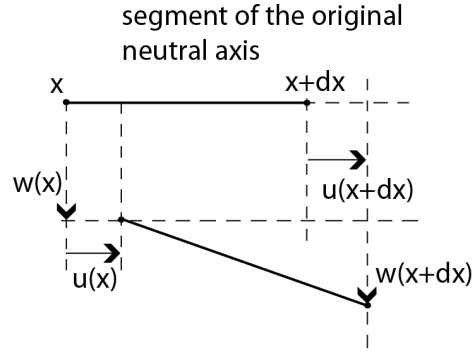


Figure 19: Segment of the neutral axis at initial and at deformed state, the original length of the segment is defined by dx , the displacements in plane and out of plane are defined as respectively u and w .

The original length of the segment is dx , resulting in a deformed length:

$$ds = \sqrt{[dx + u(x+dx) - u(x)]^2 + [w(x+dx) - w(x)]^2} \quad 3.21$$

When considering moderate rotations (small angle approximation for the small increment) we obtain:

$$ds = dx \left[1 + \frac{du}{dx} + \frac{1}{2} \left(\frac{dw}{dx} \right)^2 \right] \quad 3.22$$

$$\varepsilon_x = \frac{ds - dx}{dx} \quad 3.23$$

$$\varepsilon_x = \frac{\partial u}{\partial x} + \frac{1}{2} \left(\frac{\partial w}{\partial x} \right)^2 \quad 3.24$$

and similar:

$$\varepsilon_y = \frac{\partial v}{\partial y} + \frac{1}{2} \left(\frac{\partial w}{\partial y} \right)^2 \quad 3.25$$

Analogous to the case of pure bending; if the directions x and y do not coincide with the principal planes of curvature we will also obtain a shearing strain, due to twisting of the plate. For the couple of shear strains we obtain analogous to Equation 2.29:

$$\varepsilon_{xy} = \frac{\partial u}{\partial y} + \frac{\partial v}{\partial x} + \frac{\partial w}{\partial x} \frac{\partial w}{\partial y} \quad 3.26$$

3.2 Constitutive Equations

Polydimethylsiloxane has the mechanical property that it is a homogeneous isotropic material. In Chapter 4 the following constitutive equations will be applied to the Cytostretch membranes. Therefore, for the derivation of the constitutive equations assumed is a homogeneous isotropic material. Furthermore, for simplification reasons a linear elastic material model is assumed.

3.2.1 Small deflections

Similar to the derivation of the kinematic equations, we first assume small deflections, and focus on the constitutive equations related to bending of the thin plate. To derive the bending equations we primarily look at bending of a rectangular plate due to uniformly distributed moments M_x and M_y , in such a way that the xz and yz planes are the principle planes of the deflection surface (Figure 20).

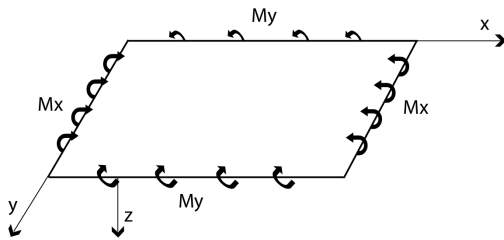


Figure 20: Representation of a rectangular thin plate, bend by uniformly distributed moments M_x and M_y , in such a way that xz and yz are the principle planes of the deflection surface.

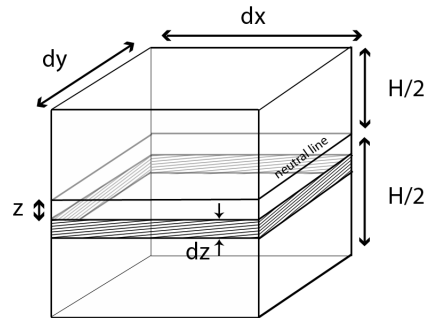


Figure 21: Small element of the rectangular thin plate with dimensions H , dy and dx . A small thickness section dz of this element is considered.

We recall the kinematic Equations 3.15 and 3.16:

$$\varepsilon_x = -z \frac{\partial^2 w}{\partial x^2} \quad 3.15$$

$$\varepsilon_y = -z \frac{\partial^2 w}{\partial y^2} \quad 3.16$$

Hooke's law for linear-elastic isotropic materials states:

$$\varepsilon_x = \frac{\sigma_x}{E} - \frac{\nu \sigma_y}{E} \quad 3.27$$

$$\varepsilon_y = \frac{\sigma_y}{E} - \frac{\nu \sigma_x}{E} = 0 \quad 3.28$$

in which the lateral strain (y -direction) must be zero in order to maintain continuity during bending. Equations 3.27 and 3.28 lead to:

$$\sigma_y = \nu \sigma_x \quad 3.29$$

$$\varepsilon_x = \frac{(1 - \nu^2) \sigma_x}{E} \quad 3.30$$

Now the stress in x -direction becomes:

$$\sigma_x = \frac{E\varepsilon_x}{1-\nu^2} = -\frac{Ez}{1-\nu^2} \frac{d^2w}{dx^2} \quad 3.31$$

The bending moment (for the two dimensional case) can be derived by multiplication of the arm (z) times the stress, integrated over the thickness of the plate:

$$M = \int_{-H/2}^{H/2} \sigma_x z dz = -\int_{-H/2}^{H/2} \frac{Ez^2}{1-\nu^2} \frac{d^2w}{dx^2} dz = -\frac{Eh^3}{12(1-\nu^2)} \frac{d^2w}{dx^2} \quad 3.32$$

In Equation 3.32 we take the first term to be the flexural rigidity of the plate:

$$D = \frac{Eh^3}{12(1-\nu^2)} \quad 3.33$$

By using Hooke's law we can also find the external moments M_x and M_y for a three-dimensional problem. The normal stresses distributed over the lateral sides of the element (Figure 21) can be reduced to couples, the magnitudes of which, per unit length must be equal to the external moments:

$$\sigma_x = -\frac{Ez}{1-\nu^2} \left(\frac{\partial^2 w}{\partial x^2} + \nu \frac{\partial^2 w}{\partial y^2} \right) \quad 3.34$$

$$\sigma_y = -\frac{Ez}{1-\nu^2} \left(\frac{\partial^2 w}{\partial y^2} + \nu \frac{\partial^2 w}{\partial x^2} \right) \quad 3.35$$

$$\int_{-H/2}^{H/2} \sigma_x z dy dz = M_x dy \rightarrow M_x = -D \left(\frac{\partial^2 w}{\partial x^2} + \nu \frac{\partial^2 w}{\partial y^2} \right) \quad 3.36$$

$$\int_{-H/2}^{H/2} \sigma_y z dx dz = M_y dx \rightarrow M_y = -D \left(\frac{\partial^2 w}{\partial y^2} + \nu \frac{\partial^2 w}{\partial x^2} \right) \quad 3.37$$

If the directions x and y do not coincide with the principal planes of curvature, not only bending moments $M_x dy$ and $M_y dx$ will act on the sides of the element, but also the twisting moments $M_{xy} dy$ and $M_{yx} dx$. For the couple of twisting moments we obtain:

$$M_{xy} = D(1-\nu) \frac{\partial^2 w}{\partial x \partial y} \quad 3.38$$

3.2.2 Large deflections

When we consider large deflections also the tension in plane has to be considered. We again recall the kinematic Equations 3.24, 3.25 and 3.26 due to stretch:

$$\varepsilon_x = \frac{\partial u}{\partial x} + \frac{1}{2} \left(\frac{\partial w}{\partial x} \right)^2 \quad 3.24$$

$$\varepsilon_y = \frac{\partial v}{\partial y} + \frac{1}{2} \left(\frac{\partial w}{\partial y} \right)^2 \quad 3.25$$

$$\varepsilon_{xy} = \frac{\partial u}{\partial y} + \frac{\partial v}{\partial x} + \frac{\partial w}{\partial x} \frac{\partial w}{\partial y} \quad 3.26$$

If we again obey Hooke's law, we obtain:

$$\sigma_x = \frac{E}{1-\nu^2}(\varepsilon_x + \nu\varepsilon_y) = \frac{E}{1-\nu^2} \left(\left(\frac{\partial u}{\partial x} + \frac{1}{2} \left(\frac{\partial w}{\partial x} \right)^2 \right) + \nu \left(\frac{\partial v}{\partial y} + \frac{1}{2} \left(\frac{\partial w}{\partial y} \right)^2 \right) \right) \quad 3.39$$

$$\sigma_y = \frac{E}{1-\nu^2}(\varepsilon_y + \nu\varepsilon_x) = \frac{E}{1-\nu^2} \left(\left(\frac{\partial v}{\partial y} + \frac{1}{2} \left(\frac{\partial w}{\partial y} \right)^2 \right) + \nu \left(\frac{\partial u}{\partial x} + \frac{1}{2} \left(\frac{\partial w}{\partial x} \right)^2 \right) \right) \quad 3.40$$

$$\sigma_{xy} = \frac{E}{2(1+\nu)}\varepsilon_{xy} = \frac{E}{1-\nu^2} \frac{1-\nu}{2} \left(\frac{\partial u}{\partial y} + \frac{\partial v}{\partial x} + \frac{\partial w}{\partial x} \frac{\partial w}{\partial y} \right) \quad 3.41$$

Integration of Equations 3.39, 3.40 and 3.41 over the thickness of the plate results in the plates tension components:

$$N_x = \frac{Eh}{1-\nu^2}(\varepsilon_x + \nu\varepsilon_y) = \frac{Eh}{1-\nu^2} \left(\left(\frac{\partial u}{\partial x} + \frac{1}{2} \left(\frac{\partial w}{\partial x} \right)^2 \right) + \nu \left(\frac{\partial v}{\partial y} + \frac{1}{2} \left(\frac{\partial w}{\partial y} \right)^2 \right) \right) \quad 3.42$$

$$N_y = \frac{Eh}{1-\nu^2}(\varepsilon_y + \nu\varepsilon_x) = \frac{Eh}{1-\nu^2} \left(\left(\frac{\partial v}{\partial y} + \frac{1}{2} \left(\frac{\partial w}{\partial y} \right)^2 \right) + \nu \left(\frac{\partial u}{\partial x} + \frac{1}{2} \left(\frac{\partial w}{\partial x} \right)^2 \right) \right) \quad 3.43$$

$$N_{xy} = \frac{Eh}{2(1+\nu)}\varepsilon_{xy} = \frac{Eh}{1-\nu^2} \frac{1-\nu}{2} \left(\frac{\partial u}{\partial y} + \frac{\partial v}{\partial x} + \frac{\partial w}{\partial x} \frac{\partial w}{\partial y} \right) \quad 3.44$$

3.2.3 Derivation of the ABD-matrix

For the description of the membrane mechanics the constitutive equations derived in section 3.2 are placed in the ABD-matrix. The ABD-matrix defines the bending and extensional stiffness of the plate and is used in Section 3.3 for the derivation of the total strain energy of the membrane for the determination of the load-deflection relation.

The ABD-matrix shows the constitutive relations of the thin plate in a short overview:

$$\begin{Bmatrix} \underline{N} \\ \underline{M} \end{Bmatrix} = \begin{bmatrix} \underline{A} & \underline{B} \\ \underline{B} & \underline{D} \end{bmatrix} \begin{Bmatrix} \underline{\varepsilon} \\ \underline{\kappa} \end{Bmatrix} \quad 3.45$$

With:

$$\begin{Bmatrix} N_x \\ N_y \\ N_{xy} \end{Bmatrix} = \begin{bmatrix} A_{11} & A_{12} & A_{16} \\ A_{21} & A_{22} & A_{26} \\ A_{61} & A_{62} & A_{66} \end{bmatrix} \begin{Bmatrix} \varepsilon_x \\ \varepsilon_y \\ \varepsilon_{xy} \end{Bmatrix} + \begin{bmatrix} B_{11} & B_{12} & B_{16} \\ B_{21} & B_{22} & B_{26} \\ B_{61} & B_{62} & B_{66} \end{bmatrix} \begin{Bmatrix} \kappa_x \\ \kappa_y \\ \kappa_{xy} \end{Bmatrix} \quad 3.46$$

$$\begin{Bmatrix} M_x \\ M_y \\ M_{xy} \end{Bmatrix} = \begin{bmatrix} B_{11} & B_{12} & B_{16} \\ B_{21} & B_{22} & B_{26} \\ B_{61} & B_{62} & B_{66} \end{bmatrix} \begin{Bmatrix} \varepsilon_x \\ \varepsilon_y \\ \varepsilon_{xy} \end{Bmatrix} + \begin{bmatrix} D_{11} & D_{12} & D_{16} \\ D_{21} & D_{22} & D_{26} \\ D_{61} & D_{62} & D_{66} \end{bmatrix} \begin{Bmatrix} \kappa_x \\ \kappa_y \\ \kappa_{xy} \end{Bmatrix} \quad 3.47$$

In which:

$\underline{A}(A_{ij})$ =extensional (membrane) stiffness matrix and its elements ($i,j=1,2,6$)

$\underline{B}(B_{ij})$ =bending-extension-coupling stiffness matrix and its elements ($i,j=1,2,6$)

$\underline{D}(D_{ij})$ =bending (flexural) stiffness matrix and its elements ($i,j=1,2,6$)

When considering an isotropic, homogeneous material, the bending-extension-coupling stiffness matrix is zero. The bending stiffness matrix can be obtained from Equations 3.36, 3.37, 3.38 and 3.33:

$$\begin{Bmatrix} M_x \\ M_y \\ M_{xy} \end{Bmatrix} = D \begin{bmatrix} 1 & \nu & 0 \\ \nu & 1 & 0 \\ 0 & 0 & \frac{1-\nu}{2} \end{bmatrix} \begin{Bmatrix} \kappa_x \\ \kappa_y \\ \kappa_{xy} \end{Bmatrix} \quad 3.48$$

The extensional stiffness matrix can be obtained from Equations 3.42, 3.43 and 3.44:

$$\begin{Bmatrix} N_x \\ N_y \\ N_{xy} \end{Bmatrix} = \frac{Eh}{1-\nu^2} \begin{bmatrix} 1 & \nu & 0 \\ \nu & 1 & 0 \\ 0 & 0 & \frac{1-\nu}{2} \end{bmatrix} \begin{Bmatrix} \varepsilon_x \\ \varepsilon_y \\ \varepsilon_{xy} \end{Bmatrix} \quad 3.49$$

From Equations 3.48 and 3.49 we obtain the following ABD-matrix:

$$\begin{bmatrix} \frac{Eh}{1-\nu^2} & \nu \frac{Eh}{1-\nu^2} & 0 & 0 & 0 & 0 \\ \nu \frac{Eh}{1-\nu^2} & \frac{Eh}{1-\nu^2} & 0 & 0 & 0 & 0 \\ 0 & 0 & \frac{Eh}{2(1+\nu)} & 0 & 0 & 0 \\ 0 & 0 & 0 & \frac{Eh^3}{12(1-\nu^2)} & \nu \frac{Eh^3}{12(1-\nu^2)} & 0 \\ 0 & 0 & 0 & \nu \frac{Eh^3}{12(1-\nu^2)} & \frac{Eh^3}{12(1-\nu^2)} & 0 \\ 0 & 0 & 0 & 0 & 0 & \frac{Eh^3}{24(1+\nu)} \end{bmatrix} \quad 3.50$$

3.3 Equilibrium Equations

Equilibrium here is determined by the principle of minimum potential energy. Considering the second law of thermodynamics, a system will always approach a point (stationary value) that minimizes its energy.

3.3.1 Potential energy

We consider a body, initially in equilibrium, subjected to a combination of surface forces F_s and body forces F_b , and quasi-statically deforms and displaces as a result of these forces. For the derivation of the equilibrium equations, we use the method of minimum potential energy. The total potential energy of the system contains the bending strain energy, the extensional strain energy, the potential energy of body forces and the potential energy of surface forces. The external forces result in potential energy of opposite sign, as the potential of these forces decrease when the internal potential increases. The total potential energy of the system can therefore be defined as follows:

$$U = W_{plate} + W_{load} \quad 3.51$$

$$U = \int_{volume} W dV - \int_{surface} (F_{s,x} u + F_{s,y} v + F_{s,z} w) dS - \int_{volume} (F_{b,x} u + F_{b,y} v + F_{b,z} w) dV \quad 3.52$$

In which W is the strain energy of the plate, containing the bending strain energy and the extensional strain energy. $F_{s,xyz}$ are the surface force components, and $F_{b,xyz}$ the body force components.

A material under strain contains elastic energy; energy stored in a body or in a system due to its position in a force field or due to its configuration. Since energy is the sum over all displacements time the force needed for the displacement, we derive for the elastic strain energy (W) for a thin plate per unit volume; one-half the product of stress times strain for each component. The factor $1/2$ results from counting twice for each component. For an element of volume dV we obtain:

$$dW_{plate} = \frac{1}{2} \sum_{i=x,y,z} \sum_{j=x,y,z} \sigma_{ij} \epsilon_{ij} dV \quad 3.53$$

For the total strain energy of the plate we now obtain:

$$W_{plate} = \frac{1}{2} \iiint \left(\sum_{i=x,y,z} \sum_{j=x,y,z} \sigma_{ij} \epsilon_{ij} \right) dx dy dz \quad 3.54$$

We can express stress in terms of the product of stiffness and strain. The strain energy of the plate can therefore be derived from the ABD-matrix 3.50 (containing the bending and extensional stiffness of the plate).

$$W_{plate} = \int_A \frac{1}{2} \left[\underline{\epsilon}^T : \underline{K}^T \right] \begin{bmatrix} \underline{A} & \underline{B} \\ \underline{B} & \underline{C} \end{bmatrix} \begin{bmatrix} \underline{\epsilon} \\ \underline{\kappa} \end{bmatrix} dA \quad 3.55$$

Equation 3.55 shows the integration over the area of the plate, as in the stiffness matrix the height of the plate is already included. Previously stated, for an isotropic, homogeneous material, the bending-extension coupling stiffness matrix \underline{B} equals zero. Therefore, with Equations 3.48 and 3.49 we obtain:

$$W_{plate} = \frac{1}{2} \int_A \left\{ \underline{N}^T \underline{\epsilon} + \underline{M}^T \underline{\kappa} \right\} dA \quad 3.56$$

The first term in Equation 3.56 represents the strain energy due to the extension, and the second term due to bending of the plate. We thus obtain for the strain energy due to bending (and twisting) of the plate (from Eq. 3.48):

$$W_{\text{bending \& twisting}} = \frac{1}{2} \iint (M_x \kappa_x + M_y \kappa_y + M_{xy} \kappa_{xy}) dx dy \quad 3.57$$

$$W_{\text{bending \& twisting}} = \frac{1}{2} D \iint \left[\kappa_x^2 + \kappa_y^2 + 2\nu \kappa_x \kappa_y + \left(\frac{1-\nu}{2} \right) \kappa_{xy}^2 \right] dx dy \quad 3.58$$

With kinematic Equations 3.18, 3.19 and 3.20, we obtain:

$$W_{\text{bending \& twisting}} = \frac{D}{2} \iint \left\{ \left(\frac{\partial^2 w}{\partial x^2} \right)^2 + \left(\frac{\partial^2 w}{\partial y^2} \right)^2 + 2\nu \left(\frac{\partial^2 w}{\partial x^2} \frac{\partial^2 w}{\partial y^2} \right) + 2(1-\nu) \left(\frac{\partial^2 w}{\partial x \partial y} \right)^2 \right\} dx dy \quad 3.59$$

Equation 3.59 can be rewritten as follows (Appendix 2):

$$W_{\text{bending \& twisting}} = \frac{D}{2} \iint \left\{ \left(\frac{\partial^2 w}{\partial x^2} + \frac{\partial^2 w}{\partial y^2} \right)^2 - 2(1-\nu) \left[\frac{\partial^2 w}{\partial x^2} \frac{\partial^2 w}{\partial y^2} - \left(\frac{\partial^2 w}{\partial x \partial y} \right)^2 \right] \right\} dx dy \quad 3.60$$

For the strain energy due to the extension of the plate, the first term in Equation 3.56, we derive (from Eq. 3.49):

$$W_{\text{extension}} = \frac{1}{2} \iint (N_x \varepsilon_x + N_y \varepsilon_y + N_{xy} \varepsilon_{xy}) dx dy \quad 3.61$$

$$W_{\text{extension}} = \frac{Eh}{2(1-\nu^2)} \iint \left[\varepsilon_x^2 + \varepsilon_y^2 + 2\nu \varepsilon_x \varepsilon_y + \left(\frac{1-\nu}{2} \right) \varepsilon_{xy}^2 \right] dx dy \quad 3.62$$

With kinematic Equations 3.24, 3.25 and 3.26 we obtain for the extensional strain energy:

$$W_{\text{extension}} = \frac{Eh}{2(1-\nu^2)} \iint \left\{ \left(\frac{\partial u}{\partial x} \right)^2 + \frac{\partial u}{\partial x} \left(\frac{\partial w}{\partial x} \right)^2 + \left(\frac{\partial v}{\partial y} \right)^2 + \frac{\partial v}{\partial y} \left(\frac{\partial w}{\partial y} \right)^2 + \frac{1}{4} \left[\left(\frac{\partial w}{\partial x} \right)^2 + \left(\frac{\partial w}{\partial y} \right)^2 \right]^2 + 2\nu \left[\frac{\partial u}{\partial x} \frac{\partial v}{\partial y} + \frac{1}{2} \frac{\partial v}{\partial y} \left(\frac{\partial w}{\partial x} \right)^2 + \frac{1}{2} \frac{\partial u}{\partial x} \left(\frac{\partial w}{\partial y} \right)^2 \right] + \frac{1-\nu}{2} \left[\left(\frac{\partial u}{\partial y} \right)^2 + 2 \frac{\partial u}{\partial y} \frac{\partial v}{\partial x} + \left(\frac{\partial v}{\partial x} \right)^2 + 2 \frac{\partial u}{\partial y} \frac{\partial w}{\partial x} \frac{\partial w}{\partial y} + 2 \frac{\partial v}{\partial x} \frac{\partial w}{\partial x} \frac{\partial w}{\partial y} \right] \right\} dx dy \quad 3.63$$

For the total strain energy (Eq. 3.56) of the plate we derive:

$$W_{\text{plate}} = W_{\text{extension}} + W_{\text{bending+twisting}} \quad 3.64$$

$$W_{\text{plate}} = \frac{1}{2} \iint \left\{ \frac{Eh}{(1-\nu^2)} \left[\varepsilon_x^2 + \varepsilon_y^2 + 2\nu \varepsilon_x \varepsilon_y + \left(\frac{1-\nu}{2} \right) \varepsilon_{xy}^2 \right] + D \left[\kappa_x^2 + \kappa_y^2 + 2\nu \kappa_x \kappa_y + \left(\frac{1-\nu}{2} \right) \kappa_{xy}^2 \right] \right\} dx dy \quad 3.65$$

When considering a distributed load (P) underneath the thin plate we define (from Eq. 3.52) the load potential as follows:

$$W_{load} = - \iint \{Pw\} dx dy \quad 3.66$$

The total strain energy and the load potential together form the total potential energy of the system (U). The body forces can be neglected when considering very thin plates, the body forces (from gravitational forces) are not significant for membranes with negligible mass.

3.3.2 Equilibrium

A structure or body will deform or displace to a position that minimizes the potential energy (second law of thermodynamics), the structure will approach a stationary point. Therefore by using approximations for the displacement fields, calculating the total potential energy, and varying the approximate solutions to find a minimum in the total potential energy, we can find the load-deflection behavior of the structure.

For this calculation we first define trial displacement functions:

$$\begin{aligned} \hat{u}(x, y, z : c_1, c_2, \dots, c_n) \\ \hat{v}(x, y, z : c_1, c_2, \dots, c_n) \\ \hat{w}(x, y, z : c_1, c_2, \dots, c_n) \end{aligned} \quad 3.67$$

Where c_1, c_2, \dots, c_n are a set of n parameters that appear in the trial functions. With the definition of U (Eq. 3.51), we find the total potential energy of the system, which will depend on the parameters c_1, c_2, \dots, c_n . To find a stationary point in the total potential energy (minimum), we can require:

$$\frac{\partial U}{\partial c_1} = 0 \dots \frac{\partial U}{\partial c_j} = 0 \dots \frac{\partial U}{\partial c_n} = 0 \quad 3.68$$

Solving the n equations (Eq. 3.68), gives n values of c_i that minimize the total potential energy, and with that represent the best approximation to the initial equilibrium displacements [52, 53].

4 Membrane Load-Deflection

This chapter describes the load-deflection behaviour of both the dogbone and circular configuration according to a derived Analytical Model with use of the method of Minimum Potential Energy of the system.

Verification of the Analytical Model is realised by use of a Finite Element Model and experimental results (Section 4.5).

With use of the mathematical Left Ventricle model described in Chapter 2, these relations lead to a relation between a desired cardiomyocyte cell-strain and the applied membrane pressure.

4.1 Membrane Displacement Field

For the calculation of the total potential energy of the system, approximations for the displacement fields are defined. By varying the approximate solutions the load-deflection behavior of the structure can be determined. In this section the trial displacement functions (Eq. 3.67) are defined. In Section 4.2 the trial displacement functions are incorporated in the potential energy of the system, from which the membrane deflection and strain can be derived (Section 4.3, Section 4.4).

4.1.1 Dogbone configuration

The Cytostretch chip exists in two configurations, a circular configuration for multi-axial loading, and a dogbone configuration for uni-axial loading conditions. The uni-axial loading configuration (Figure 22) is developed for the determination of the influence of directed mechanical load; recently only one direction is incorporated in the dogbone configuration. Only transverse strain is tested, as the grooves lie in longitudinal direction (Figure 22).

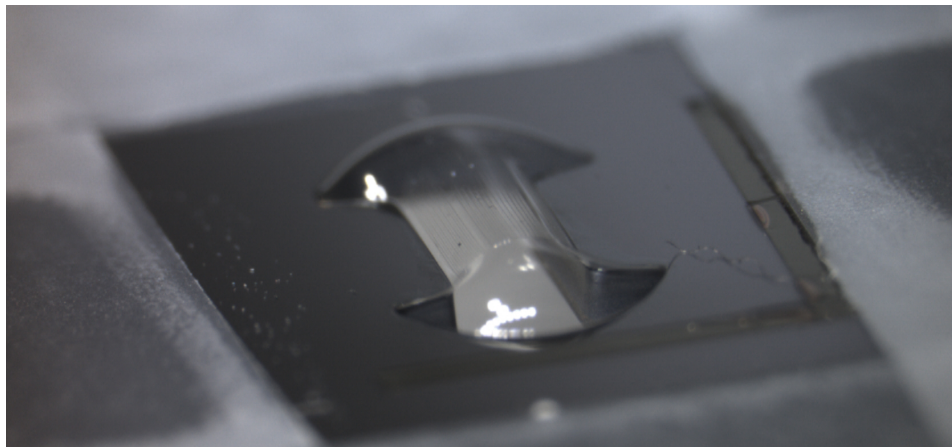


Figure 22: Image of an inflated dogbone chip excluding culture container, interconnects and electrodes. Cells are transversely strained on this membrane due to the long-axis oriented grooves. Notice that the centre-section of the membrane bulges up cylindrically, realising the uni-axial straining condition. The strain in the membrane can thus be calculated from a small section of the centre region. We are able to model the centre section of the dogbone simply by a double clamped thin beam (a two dimensional representation).

The geometry of the dogbone configuration results in zero strain in the longitudinal direction over the middle part as the strain in this direction gets absorbed by the two half circular parts at both ends. The cells are thus in a uni-axial manner strained in the middle section of the membrane.

For the derivation of the Analytical Model of this dogbone membrane, we are thus able to simplify the membrane to a square membrane clamped at the two edges parallel to the grooves and symmetry conditions on the edges perpendicular to the grooves. The upper side of the membrane has a free boundary condition, and on the bottom side exists a distributed pressure-load. As a result from the symmetry axes on both edges perpendicular to the x -axis, we can describe the total behavior of the middle part of the membrane by the description of a small slice (dy) of the membrane. The load-deflection behaviour of the middle part of the dogbone membrane can thus be described by a two-dimensional Analytical Model of a uniformly loaded double-clamped beam (Figure 23).

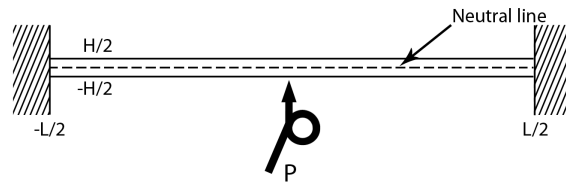


Figure 23: Two-dimensional representation of the dogbone membrane. The centre section of the membrane can be modelled by a double clamped thin beam with a length L and a thickness H .

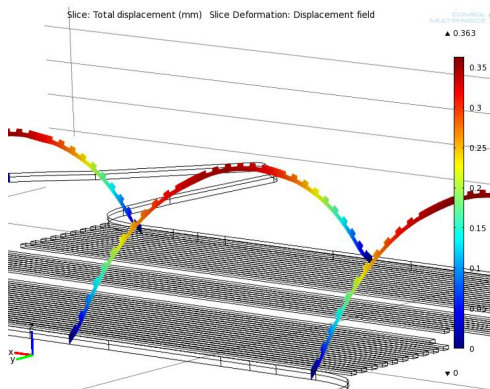


Figure 24: Membrane slices depicting the membrane displacement of the centre section of the dogbone membrane. Notice the correspondence in deflection with the 2D representation of Figure 25.

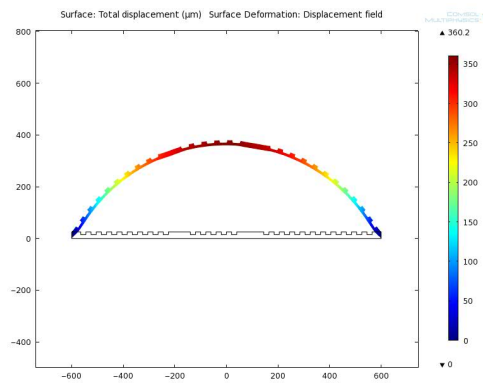


Figure 25: 2D representation depicting the membrane displacement of the centre section of the dogbone membrane. Notice the correspondence in deflection with the 3D representation of Figure 24.

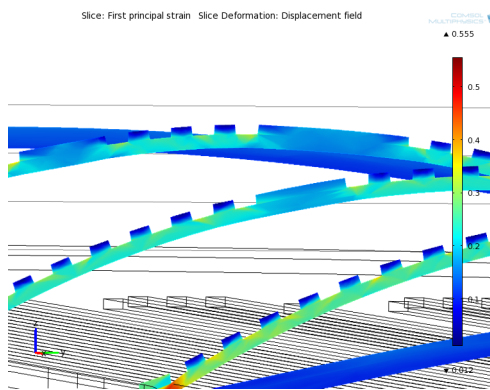


Figure 26: Membrane slices depicting the membranes axial strain in the centre section of the dogbone membrane. Notice the correspondence in strain with the 2D representation of Figure 27.

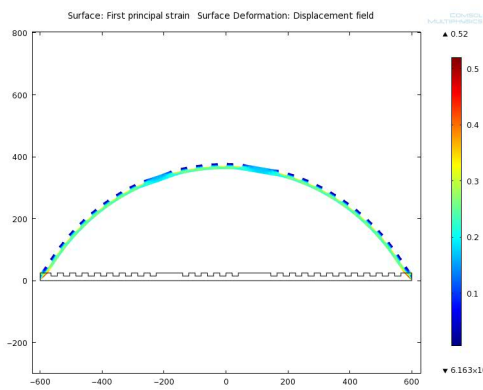


Figure 27: 2D representation depicting the membranes axial strain in the centre section of the dogbone membrane. Notice the correspondence in strain values with the 3D representation of Figure 26.

The 2D simplification assumption has been verified with use of 2D and 3D Finite Element simulations (Appendix 1)(Figure 24 - Figure 27). Notice the correspondence in deflection in the 2D simulation in Figure 26 and the 3D simulation in Figure 25. This correspondence can also be seen in the transverse strain in the various simulations (Figure 26 and Figure 27).

The two edges of the small slice of the dogbone membrane is clamped, leading to a displacement field representing two directions, a displacement function u in x-direction, and a displacement function in the z-direction, w (the deflection of the membrane). A trial displacement function has to be kinematically admissible, which means that it has to be continuous and has to satisfy the boundary conditions. The trial displacement function thus has to satisfy the clamped edges and symmetry conditions:

$$\frac{\partial \hat{w}}{\partial x} = 0 \xrightarrow{\text{for}} x = \pm \frac{L}{2} \quad 4.1$$

$$\frac{\partial \hat{w}}{\partial x} = 0 \xrightarrow{\text{for}} x = 0 \quad 4.2$$

$$\hat{u} = 0 \xrightarrow{\text{for}} x = \pm \frac{L}{2} \quad 4.3$$

$$\hat{w} = 0 \xrightarrow{\text{for}} x = \pm \frac{L}{2} \quad 4.4$$

We assume the following trial membrane displacement function in z-direction:

$$\hat{w} = \frac{w_0}{2} \left(1 + \cos \frac{2\pi x}{L} \right) \quad [52] \quad 4.5$$

The cosine describes the membrane movement with clamped edges satisfying condition 4.1 and symmetry condition 4.2, the constant w_0 describes the centre-deflection of the membrane.

Figure 28 shows the displacement function in z-direction (after determination of the constant w_0), for visualization. Notice that the cosine in the trial function properly describes the clamped edges, satisfies the boundary conditions.

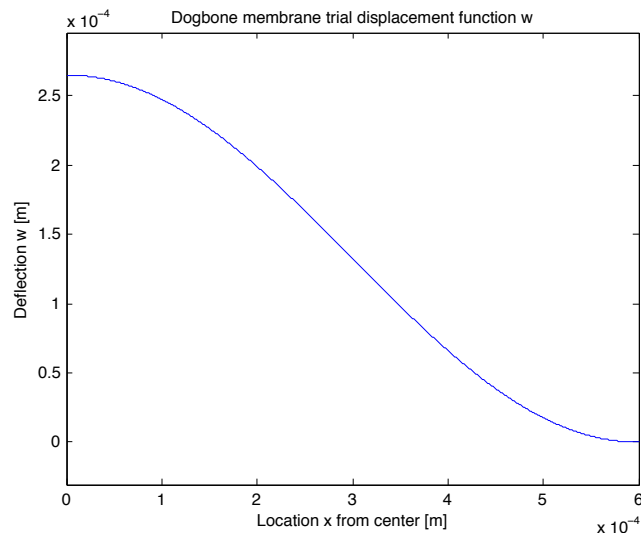


Figure 28: Dogbone membrane trial displacement function in z-direction (depicting the deflection), versus the location x from the centre. The origin is denoted as the centre of the membrane at the reference state. Notice that the function properly describes the clamped edges, as the deflection leaves under a zero tangent at the edges.

The displacement in x -direction; u , can be described by Equation 4.6. The displacement function satisfies the boundary conditions as the first term ensures symmetry, zero displacement at the centre. The second term ensures the edge condition, zero displacement at the edges. The polynomial part of the function contains several terms, each refining the function. The refinements reduce the error of the function.

$$\hat{u} = x \left(\frac{L}{2} - x \right) (c_1 + c_2 x + c_3 x^2 + c_4 x^3 + c_5 x^4 + \dots) \quad [52] \quad 4.6$$

Initially we use the first two terms of the trial displacement function 4.7:

$$\hat{u} = x \left(\frac{L}{2} - x \right) (c_1 + c_2 x) \quad [52] \quad 4.7$$

Notice that function 4.8 again satisfies the boundary conditions of the clamped membrane (4.3). Figure 29 shows the trial displacement function (after determination of the constants) for visualization. The negative displacement in x -direction relates to the clamped edges. The displacement appears to be outward in the central section, and inward in the outside sections. At $x=300\mu\text{m}$ from the centre the membrane only moves upward.

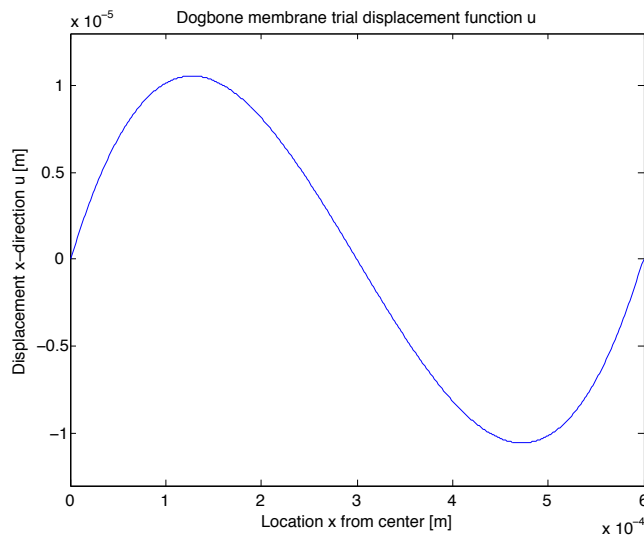


Figure 29: Dogbone membrane trial displacement function u , representing the in plane displacement of the membrane (x -direction). Location 0 again denotes the centre of the membrane. Notice the negative displacement towards the edges. Due to the clamped edges the x -displacement appears to be towards the edges in the centre section of the membrane, however in the outer section of the membrane the x -displacement appears to be towards the centre (negative).

4.1.2 Circular configuration

The circular membrane; designed for multi-axial loading, with grooves running in radial direction; has to be modelled in a three-dimensional manner. The entire edge of the circular membrane is clamped. For simplification we use polar coordinates, this way we can represent the displacement field again in two directions; a radial displacement function u (Figure 30), and a displacement function in the w , in z -direction (Figure 31).

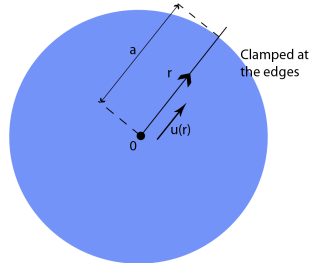


Figure 30: Representation of the circular membrane, depicting the direction of the in plane displacement u , in radial direction.

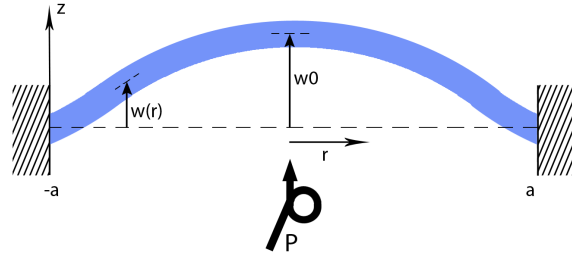


Figure 31: Cross-sectional representation of the circular membrane, depicting the direction of the out of plane displacement w , in z -direction.

We consider the same boundary conditions as for the dogbone membrane (conditions 4.1, 4.2 and 4.3), only applied to the circular membrane (polar coordinate system):

$$\frac{\partial \hat{w}}{\partial r} = 0 \text{ ---for---} \rightarrow r = a \quad 4.8$$

$$\frac{\partial \hat{w}}{\partial r} = 0 \text{ ---for---} \rightarrow r = 0 \quad 4.9$$

$$\hat{u} = 0 \text{ ---for---} \rightarrow r = a \quad 4.10$$

$$\hat{w} = 0 \text{ ---for---} \rightarrow r = a \quad 4.11$$

The trial displacement field has to satisfy the conditions 4.9, 4.10 and 4.11 above. In the conditions a is considered the radius of the membrane. We define the trial membrane displacement function in z -direction as:

$$\hat{w} = w_0 \left(1 - \frac{r^2}{a^2} \right)^2 \quad 4.12$$

[52]

For the displacement function in z -direction we now consider a cubic function instead of the cosine function to describe the clamped edges. This enables us to determine if the trial function has a big influence on the outcome. Figure 32 shows the trial displacement function u (after determination of the constants), and Figure 33, the trial displacement function w , for visualization. Notice that the cubic function also describes the clamped edges properly, and satisfies the boundary conditions.

For the trial membrane displacement function u in r -direction we take:

$$\frac{\hat{u}}{r} = (a - r) (c_1 + c_2 r + c_3 r^2 + c_4 r^3 + c_5 r^4 + \dots) \quad 4.13$$

In Function 4.13 r ranges from zero (centre of the membrane) to a (membrane edge). Function 4.13 is defined as such, because we do not want to constrict the central membrane r -displacement to zero, this means that we do want u to go to zero when r goes to zero, however the limit of u divided by r does not equal zero. In order to satisfy this condition, we first define the displacement function u , as u divided by r . For an easy

implementation into the potential energy functions described in Chapter 3, we now multiply both sides with r :

$$\hat{u} = r(a - r)(c_1 + c_2 r + c_3 r^2 + c_4 r^3 + c_5 r^4 + \dots) \quad 4.14$$

The displacement field in r -direction (u) now becomes identical to the displacement function u of the dogbone membrane, satisfying the boundary conditions. We again initially consider the first two terms of the polynomial part of the function.

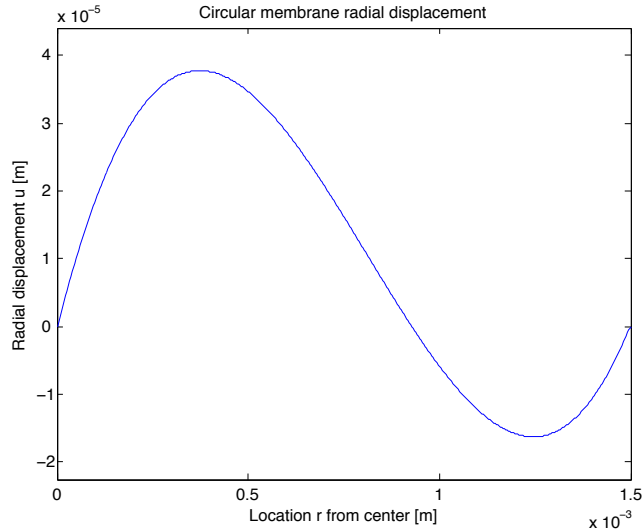


Figure 32: Circular membrane trial displacement function u , representing the in plane displacement of the membrane (r -direction). Location 0 denotes the centre of the membrane. Notice the similarity with the dogbone u -displacement function. We obtain a negative displacement towards the edges. Due to the clamped edges the r -displacement again appears to be towards the edges in the centre section of the membrane, however in the outer section of the membrane the r -displacement appears to be towards the centre (negative).

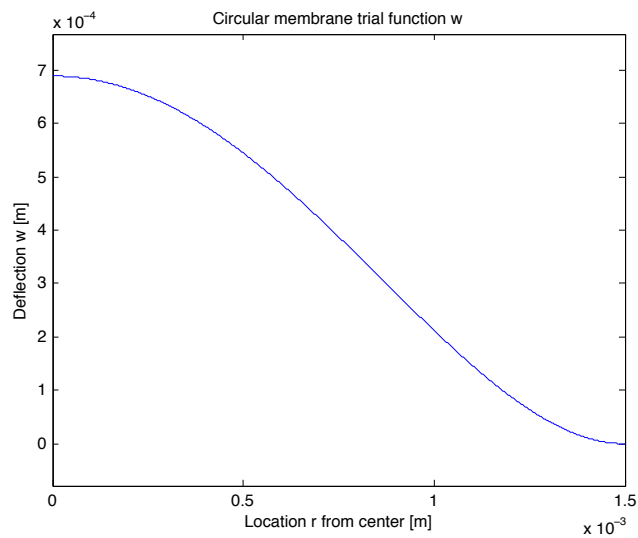


Figure 33: Circular membrane trial displacement function in z -direction (depicting the deflection), versus the location r (polar coordinates) from the centre. The origin again is denoted as the centre of the membrane at the reference state. Notice that similar to the case of the dogbone membrane, the trial function properly describes the clamped edges, as the deflection leaves under a zero tangent at the edges.

The displacement of membrane elements in radial direction is taken positive from the centre of the membrane, outwards (positive r -direction). The centre element moves straight up, with no displacement in the radial directions, membrane elements further outward move towards the edge of the membrane. However, membrane elements near the edge of the membrane move inwards, similar to the dogbone's x -displacement. This membrane movement can be seen in Figure 32, notice that there is a ring on the membrane where the outward and inward moving elements will meet, this part of the membrane moves straight up. The displacement in r -direction shows similarity with the x -displacement of the dogbone membrane.

The displacement function in z -direction (displacement function w , Figure 33) resembles the displacement function of the dogbone membrane, however this displacement has been represented in polar coordinates and thus holds for a three-dimensional circular case. The displacement function shows the deflection of the membrane in a sphere like manner (in contrary to the cylindrical manner of the dogbone membrane), and shows the clamped edge by tangent approaching zero at the edge.

4.2 Membrane Potential Energy

The potential energy of the system leads to the derivation of the true displacement field, by deriving the constants in the trial displacement functions u and w . Mentioned previously; The kinematics of thin plates can be applied to large membranes when considering stretch of the neutral line, due to in-plane displacement additional to pure bending strains, due to perpendicular displacement. This is due to the fact that we allow for the deflections to be large, and include two sources of strain energy, both energy in the bending of the membrane (only strain term when considering small deflections), and the energy due to the stretching of the membrane. The potential energy equations for a thin plate derived from kinematic equations and constitutive equations considers the bending strain energy and extensional strain energy, Equation 3.64. Therefore, we are able to directly apply them to both membrane configurations.

4.2.1 Dogbone Configuration

We recall the strain energy equation for bending and twisting of the membrane, Equation 3.58:

$$W_{\text{bending \& twisting}} = \frac{1}{2} D \iint \left[\kappa_x^2 + \kappa_y^2 + 2\nu\kappa_x\kappa_y + \left(\frac{1-\nu}{2}\right)\kappa_{xy}^2 \right] dx dy \quad 3.58$$

For the dogbone configuration we obtain a simplified version of the bending strain energy. We consider a small element (2D representation) of the membrane, thus only consider the curvature in one direction, the x -direction:

$$W_{\text{bending \& twisting}} = \frac{D}{2} \int_0^1 \int_{-L/2}^{L/2} \left\{ \kappa_x^2 \right\} dx dy \quad 4.15$$

The width of the membrane element dy we take equal to unity. With the kinematic Equation 3.15 we now obtain for the strain energy due to bending and twisting of the dogbone membrane:

$$W_{\text{bending \& twisting}} = \frac{D}{2} \int_0^1 \int_{-L/2}^{L/2} \left\{ \left(\frac{\partial^2 w}{\partial x^2} \right)^2 \right\} dx dy \quad 4.16$$

Introduction of the trial displacement function for the dogbone configuration, 4.5, leads to the following bending strain energy:

$$W_{\text{bending \& twisting}} = D \frac{\pi^4 w_0^2}{L^3} \quad 4.17$$

For the strain energy due to the extension of the membrane, we recall Equation 3.62, and obtain by using the kinematic Equation 3.24:

$$W_{\text{extension}} = \frac{Eh}{2(1-\nu^2)} \iint \left[\varepsilon_x^2 + \varepsilon_y^2 + 2\nu\varepsilon_x\varepsilon_y + \left(\frac{1-\nu}{2}\right)\varepsilon_{xy}^2 \right] dx dy \quad 3.62$$

$$W_{\text{extension}} = \frac{Eh}{2(1-\nu^2)} \int_0^1 \int_{-L/2}^{L/2} \{ \varepsilon_x^2 \} dx dy \quad 4.18$$

$$W_{\text{extension}} = \frac{Eh}{2(1-\nu^2)} \int_0^1 \int_{-L/2}^{L/2} \left\{ \left[\frac{\partial u}{\partial x} + \frac{1}{2} \left(\frac{\partial w}{\partial x} \right)^2 \right]^2 \right\} dx dy \quad 4.19$$

We now obtain with use of the trial displacement field (Eq. 4.5 and 4.8) the following strain energy due to extension of the membrane:

$$W_{\text{extension}} = \frac{Eh}{L^3(1-\nu^2)} \left\{ \frac{L^8 c_2^2}{240} + \frac{L^7 c_1 c_2}{48} + \frac{L^6 c_1^2}{24} + \frac{3L^4 c_2 w_0^2}{32} + \frac{3\pi^4 w_0^4}{64} \right\} \quad 4.20$$

Equations 3.60, 3.63 and 3.66 show that solely the extensional strain energy depends on the displacement function u . We are thus able to derive the constants c_1 and c_2 from the expression for the extensional strain energy, by approaching a stationary point in the extensional strain energy:

$$\frac{\partial W_{\text{extension}}}{\partial c_1} = 0 \dots \frac{\partial W_{\text{extension}}}{\partial c_j} = 0 \dots \frac{\partial W_{\text{extension}}}{\partial c_n} = 0 \quad 4.21$$

Leading to the following expressions for the constants c_1 , c_2 and $W_{\text{extension}}$:

$$c_1 = \frac{15w_0^2}{L^3} \quad 4.22$$

$$c_2 = -\frac{30w_0^2}{L^4} \quad 4.23$$

$$W_{\text{extension}} = \frac{Eh}{(1-\nu^2)} \left\{ \frac{3w_0^4(\pi^4 - 30)}{64L^3} \right\} \quad 4.24$$

The total potential energy of the plate contains the strain energy of the membrane and the potential energy due to the load (Eq. 3.51). For the potential energy of the load we recall Equation 3.66, and obtain with use of the trial displacement function 4.5 the following expression for the load potential of the membrane:

$$W_{\text{load}} = -\iint \{ Pw \} dx dy \quad 3.66$$

$$W_{\text{load}} = -\int_0^1 \int_{-L/2}^{L/2} \{ Pw \} dx dy \quad 4.25$$

$$W_{load} = -\frac{LPw_0}{2} \quad 4.26$$

The total potential energy of the system follows from Equation 3.33 3.51, 4.16, 4.23 and 4.25:

$$U = \frac{Eh^3}{12(1-\nu^2)} \frac{\pi^4 w_0^2}{L^3} + \frac{Eh}{(1-\nu^2)} \left\{ \frac{3w_0^4(\pi^4 - 30)}{64L^3} \right\} - \frac{LPw_0}{2} \quad 4.27$$

The constant w_0 can now be determined by minimizing the total potential energy of the system, finding a stationary point:

$$\frac{\partial U}{\partial w_0} = 0 \quad 4.28$$

This leads to the following load-centre-deflection relation:

$$P = \frac{Eh^3}{12(1-\nu^2)} \frac{4\pi^4 w_0}{L^4} + \frac{Eh}{(1-\nu^2)} \left\{ \frac{3w_0^3(\pi^4 - 30)}{8L^3} \right\} \quad 4.29$$

A cubic function in which w_0 is the centre-deflection of the membrane, which can be calculated for various pressures. From this load-deflection behavior we are able to determine the axial strain in the membrane.

4.2.2 Circular configuration

The determination of the potential energy of the circular membrane can be done in a similar manner. Due to the circular configuration, we are able to express the potential energy in polar coordinates. This enables us to simplify the equations to two directions, the radial direction r and the transverse direction θ . The transformation to the polar coordinate system results in different kinematic and constitutive equations. In analogy with the matrices 3.48 and 3.49 (isotropic, homogeneous material), we obtain the following constitutive matrices for the circular membrane:

$$\begin{Bmatrix} N_r \\ N_t \\ N_n \end{Bmatrix} = \frac{Eh}{1-\nu^2} \begin{bmatrix} 1 & \nu & 0 \\ \nu & 1 & 0 \\ 0 & 0 & \frac{1-\nu}{2} \end{bmatrix} \begin{Bmatrix} \varepsilon_r \\ \varepsilon_t \\ \varepsilon_n \end{Bmatrix} \quad 4.30$$

$$\begin{Bmatrix} M_r \\ M_t \\ M_n \end{Bmatrix} = D \begin{bmatrix} 1 & \nu & 0 \\ \nu & 1 & 0 \\ 0 & 0 & \frac{1-\nu}{2} \end{bmatrix} \begin{Bmatrix} \kappa_r \\ \kappa_t \\ \kappa_n \end{Bmatrix} \quad 4.31$$

Because of the circular symmetry we do not have to take into account any shear strains in the membrane, the shear strains are equal to zero. Conversion of the kinematic expressions for the curvature to a polar coordinate system results in:

$$\kappa_r = -\frac{\partial^2 w}{\partial r^2} \quad 4.32$$

$$\kappa_t = -\frac{1}{r} \frac{\partial w}{\partial r} \quad 4.33$$

Where t represents the curvature in transverse direction. With use of Equation 3.24, we obtain for the strain in radial direction (large deflections):

$$\varepsilon_r = \frac{\partial u}{\partial r} + \frac{1}{2} \left(\frac{\partial w}{\partial r} \right)^2 \quad 4.34$$

And the strain in transverse direction obviously becomes:

$$\varepsilon_t = \frac{\Delta L}{L_0} = \frac{2\pi(r+u) - 2\pi r}{2\pi r} = \frac{u}{r} \quad 4.35$$

The strain energy due to bending and twisting now becomes:

$$W_{\text{bending \& twisting}} = \frac{1}{2} \iint (M_r \kappa_r + M_t \kappa_t + M_{rt} \kappa_{rt}) r dr d\theta = \frac{1}{2} \iint (M_r \kappa_r + M_t \kappa_t) r dr d\theta \quad 4.36$$

$$W_{\text{bending}} = \pi D \int [\kappa_r^2 + \kappa_t^2 + 2\nu \kappa_r \kappa_t] r dr \quad 4.37$$

For the bending strain energy we now obtain from kinematic expressions 4.31 and 4.32:

$$W_{\text{bending}} = \iint \left\{ \frac{D}{2} \left[\left(\frac{\partial^2 w}{\partial r^2} \right)^2 + \left(\frac{1}{r} \frac{\partial w}{\partial r} \right)^2 + \frac{2\nu}{r} \frac{\partial w}{\partial r} \frac{\partial^2 w}{\partial r^2} \right] \right\} r dr d\theta \quad 4.38$$

$$W_{\text{bending}} = \int_0^{2\pi} \int_0^a \left\{ \frac{D}{2} \left[\left(\frac{\partial^2 w}{\partial r^2} \right)^2 + \left(\frac{1}{r} \frac{\partial w}{\partial r} \right)^2 + \frac{2\nu}{r} \frac{\partial w}{\partial r} \frac{\partial^2 w}{\partial r^2} \right] \right\} r dr d\theta = \frac{32\pi}{3} \frac{w_0^2}{a^2} D \quad 4.39$$

Similar to Equation 4.36, we obtain for the strain energy due to the extension of the membrane:

$$W_{\text{extension}} = \frac{1}{2} \iint (N_r \varepsilon_r + N_t \varepsilon_t) r dr d\theta = \frac{\pi E h}{1-\nu^2} \int [\varepsilon_r^2 + \varepsilon_t^2 + 2\nu \varepsilon_r \varepsilon_t] r dr \quad 4.40$$

Substitution of the kinematic expressions 4.33 and 4.34 in 4.39 leads to the following expression for the extensional strain energy:

$$W_{\text{extension}} = \int_0^{2\pi} \int_0^a \left\{ \frac{Eh}{2(1-\nu^2)} \left[\left(\frac{\partial u}{\partial r} + \frac{1}{2} \left(\frac{\partial w}{\partial r} \right)^2 \right)^2 + \left(\frac{u}{r} \right)^2 + \frac{2\nu}{r} \left(\frac{\partial u}{\partial r} + \frac{1}{2} \left(\frac{\partial w}{\partial r} \right)^2 \right) \right] \right\} r dr d\theta \quad 4.41$$

We now obtain with use of the trial displacement field (Eq. 4.12 and 4.14) the following strain energy due to extension of the membrane:

$$W_{\text{extension}} = \frac{\pi E h}{1-\nu^2} \left\{ \frac{4a^2 c_2 w_0^2}{315} + \frac{44a^2 c_2 \nu w_0^2}{315} - \frac{46ac_1 w_0^2}{315} + \frac{82ac_1 \nu w_0^2}{315} + \frac{a^4 c_1^2}{4} + \frac{7a^6 c_2^2}{60} + \frac{32w_0^4}{105a^2} + \frac{3a^5 c_1 c_2}{10} \right\} \quad 4.42$$

We again derive the constants c_1 and c_2 from the expression for the extensional strain energy, by approaching a stationary point in the extensional strain energy.

$$c_1 = -\frac{w_0^2(444991\nu - 895018)}{630000a^3} \quad 4.43$$

$$c_2 = \frac{w_0^2(619\nu - 3762)}{2000a^4} \quad 4.44$$

$$W_{\text{extension}} = \frac{\pi Eh}{1-\nu^2} \left\{ \frac{425\nu w_0^4}{3969a^2} - \frac{222\nu^2 w_0^4}{3157a^2} + \frac{1501w_0^4}{7938a^2} \right\} \quad 4.45$$

For the potential energy of the load we recall Equation 3.66, and obtain with use of the trial displacement function 4.13 the following expression for the load potential of the membrane:

$$W_{\text{load}} = -\iint \{Pw\} drd\theta \quad 4.46$$

$$W_{\text{load}} = -2\pi P \int_0^a wrdr = -\frac{1}{3}\pi Pa^2 w_0 \quad 4.47$$

The potential energy of the system can now be defined as (D eliminated with use of Eq. 3.33):

$$U = \frac{32\pi}{3} \frac{w_0^2}{a^2} \frac{Eh^3}{12(1-\nu^2)} + \frac{\pi Eh}{1-\nu^2} \left(\frac{425\nu w_0^4}{3969a^2} - \frac{222\nu^2 w_0^4}{3157a^2} + \frac{1501w_0^4}{7938a^2} \right) - \frac{1}{3}\pi Pa^2 w_0 \quad 4.48$$

From $dU/dw_0=0$, we find the following load-deflection relation:

$$P = \frac{Eh^3}{12(1-\nu^2)} \frac{64w_0}{a^4} + \frac{Eh}{1-\nu^2} \frac{w_0^3}{a^4} \left\{ \frac{1700\nu}{1323} - \frac{589\nu^2}{698} + \frac{1813}{799} \right\} \quad 4.49$$

Again a cubic function in which w_0 is the centre-deflection of the membrane.

4.3 Membrane Deflection

From the membrane load-deflection behavior described by expressions 4.28 and 4.48 we are able to obtain the deflection of the membrane as function of the applied load. In this section the load-deflection of both membrane configurations will be derived, and the load-deflection behavior as approximated by the analytical approximation will be compared with the load-deflection behavior as approximated numerically (Finite Element Model).

4.3.1 Dogbone configuration

Figure 34 shows the deflection of the dogbone membrane at a prescribed $5kPa$ pressure. Notice the resemblance of centre-deflection in the validation with the Finite Element Model shown in Figure 35. The Analytical Model predicts a centre-deflection of $264.84\mu m$ (concerning a $16.5\mu m$ thick membrane; Appendix 3). The Finite Element Model (Appendix 1) predicts a centre-deflection of $269.95\mu m$.

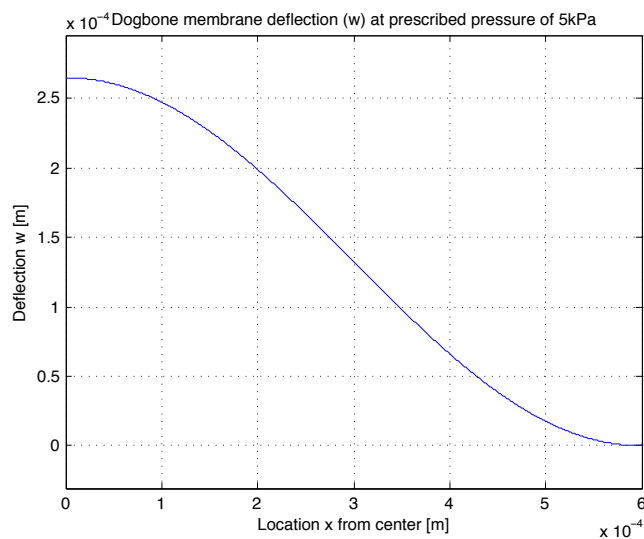


Figure 34: Graph indicating the analytically approximated deflection of the dogbone membrane as function of location when a pressure of $5kPa$ is applied. Notice the correspondence in centre-deflection with the finite element approximation depicted in Figure 35. Notice however also that the analytical approximation deviates slightly in deflection course, the effect of the clamped edges appears to be much greater when approximated analytically.

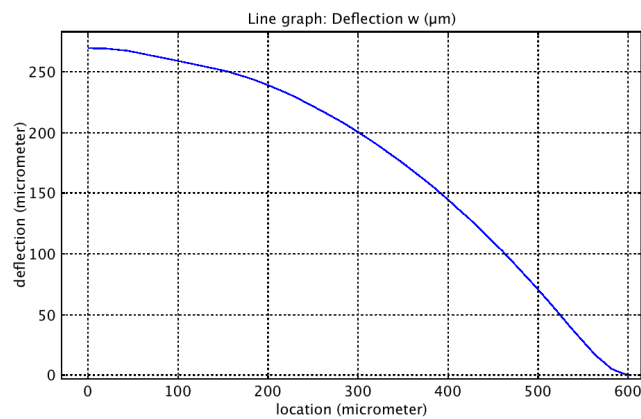


Figure 35: Graph indicating the numerically approximated deflection of the dogbone membrane as function of location when a pressure of $5kPa$ is applied. Notice the correspondence in centre-deflection with the analytical approximation depicted in Figure 34.

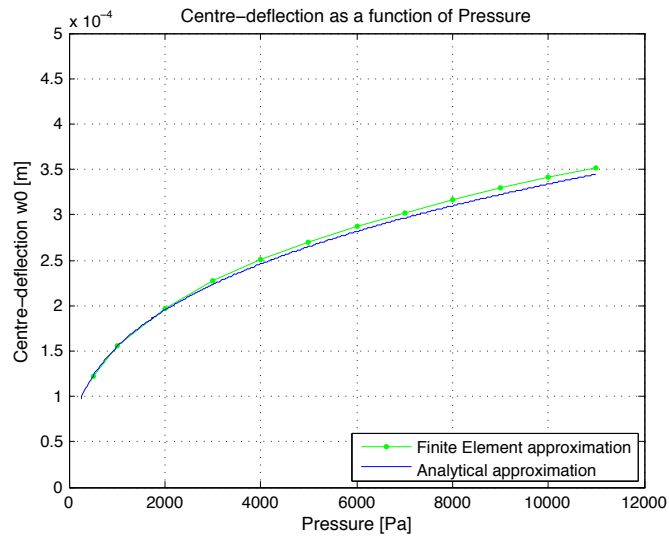


Figure 36: Graph depicting the centre-deflection of the dogbone membrane as function of applied pressure for both the numerical (green line) as analytical approximation (blue line). Notice the nice correspondence between the two models. The deviation we see is due to the smaller radius of bending around the edges in the numerical model.

Figure 36 shows the centre-deflection of the dogbone membrane as function of applied pressure for both numerical and analytical approximation. Notice that for various pressures the numerical approximation corresponds with the analytical approximation for a uniform $16.5\mu\text{m}$ thick uniform membrane. Furthermore, the membrane shows great flexibility, as it deflects up to approximately $350\mu\text{m}$ at an applied pressure of 10kPa .

4.3.2 Circular configuration

Figure 37 shows the deflection of the circular membrane at an applied pressure of 5kPa . We again see the similarity with the deflection results of the finite element approximation showed in Figure 38. We obtain a centre-deflection with use of the analytical model of $688.79\mu\text{m}$, which corresponds with the centre-deflection obtained from the finite element model of $629.91\mu\text{m}$. We should notice, however, that the effect of the clamped edges is more profound in the analytical model, compared with the numerical model.

In the numerical model (Figure 35 and Figure 38), we witness the clamped edges in the fact that the membrane leaves the edges under a zero tangent. The tangent however increases fast when going inward. In the analytical model (Figure 34 and Figure 37), we witness a slower increase in tangent. The finite element model seems to behave almost as a simply supported membrane, almost eliminating the bending term of the strain energy.

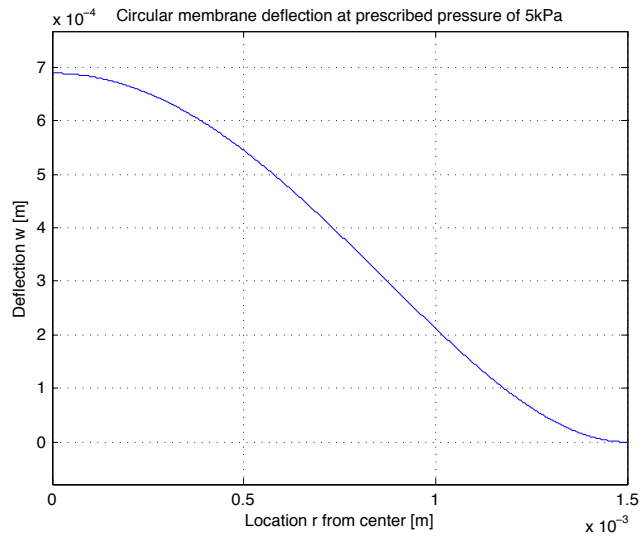


Figure 37: Graph indicating the analytically approximated deflection of the circular membrane as function of location when a pressure of 5kPa is applied. Notice the correspondence in centre-deflection with the finite element approximation depicted in Figure 38. Notice however also that also in the circular case the analytical approximation deviates slightly in deflection course, the effect of the clamped edges appears to be much greater when approximated analytically.

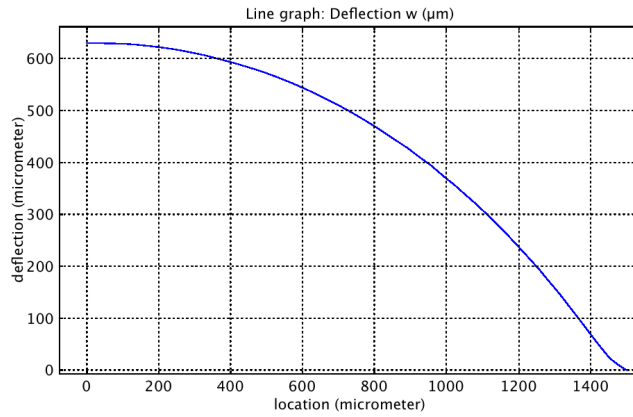


Figure 38: Graph indicating the numerically approximated deflection of the circular membrane as function of location when a pressure of 5kPa is applied. Notice the correspondence in centre-deflection with the analytical approximation depicted in Figure 37.

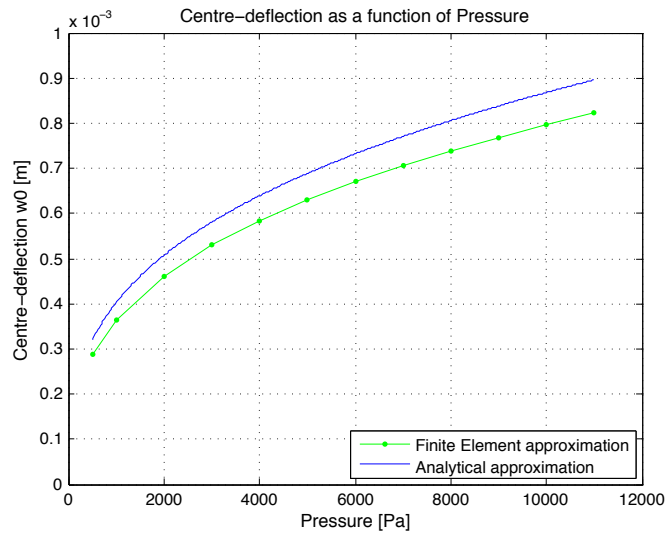


Figure 39: Graph depicting the centre-deflection of the circular membrane as function of applied pressure for both the numerical (green line) and analytical approximation (blue line). Notice that in the case of the circular membrane the line of the numerical approximation is situated below the line of the analytical approximation. This is contradictory to the case of the dogbone, furthermore one would expect due to the smaller radius of bending at the edges that the line of the numerical approximation would be above the line of the analytical approximation. However, we determine the compliancy here solely by centre-deflection, for the correct determination of the deflection (and thus compliancy), the deflection should be integrated over the total area of the membrane, and not solely centre-deflection should be taken into account.

Figure 39 shows the centre-deflection of the circular membrane as function of applied pressure for both numerical and analytical approximation. For various pressures the numerical approximation corresponds with the analytical approximation for a uniform $21.5\mu\text{m}$ thick uniform membrane. Notice, however, that for the dogbone membrane, the finite element model is slightly more compliant, whereas for the circular membrane the analytical model shows a higher compliancy.

One would expect a higher compliancy of the finite element model, as the transition area (bending area) situated at the edges is smaller. However, we define the compliancy here by looking at the centre-deflection, whereas actually the entire deflection plays a role in the compliancy of the membrane. To properly describe the compliancy of the membrane, we should describe the compliancy by integration of the deflection over the total area of the membrane. We can also determine, by looking at the two deflection curves (Figure 37 and Figure 38), that this is the case with the circular membrane and in smaller extend also with the dogbone membrane. The numerical model (Figure 38) shows lower deflection in the centre. However, approximately $400\mu\text{m}$ from the centre outward, the numerical model shows a higher deflection.

4.4 Membrane Strain

From the in plane strain components described by the expressions 3.24, 4.33 and 4.34, together with the membrane load-deflection behavior described by expressions 4.28 and 4.48 we are able to obtain the strain components of the membrane as function of the applied load. In this section the in plane strain components of both membrane configurations will be derived, and the strain behavior as approximated by the analytical approximation will be compared with the strain behavior as approximated numerically (Finite Element Model).

4.4.1 Dogbone configuration

The axial strain in the membrane is, as earlier stated, a combined function of the strain due to membrane bending and the strain due to axial stretching. Both displacements in z - (Figure 28) as well as x -direction (Figure 29) influence the strain in the membrane. As earlier mentioned, we obtain a displacement in x -direction from the centre towards the edge in the centre section of the membrane, and from the edge toward the centre in the outer section of the membrane. Resulting this material movement, a part of the membrane only moves up and downwards. This displacement u has a big influence on the strain distribution over the membrane. Figure 40 represents the relation between applied pressure (y -axis), the axial strain (z -axis) and the x -coordinate (location on the membrane, x -axis), due to bending and stretching (thickness $16.5\mu\text{m}$, Appendix 3).

We obtain a non-uniform strain distribution in the membrane, increasing in range with higher pressures. This non-uniformity can be more easily witnessed from Figure 41, where the axial strain as function of the location is expressed for several pressures. Notice the characteristic wave pattern, with a local maximum in the middle. This local maximum seems to correspond with the sign transition in u -displacement (Figure 29).

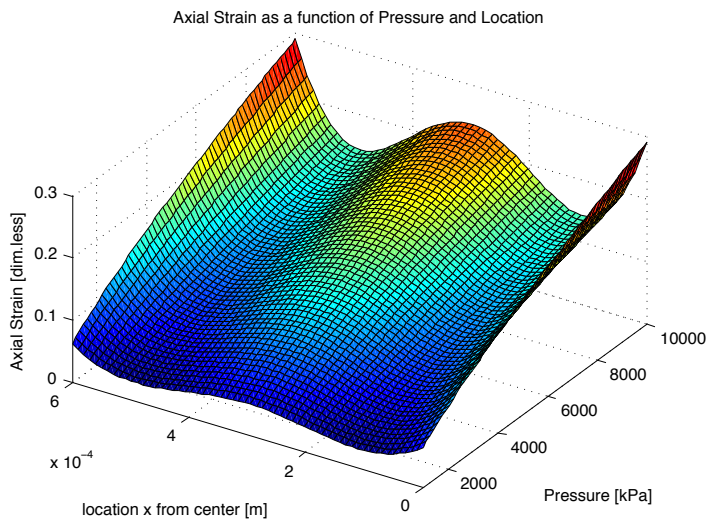


Figure 40: Graph depicting the relation between applied pressure (y -axis), the axial strain (z -axis) and the x -coordinate (location on the membrane, x -axis), due to bending and stretching for the dogbone membrane. Notice the non-uniform strain distribution, increasing in range with increasing pressure.

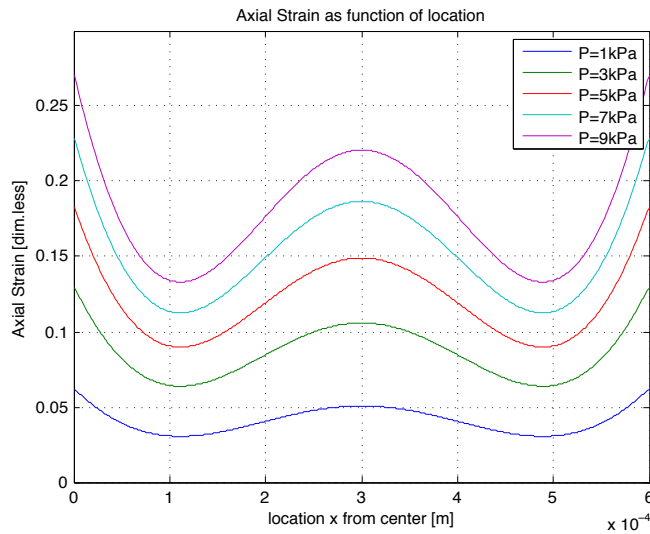


Figure 41: Graph depicting the axial strain as function of the location is for various pressures. Notice the characteristic wave pattern, with a local maximum in the middle. This local maximum seems to correspond with the sign transition in u -displacement.

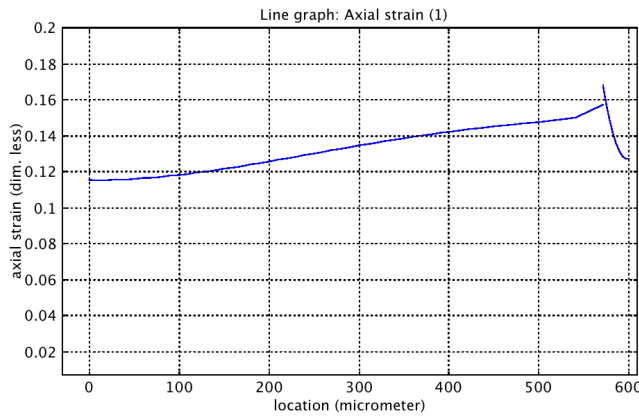


Figure 42: Graph depicting the strain distribution in x -direction as approximated by the finite element model at an applied pressure of $5kPa$. Notice that the characteristic wave pattern we have seen in the outcomes of the analytical model does not occur in the numerical model. The outcome of the numerical model shows more what we would expect, a rather uniform strain distribution.

The strain distribution in x -direction as approximated by the finite element model, is shown in Figure 42. Chosen is to show this membrane strain by means of a graph indicating the axial strain in the neutral line. From this representation the strain distribution can be easily compared with the strain as approximated by the analytical model. In Appendix 3 the strain distribution of the membrane including and excluding grooves are presented. Where we can note that the uniform thickness representation shows strain similarity with the grooved model, when we look at the overall membrane strain. The axial strain (x -direction) as approximated by the finite element model, shows to be different from the axial strain as approximated by the analytical model. The characteristic wave pattern, as witnessed in the analytical model, does not occur in the finite element model. The axial strain as approximated by the finite element model shows a behavior more like we would expect; a rather homogeneous distribution. Large strain deviation only occurs at the clamped edges.

The logic behind the variable strain distribution in the analytical approximation is hard to understand. When considering a flexible, thin membrane, under large deflection, one would expect the stretch term to take the overhand. The strain in a double clamped element would then in axial direction become more or less uniform. The only non-uniformity that could occur

would be in the edge region, where more bending exists. This is exactly what the finite element model predicts. In order to better understand the outcome of the analytical model, displacement field variations are done.

4.4.1.1 Displacement field variation

As can be witnessed from Figure 43 and Figure 44, the deflection approximated with the analytical model for the dogbone membrane does not exactly resemble the actual measured deflection of the membranes during experiments. When comparing the actual membrane deflection obtained by a microscope (Figure 43) with the deflection function obtained by the analytical model (Figure 44), we notice some error near the clamped edges.



Figure 43: Image obtained by the microscope of the dogbone membrane including grooves. Notice that in the centre region the membrane seems to leave the edges under a considerable angle. The effect of the clamped edges appears to be extremely small.

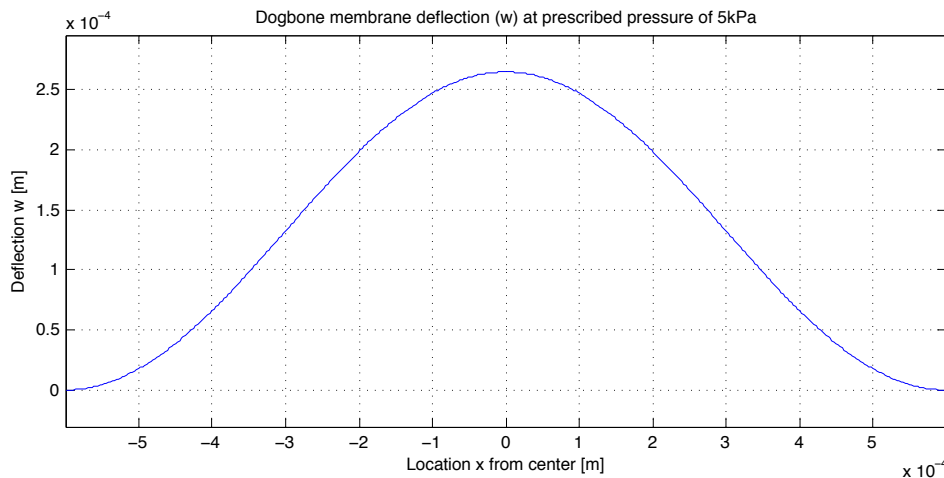


Figure 44: Graph indicating the deflection of the dogbone membrane in the central region, $x=0$ defines the centre of the membrane. Notice that the analytical model approaches the edges with a zero tangent, unlike the actual deflection Figure 43.

Similar to the finite element model (Figure 38), the actual membrane deflection does not show a transition region, it appears to leave almost immediately under a considerable angle. This proves the assumption that for thin membranes subjected to large deflections the bending strain plays little to no role in the axial strain. The analytical model, however, describes the clamped edges with a zero-tangent when approaching the edge. The contribution of the bending strain to the axial strain as follows from the deflection of the membrane will in reality thus be less than assumed in the analytical model.

This behavior can be approximated when considering the membrane simply supported instead of clamped at both ends. By approximating the edges as simply supported, we switch from plate theory to membrane theory. Plate theory is not able to describe the small radius of bending that occurs at the edges of a clamped membrane.

The true membrane behavior, however, will be in the middle of the two models. The clamped edges do not describe the behavior exact, however, simply supported edges will neither. The membrane does leave under a zero-tangent, although the small tangent only exists in a small outer part of the deflected membrane.

The first variation in the displacement field is thus actually a variation in the boundary conditions, with the displacement field changing corresponding to these boundary conditions. We consider the boundary conditions as follows:

$$\frac{\partial \hat{w}}{\partial x} = 0 \xrightarrow{\text{for}} x = 0 \quad 4.50$$

$$\frac{\partial^2 \hat{w}}{\partial x^2} = 0 \xrightarrow{\text{for}} x = \pm \frac{L}{2} \quad 4.51$$

$$\hat{u} = 0 \xrightarrow{\text{for}} x = \pm \frac{L}{2} \quad 4.52$$

$$\hat{w} = 0 \xrightarrow{\text{for}} x = \pm \frac{L}{2} \quad 4.53$$

In which the second condition (condition 4.50) states that the rotations at the supported edges are unrestricted. The following kinematically admissible (satisfies the boundary conditions) displacement function w will replace function 4.5 when considering a simply supported element of the dogbone membrane:

$$\hat{w} = w_0 \left(1 - \frac{2(3+\nu)}{5+\nu} \frac{x^2}{(L/2)^2} + \frac{1+\nu}{5+\nu} \frac{x^4}{(L/2)^4} \right) \quad 4.54$$

$$\hat{w} = w_0 \left(1 - 2P \frac{x^2}{(L/2)^2} + Q \frac{x^4}{(L/2)^4} \right) \quad 4.55$$

From the clamped case we have seen that the deflected shape of the circular membrane is similar to the deflected shape of the dogbone membrane. For simplification, we now use the same trial displacement function for the circular case as well as the dogbone membrane. The trial displacement function is obtained from the trial displacement function 4.13 for the circular clamped case. In the clamped case $P=Q=1$ in Equation 4.54.

Secondly we will vary the displacement in x -direction (u -displacement). As stated earlier, we can describe the displacement u by a simple polynomial function containing several terms (Eq. 4.7), each refining the function. The refinements reduce the error of the function. Initially we took two terms of this polynomial function. However, to reduce the error we now also look at the polynomial, taking 5 terms into account.

$$\hat{u} = x \left(\frac{L}{2} - x \right) \left(c_1 + c_2 x + c_3 x^2 + c_4 x^3 + c_5 x^4 \right) \quad 4.56$$

Figure 45 shows the deflection in z -direction (w), for each of the four displacement fields, at a prescribed pressure of $5kPa$. Notice that, although the centre-deflection w_0 is determined by the derivation of the total strain energy, and thus also depends on the displacement function u , the deflection does not vary with varying trial function u .

The displacement function 4.53 properly describes the supported edges, leaving rotation at the edges free. Obviously the model with the supported edges shows a higher centre-deflection, as the deflection is restricted less in the edge area.

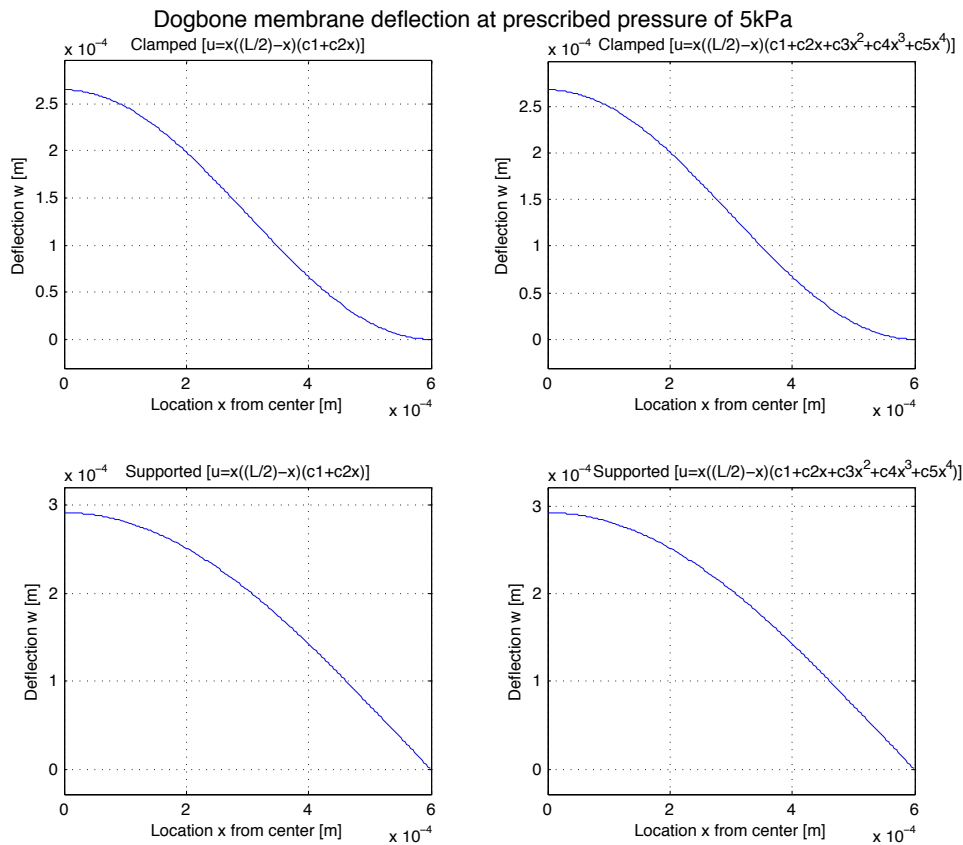


Figure 45: Deflection in z-direction (w), for each of the four displacement fields, at a prescribed pressure of 5kPa. Notice that, although the centre-deflection w_c is determined by the derivation of the total strain energy, and thus also depends on the displacement function u , the deflection does not vary with varying trial function u .

When we compare the deflection of the four models with the deflection of the finite element model (Figure 35), we can conclude that the finite element model lies in between the supported and the clamped analytical model.

Figure 46 shows the displacement in x-direction (u), for each of the displacement field, at an applied pressure of 5kPa. The extra terms in the trial function u do not show any big transformation in the derived u -displacement. A significant transformation of the displacement u occurs though, when considering simply supported edges with respect to clamped edges. Because of the free rotations at the edges, a negative displacement u obviously does not occur.

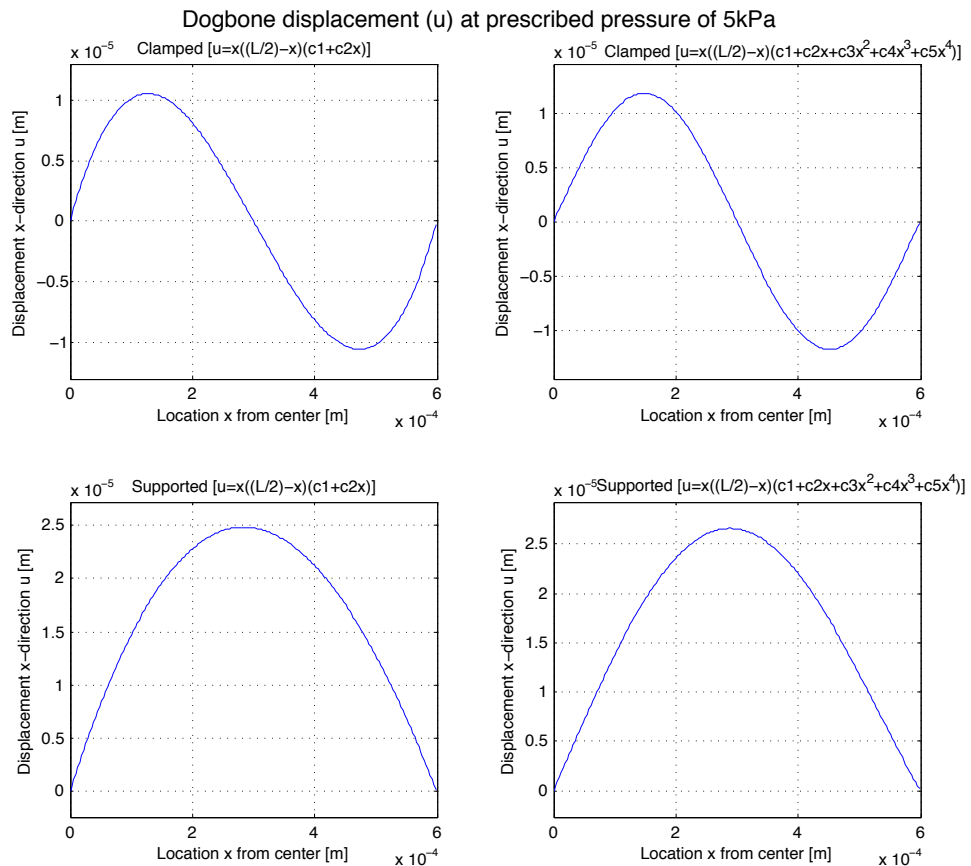


Figure 46: Displacement in x -direction (u), for each of the displacement field variations of the dogbone membrane, at an applied pressure of 5kPa. Notice that the extra terms in the trial function u do not show any big transformation in the derived u -displacement. A significant transformation of the displacement u occurs though, when considering simply supported edges with respect to clamped edges. Because of the free rotations at the edges, a negative displacement u obviously does not occur.

When we now compare the displacement in u direction of the four models (Figure 46) with the displacement u of the numerical model shown in Figure 47. Notice that the numerical approximation predicts a displacement in x -direction that lies between the predictions of the analytical models for clamped and supported edges. The behavior tends to the behavior of the analytical supported model, however in the edge section you can find the clamped edge effect. The displacement, however, does not turn negative in the edge region.

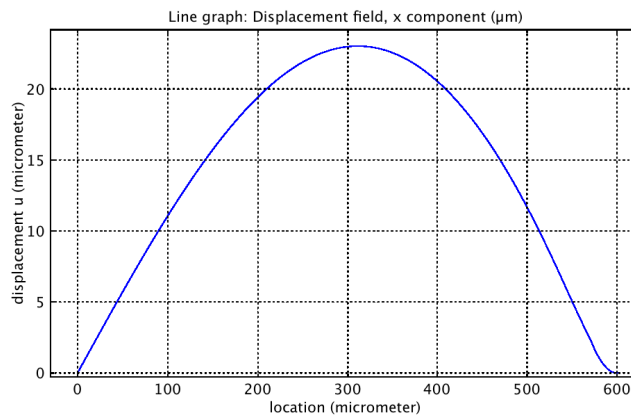


Figure 47: Displacement u as approximated by the numerical model. Notice that the numerical approximation shows mainly resemblance with the simply supported analytical model, however, still some effects occur at the edges.

The effect of the refinement of the displacement function u , by adding terms, becomes obvious when we look at the strain distribution over the membrane (Figure 48).

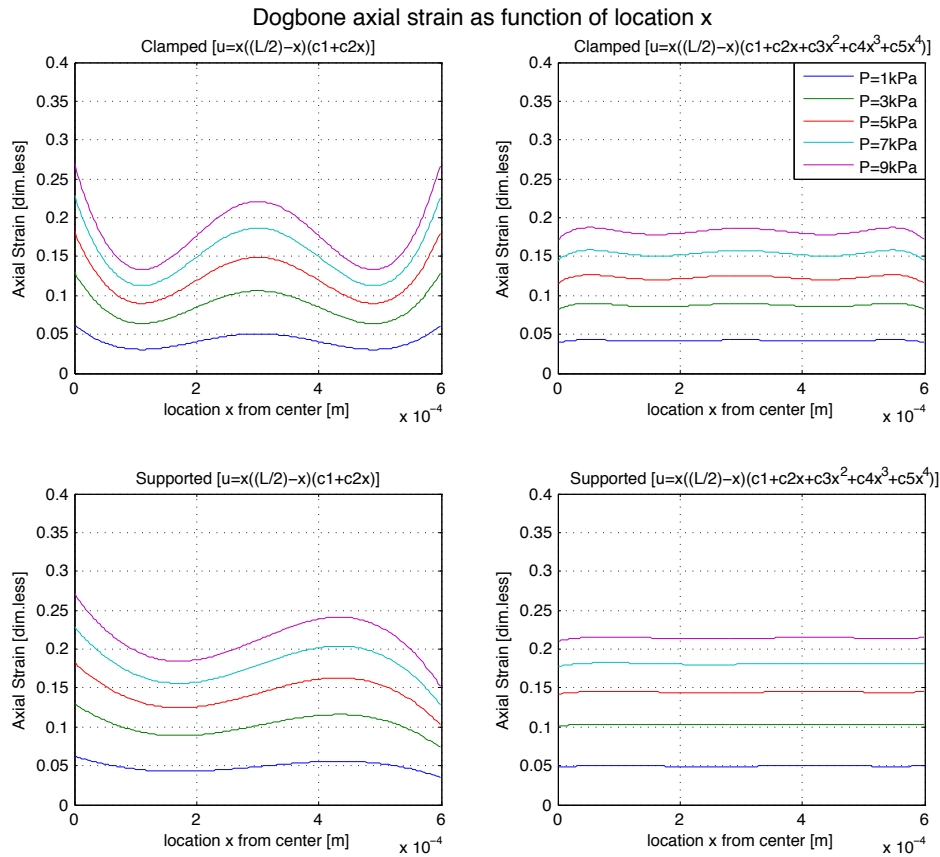


Figure 48: Strain approximation of the four analytical models as function of location (x), for various pressures. Notice that the effect of the refinement of the displacement function u , by adding terms, becomes obvious when we look at the strain distribution over the membrane.

The characteristic wave pattern, which we obtain when we only use two terms in the displacement function in x -direction, is greatly reduced when we include 5 terms. Expected is a homogeneous strain distribution over the membrane, because the bending term in the strain energy plays little to no role when considering a thin flexible membrane. We obtain that homogeneous distribution of strain when adding additional terms to the displacement function u .

Comparing the strain approximation of the analytical models (Figure 48) above, with the strain approximation of the numerical model (Figure 42), we can again conclude that the numerical strain distribution lies in between the strain distributions of the clamped and the supported analytical model, containing 5 terms in the u displacement function. The strain obtained by the numerical model in the central region tends to the strain obtained by the clamped analytical model. The strain obtained by the numerical model in the outer region tends to the strain obtained by the simply supported analytical model.

The asymptotic behavior, as a result from the small radius bending (due to the clamped edges), in case of the numerical model, does not appear in the results of the analytical models. When we zoom in on this area in the numerical model¹ (Figure 49), we can see that in these edge regions (very near to the edge, small region), the numerical model shows an

¹ Here we make use of the two dimensional representation (not containing shell elements), to be able to show the distribution over the thickness. Figure 42 is obtained from the shell model.

asymmetric behavior around the mid-plane (black line), where we would expect a symmetric behavior.

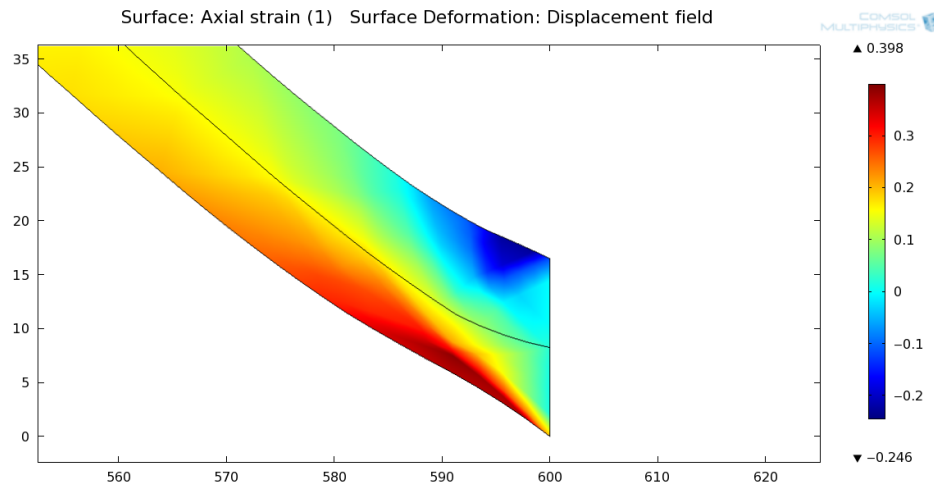


Figure 49: Close up of the numerical model near the edges. Notice that in the edge regions (very near to the edge, small region), the numerical model shows an asymmetric behavior around the mid-plane (black line), where we would expect a symmetric behavior.

This asymmetric behavior occurs due to the fact that instead of using classical deformation theory, a shear deformation theory is applied. In the classical deformation theory, as used for the analytical model, the assumption is made that plane sections, initially normal to the mid surface before deformation, remain plane, and normal to that surface after deformation. In the classical deformation theory no shear deformation due to transverse forces is considered, only in plane deformations are considered.

When a shear deformation theory is applied we do consider shear deformation due to out of plane forces. Plane sections; initially normal to the mid surface do not necessarily remain plane and normal to that surface after deformation. The plane sections, initially normal to the mid surface are displaced by $z(x)$ and rotates by $\theta=(\theta_1(x),\theta_2(x))$.

The element used for the shell interface in comsol is of Mindlin-Reissner type, which means that in these shell models transverse shear deformation is accounted for. The transverse forces, creating these shear deformations, are proportional to the derivative of the moment to x . The moments approach zero in the largest part of the membrane, due to the negligible effect that the bending of the membrane has on the total strain energy. However, near the edges, due to the clamped boundary (and the related small radius of bending), the moment increases rapidly. This results in a large transverse force, leading to large shear deformations, thus leading to a different strain distribution near the clamped edges.

This differing behavior near the membrane's clamped edges occurs in a small region where no grooves exist. When plating a monolayer of cardiomyocytes on the membrane, we assume that the cells tend to anchor inside the grooves. We thus assume that this edge effect does not affect the cell stretch in a significant manner. Furthermore, the edge behavior we see in the finite element model is the behavior as calculated for the mid surface of the membrane. The cardiomyocytes will anchor on the top surface of the membrane. Notice, from Figure 49 that on the top surface of the membrane the strain decreases and even turns into a compression. We can thus conclude that we do not have to consider possible overstretch of the cardiomyocytes near the edges. We are thus able to focus on the overall strain as predicted by the analytical model, without further complicating this model.

With this homogeneous axial strain distribution in the dogbone membrane, we are able to describe the axial strain as function of the load applied. This enables us to define the optimal pressure to be applied for to obtain the 14.7 percent stretch (Section 2.2.3) on the cardiomyocytes as desired. Figure 50 shows this load-strain behavior.

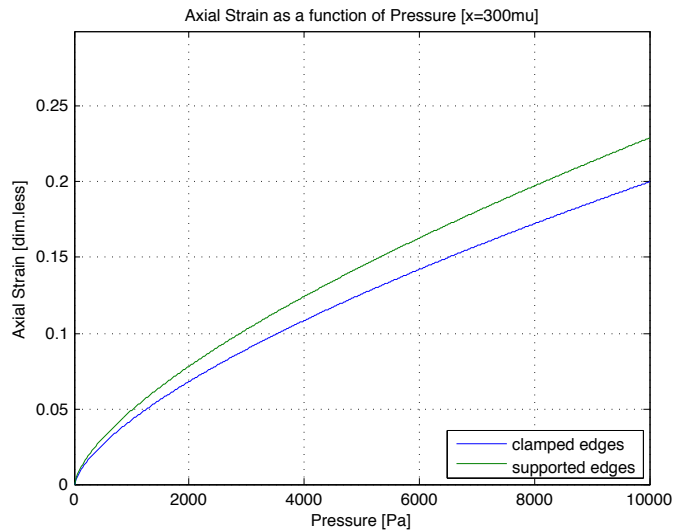


Figure 50: Load-strain behavior; the axial strain as function of the load applied. Notice the change from an exponential increase to a more linear relation, in the exponential part the bending strain is leading, in contrary to the linear region where the stretching strain is leading.

Notice the change from an exponential increase to a more linear relation, in the exponential part the bending strain is leading, in contrary to the linear region where the stretching strain is leading. One can see that up from an applied pressure of approximately 3 kPa the strain due to stretch is leading in the axial strain of the membrane and the bending strain has little to no influence on the axial strain.

For the determination of the pressure for the optimal the ceiling value will be considered, in order to be sure not to overstretch the cells initially.

4.4.2 Circular configuration

For the circular configuration we obtain two strain components, the component in radial direction (Eq. 4.33) and the component in transverse direction (Eq. 4.34). This corresponds with respectively the longitudinal and transverse strain on the cardiomyocytes (considering grooves running radial). A similar strain distribution will be expected for the radial strain as for the dogbone case (Figure 40) when considering the initial displacement field and boundary conditions. This similarity will be expected due to similarity of the displacement field, and the same way of calculating this radial strain with respect to the axial strain in the dogbone case. The radial strain distribution belonging to the initial conditions, for the circular configuration can be witnessed in Figure 51. We obtain the same illogical characteristic wave pattern. For this reason we immediately start varying the displacement field.

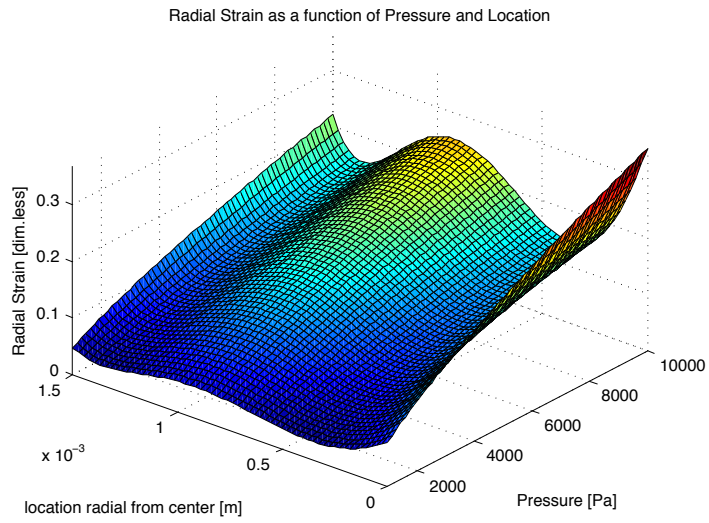


Figure 51: Radial strain distribution of the circular membrane as function of applied pressure. Notice that we obtain an expected similar non-uniform strain distribution as we have seen in the dogbone case.

4.4.2.1 Displacement field variation

Similar to the dogbone case, when we closely look at the boundaries of the circular membrane, and comparing the actual membrane deflection obtained by a microscope (Fig. 2.4.1-2.4.4) with the deflection function obtained by the Analytical model (Fig. 2.4.5-2.4.6), we notice again the same error near the clamped edges.

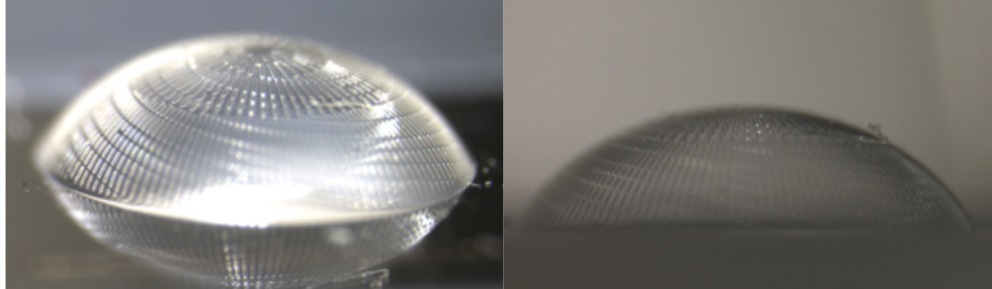


Figure 52: Two images showing the actual circular membrane deflection. Notice that, similar to the dogbone membrane, the membrane seems to leave the edges under a considerable angle, the clamped edges seem to have little to no effect.

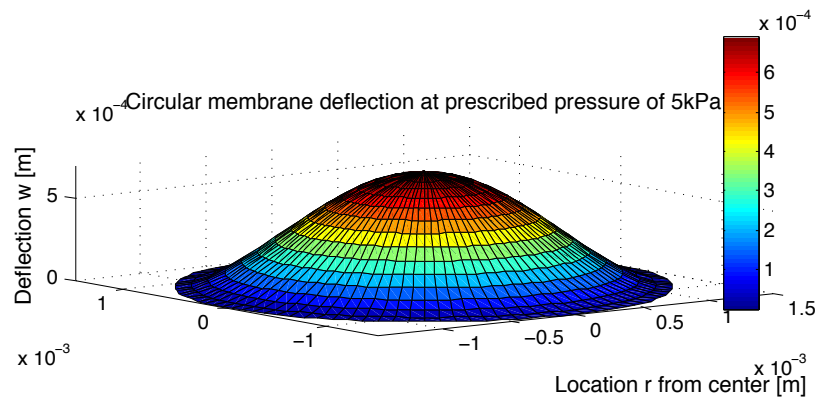


Figure 53: Circular membrane deflection as predicted by the analytical model. Notice that in contrary with the actual membrane, the analytical model predicts a large transition area from the edge inward.

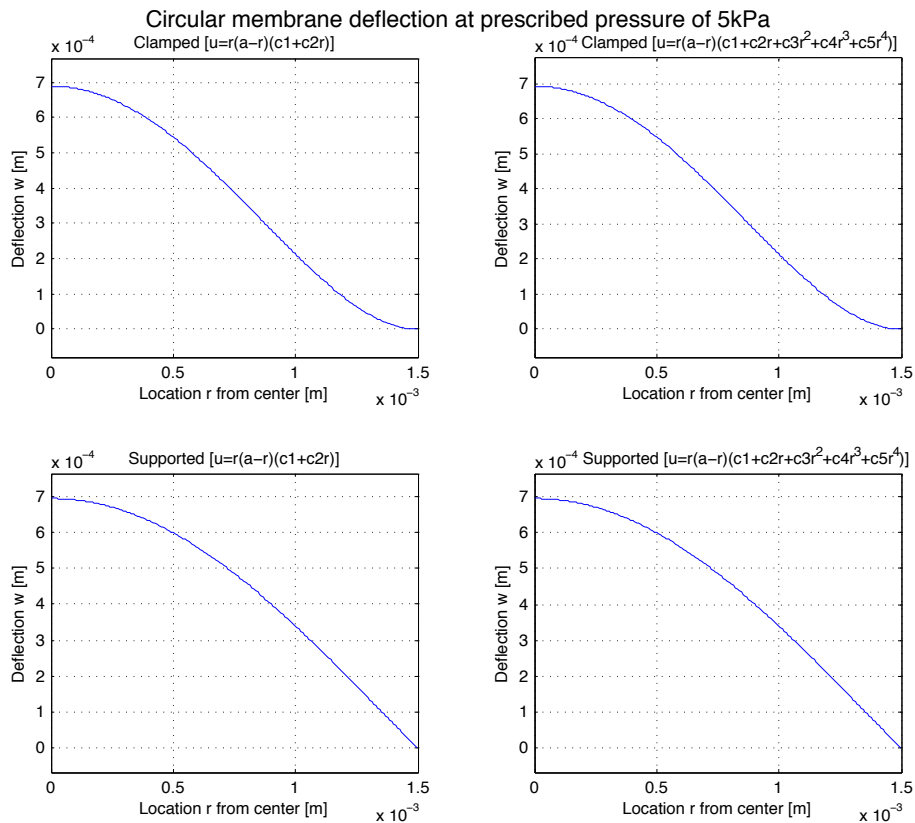


Figure 54: Deflection of the membrane as function of location (r) at an applied pressure of $5kPa$ as predicted by the analytical model, for the four different displacement cases. Notice that the supported boundary condition shows a slightly higher deflection, although it is not as big a difference as in the dogbone case. However, we should note that again we are solely considering centre-deflection as compared to the integrated deflection.

Where the Analytical model describes the clamped edges with a zero-tangent when approaching the edge, the actual membrane leaves almost immediately under a considerable angle.

We again model the membrane behavior with two different boundary conditions. We consider clamped edges, from which we have seen that this model is not fully able to describe the small radius bending at the edges. Furthermore, we consider simply supported edges, switching from thin plate behavior to membrane behavior. Where we expect the real behavior to resemble a combination of the two, as bending does exist at the edges.

Furthermore, we vary the radial displacement function u . We expect that refinement of the radial displacement function, similar to the dogbone case, will correct the membrane stain to a more accurate distribution.

Figure 54 shows the deflection of the membrane as predicted by the analytical model, for the four different displacement cases.

The supported boundary condition shows a slightly higher deflection, the deflection difference however is not as big as we have seen in the dogbone case (Figure 45). As mentioned before, the compliancy cannot be expressed accurately in terms of centre-deflection; we should consider the deflection integrated over the area. When we consider the deflection deviation further towards the edges, we see a bigger difference. Thus we can state that the overall deflection of the simply supported model is higher than the deflection of the clamped model. The deflection distribution described by the supported model shows better similarity with the finite element approximation (Figure 38). However, the edge effects as predicted by the clamped analytical model should be taken into account.

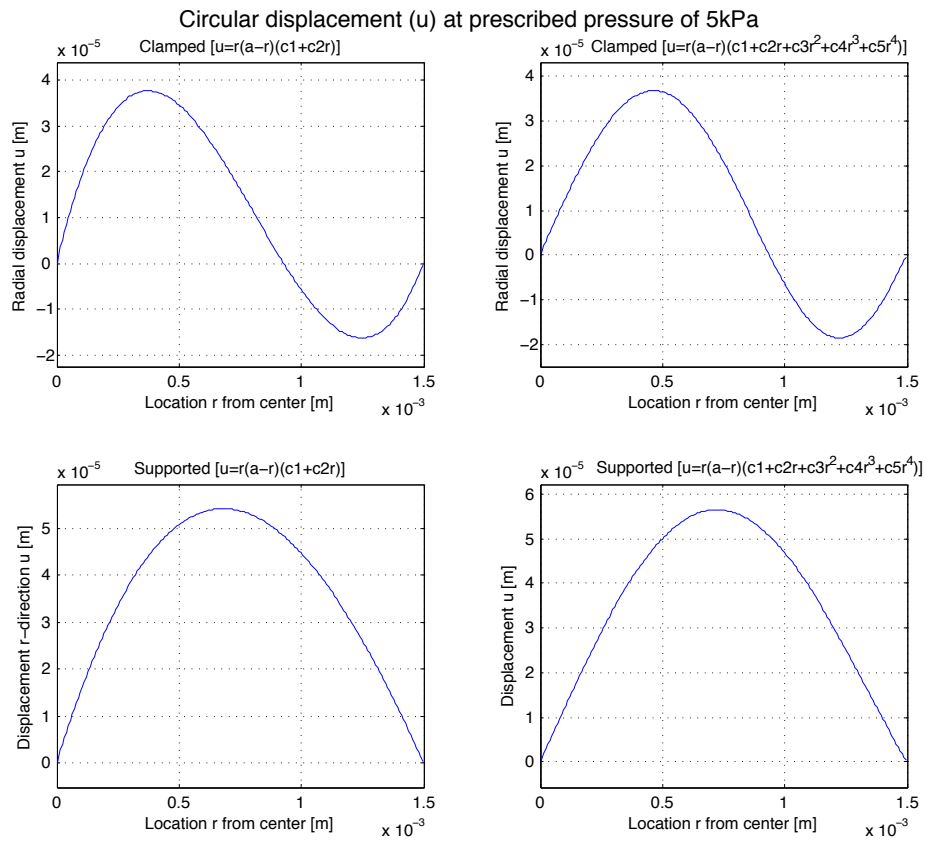


Figure 55: The displacement u , in radial direction, of the four displacement cases. We again notice that the extra terms in the trial function u do not show any big transformation in the derived u -displacement. The only significant transformation of the displacement u we see is due to the boundary conditions.

Figure 55 shows the displacement in radial direction (u), for each of the displacement cases. We again notice that the extra terms in the trial function u do not show any big transformation in the derived u -displacement. The only significant transformation of the displacement u we see is due to the boundary conditions. The free rotations at the edges eliminate extreme bending at the edges and thus negative u values.

We compare the displacement u of the four displacement cases with the displacement u as approximated numerically (Figure 56). Notice that the finite element approximation resembles the analytical model with simply supported edges even more than in the dogbone case. The exponential decrease we see in the dogbone numerical approximation, relating to the clamped edges, has reduced in the circular case. The explanation for this is that the circular membrane has a smaller thickness-area ratio, leading to a smaller contribution of the bending strain energy as compared with the dogbone membrane.

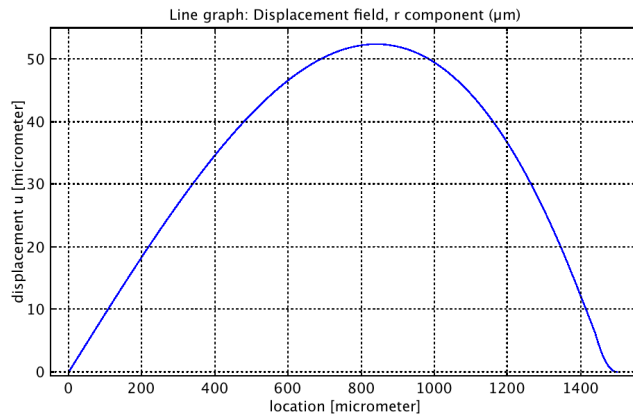


Figure 56: displacement u approximated numerically as function of location (r) at an applied pressure of $5kPa$. Notice again the resemblance with the simply supported analytical model. Furthermore, the edge effect as seen in the u displacement as approximated by the numerical model for the dogbone membrane almost disappears here.

Circular radial strain as function of location r

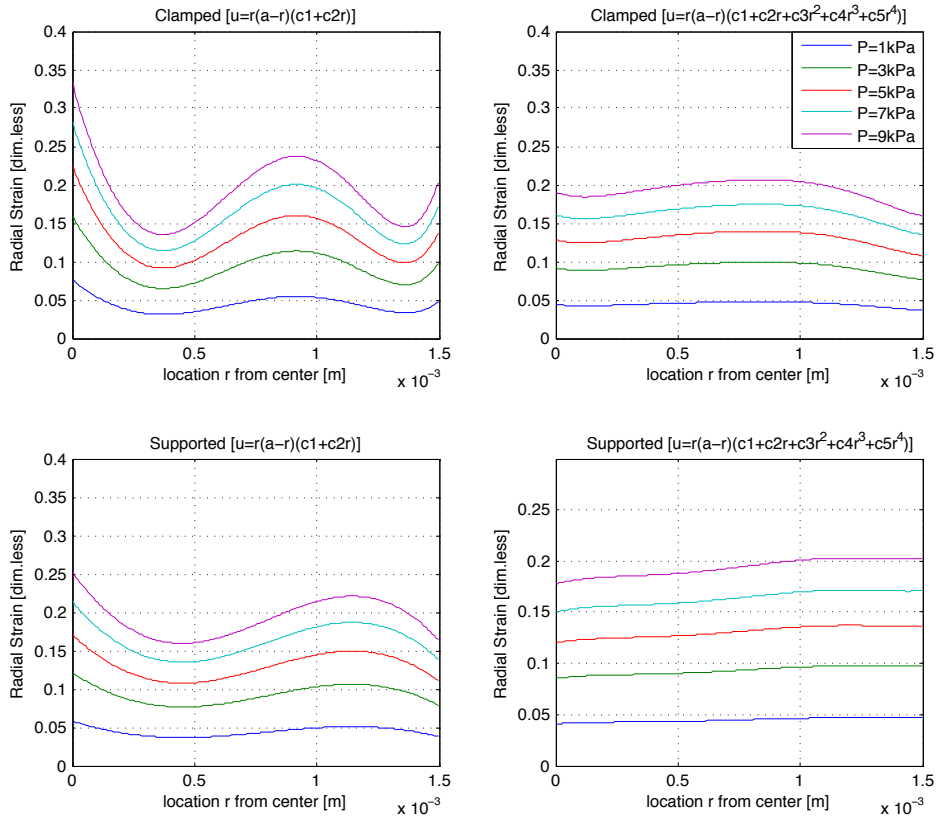


Figure 57: Radial strain of the circular membrane as function of location (r) for the different displacement fields, at various applied pressures. Notice that the characteristic wave pattern, which we obtain when we only use two terms in the displacement function in r -direction, is again greatly reduced when we include 5 terms.

We are thus able to describe the behavior of the circular membrane almost completely by membrane theory instead of plate theory, leaving out any bending terms. We can only neglect all bending terms when we consider large deflection (at large applied pressure).

Figure 57 shows the radial strain of the circular membrane at various applied pressures. Notice that the characteristic wave pattern, which we obtain when we only use two terms in the displacement function in r -direction, is again greatly reduced when we include 5 terms.

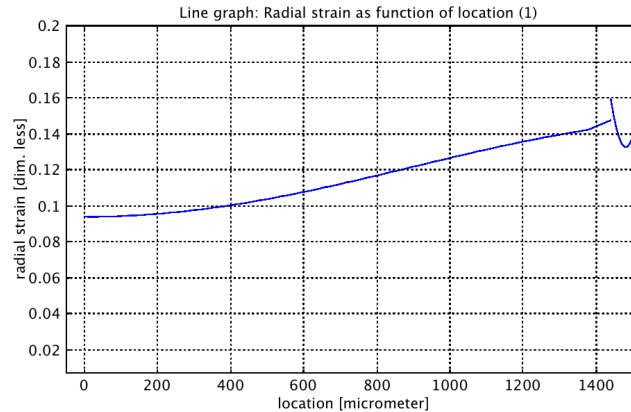


Figure 58: Strain approximation of the numerical model as function of the location (r) on of the membrane. Notice the correspondence with the strain distributions of the clamped and the supported analytical model, containing 5 terms in the u displacement function.

When we compare the strain approximation of the analytical models (Figure 57), with the strain approximation of the numerical model (Figure 58), we can again conclude that the numerical strain distribution lies in between the strain distributions of the clamped and the supported analytical model, containing 5 terms in the u displacement function. The distribution resembles the simply supported model, however we obtain a maximum strain (edge error excluded) more similar to the clamped analytical model.

Similar to the dogbone case, we are able to reject the edge effect, which occurs in the numerical model due to shear deformation. The edge effect, seen in Figure 58 will result in compression on the upper surface of the membrane, thus not resulting in overstretch of cardiomyocytes at the edge regions.

As previously stated, the cardiomyocytes on the circular membrane are not solely subjected to longitudinal strain; they also obtain strain in their transverse direction. The circular membrane introduces a multi-axial straining of the cardiac muscle cells. The cells will be stretched longitudinal by the radial strain of the membrane, as well as stretched transverse by the transverse strain of the membrane.

The transverse strain (Eq. 4.34) as function of location at various pressures for the four different displacement cases can be witnessed in Figure 59. Notice the high amount of transverse strain in the centre of the membrane, decreasing towards the edges. The increase results from the relative larger increase in circumference towards the centre of the membrane. The tangent approaches the radial direction near to the centre of the membrane, thus resulting in an increasing transverse strain near the centre of the membrane.

Furthermore, notice the multiple zero-strain areas, in case of the clamped edges. Obviously, no transverse strain exists totally at the membrane end, due to the fact that the edge is clamped. However another zero-strain point exists, where the displacement u in radial direction changes sign. A part of the circular membrane (ring) solely moves in a vertical direction, similar to the strip on the dogbone. Because of this vertical movement, and the negative radial displacement outward from this rigid ring, the outer membrane part shows a small negative strain. Sections move here from a ring with bigger diameter to a ring with a smaller diameter. In the case of low applied pressure, the compression is small compared to the tensile strain in the central region of the membrane. However, when applying a higher pressure to the membrane, this might be an effect we should consider.

Although, when we compare the outcomes of the several analytical models with the approximation of the finite element model in Figure 60, we notice that we can better describe the transverse strain behavior of the circular membrane when we consider the edges simply supported. Notice that in the finite element approximation the transverse strain does show a small exponential decrease near the edges, still indicating some effect due to the clamped edges. The simply supported model in Figure 59 obviously does not show such an effect, due to the free rotation at the edges.

We are thus also able to describe the transverse strain of the circular membrane by neglecting the edge bending terms. We can model the total behavior of the circular membrane by simply supported edges.

We should notice that the transverse strain, in contrary to the radial strain, depends highly on the radial coordinate. This means that cells centrally located will be subjected to higher transverse strain compared to cells located more peripheral.

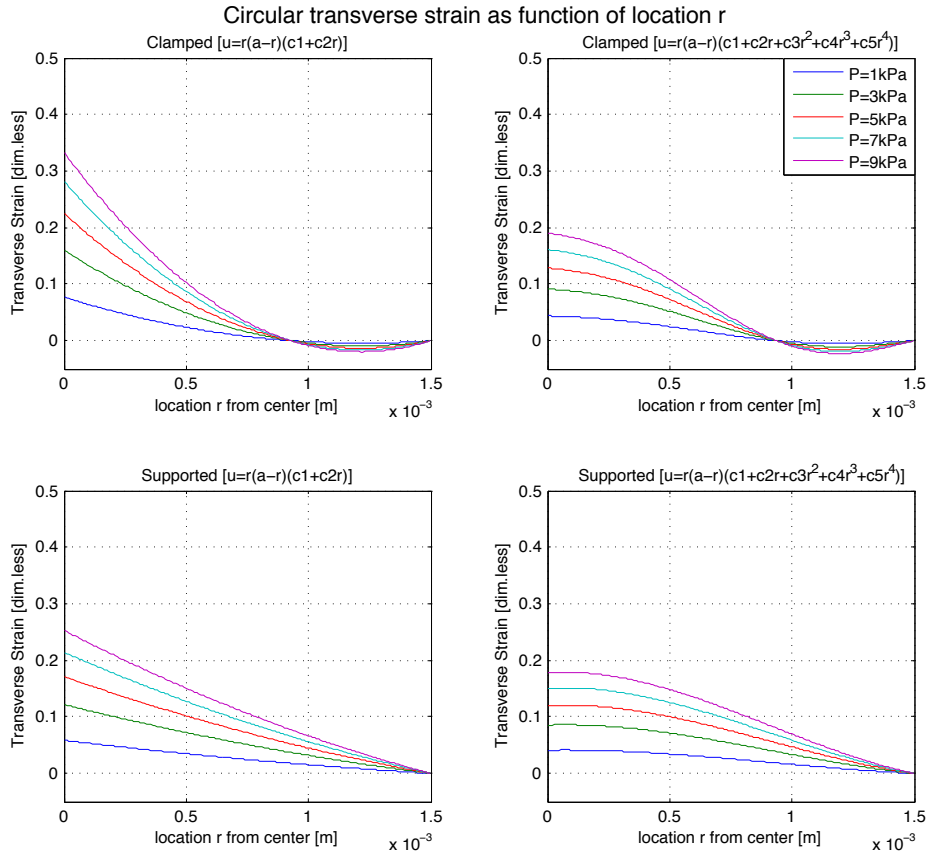


Figure 59: Transverse strain as function of location at various pressures for the four different displacement cases. Notice that in none of the four displacement cases the transverse strain is a uniform value. There will always be a transverse strain gradient in over the membrane in radial direction.

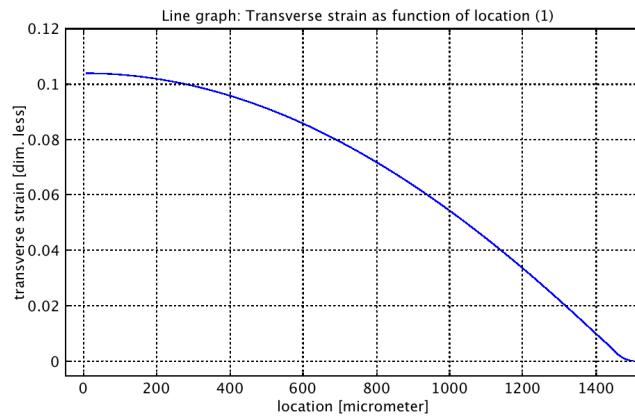


Figure 60: Transverse strain as function of location approximated numerically at an applied pressure of 5kPa. Notice that when we compare this graph with the previous one (Figure 59) we can describe the transverse strain behavior of the circular membrane most properly when we consider the edges simply supported.

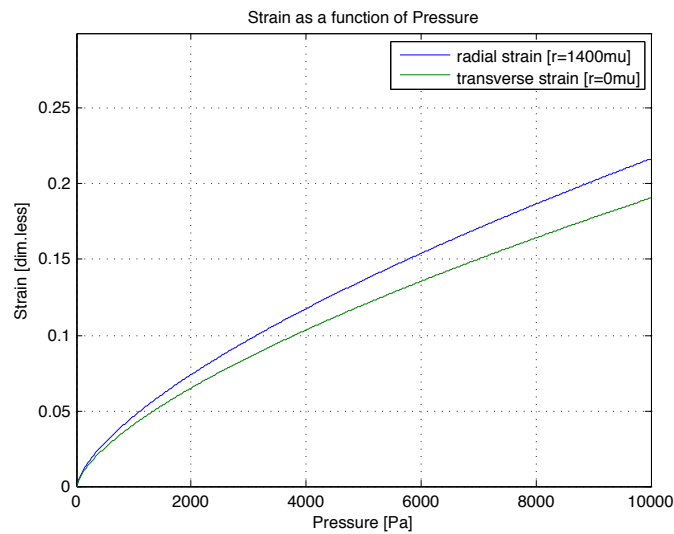


Figure 61: Both strain components as function of the applied pressure. The blue line denotes the radial strain as function of applied pressure; the green line represents the maximum transverse strain as function of pressure. We take the ceiling strain values in order not to overstretch the cardiac muscle cells.

We are now able to describe the two strain components as function of the applied pressure. Once again we will take the ceiling strain value in order not to overstretch the cardiac muscle cells. Figure 61 shows the maximal load-radial strain and load-transverse strain behavior.

Notice that we thus obtain a different load-strain behavior for the transverse direction with respect to the longitudinal direction. This will lead to a sub-optimal loading protocol for one of the two directions. Furthermore, we again see that for lower loading conditions the bending strain takes part in the total strain behavior of the membrane. However, for higher applied pressures, the bending strain energy can be neglected with respect to the extensional strain energy. The transition of the point where bending strain energy can be neglected is related to pressure, thickness to area ratio and elasticity modulus.

4.5 Experimental verification

For the validation of the Analytical Model, approximated experimental values are compared with both the Analytical and Finite Element approximations. The comparison is made in terms of centre-deflection, and in terms of the either x - or r -displacement of both membrane configurations.

4.5.1 Materials and methods

The experimental setup used (Figure 62), consists of a pressure box (Figure 63) connected to analogue regulated compressed air (Figure 64). For a better quantification of the applied pressure, the actual pressure in the box is measured by means of a pressure sensor. The voltage output of this pressure sensor is read out by a voltmeter, which relates to pressure by: $1V=6.9kPa$ (Figure 65).



Figure 62: Entire experimental setup.



Figure 63: Pressure box, to generate a constant pressure.



Figure 64: Analogue regulated compressed air, to fill the pressure box.

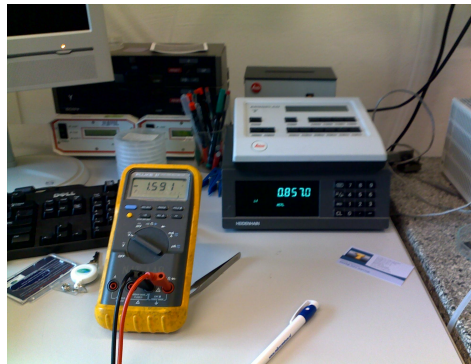


Figure 65: Voltmeter, measuring the voltage from a pressure sensor inside the box, for an accurate measure of the applied pressure.

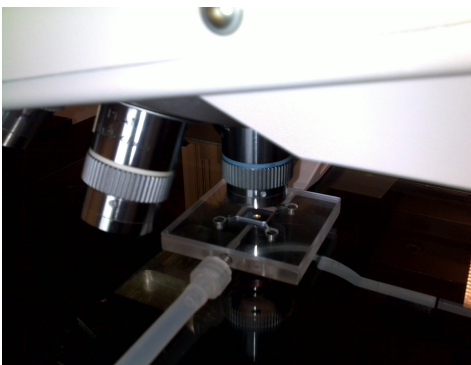


Figure 66: Chip holder consisting of two Plexiglas plates in between which the chip is clamped, and through which air is supplied.



Figure 67: The measurement of the table height (and thus deflection) when focussing visually, is done by a sensor situated underneath the table.

A single chip is clamped between two transparent plates (Figure 66), connected by a tube to the pressure box, the lower plate containing an air-tube ending below the membrane, for applying the pressure. The upper plate contains a rectangular hole to account for the deflection of the membrane and proper visualization. Visualization is realised by means of a Leica Ergoplan wafer inspection microscope.

The deflection of the membrane is obtained by measuring the table height, measured by a sensor below the table (Figure 67), and is indicated digitally (Figure 65, right). Deflection is set to zero, at visual focus in deflated condition between successive inflation. Deflection is determined by visual focus at various applied pressure in the range of 1 kPa - 11 kPa , with use of a magnification of $500\times$ (objective magnifying $50\times$).

The displacement in either x - or r -direction (displacement u) has been obtained by particle tracking. Black toner particles are randomly distributed on the membrane. With use of the Leica Ergoplan wafer inspection microscope, pictures are made of the membranes, at a magnification of $25\times$ (objective magnifying $2.5\times$). Several sequences of pictures (11) are obtained under several applied pressures, in the range between zero and 6.9 kPa .

For the tracking of the particles, from which the displacement function u is obtained, the PolyParticleTracker is used. The PolyParticleTracker is a versatile particle tracker, based on the "Polynomial Fit Gaussian Weight" (PFGW) method by S.S. Rogers *et al.* [54], and is written by S.S. Rogers at the University of Manchester Biological Physics Group in 2007. The PolyParticleTracker contains three Matlab M-files, and can be run via a graphical user interface. The PolyParticleTracker has been runned on Matlab version R2008b.

4.5.2 Deflection w

Figure 68 shows the experimental values for the centre-deflection of the dogbone membrane, as obtained by visual focus. We first notice that the centre-deflection progression of the actual membrane resembles the overall progression of both analytical and numerical models.

We subsequently compare the experimental, with the finite element and both clamped and simply supported analytical centre-deflections as function of applied pressure, for the dogbone membrane (Figure 69). Notice the centre-deflection resemblance between the three methods and the experimental derived values. The simply supported analytical model resembles the experimental deflection lapse over pressure most accurately.

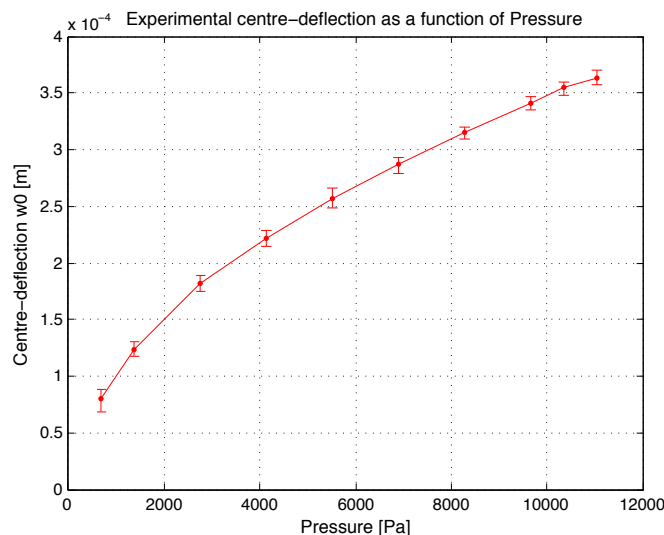


Figure 68: Experimental values for the centre-deflection of the dogbone membrane, as obtained by visual focus. Notice that the centre-deflection progression of the actual membrane resembles the overall progression of both analytical and numerical models.

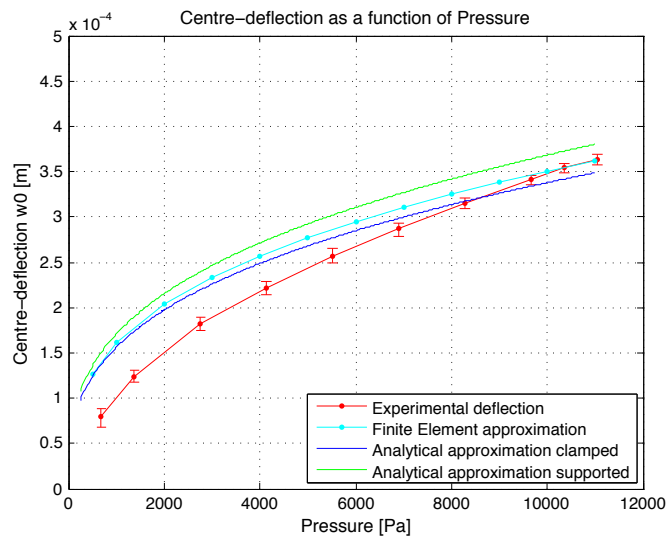


Figure 69: The experimental (red line), finite element (cyan line) and both clamped and simply supported analytical (resp. blue and green line) centre-deflections of the dogbone membrane as function of applied pressure, for the dogbone membrane. Notice the centre-deflection resemblance between the three methods and the experimental derived values. The simply supported analytical model resembles the experimental deflection lapse over pressure most accurately.

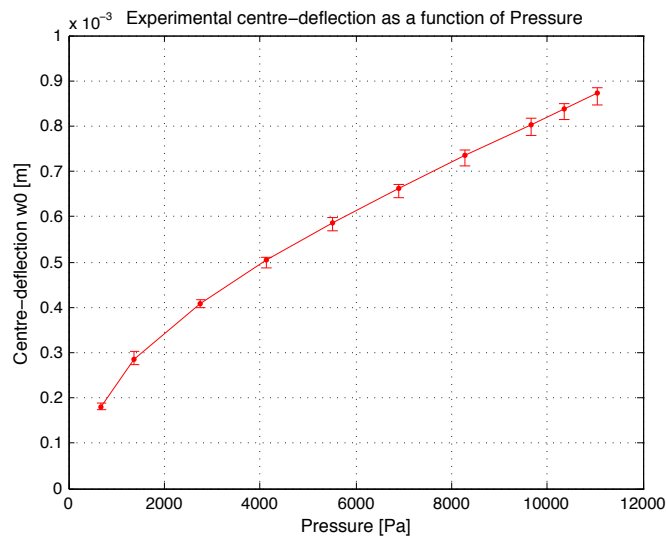


Figure 70: Experimental deflection of the circular membrane as obtained by visual focus. We again obtain a similar relation between pressure and deflection as we have seen in the analytical and numerical outcomes.

Figure 70 shows the experimental deflection of the circular membrane as obtained by visual focus. We again obtain a similar relation between pressure and deflection as we have seen in the analytical and numerical outcomes.

Figure 71 shows the comparison of the experimental values, with the numerical, the clamped analytical and simply supported analytical outcomes for the load-deflection behavior. We obtain a similar image as for the dogbone (Figure 69), a resembling load-deflection relation, subjected to a small shift. Notice that for the circular membrane, in contrary to the dogbone membrane, we do not obtain a different pitch angle for the simply supported analytical approximation as compared to the clamped analytical approximation. Which most probably will be an artefact due to the fact that we consider only centre deflection instead of the total deflection, described on Page 69.

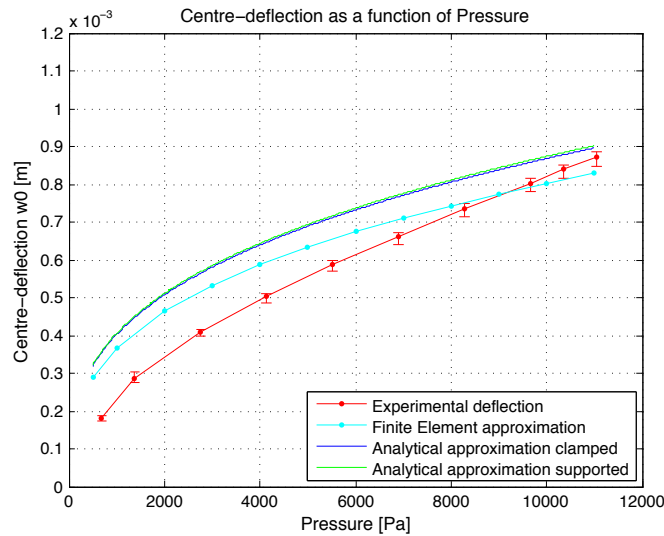


Figure 71: The experimental (red line), finite element (cyan line) and both clamped and simply supported analytical (resp. blue and green line) centre-deflections of the circular membrane as function of applied pressure, for the dogbone membrane. Notice the centre-deflection resemblance between the three methods and the experimental derived values. The simply supported analytical model resembles the experimental deflection lapse over pressure most accurately.

4.5.3 Displacement u

Figure 72 shows the experimental tracked particles in x -direction for the dogbone membrane. A polynome is used for fitting the data, containing three terms. Notice that the tracked data shows a relatively big variation. However, we do obtain a noticeable trend, indicated by the fitted polynome.

Although we obtain many tracked particles, the distribution near the edges of the membrane is very poor. When the membrane is inflated underneath the microscope, it obtains a three-dimensional shape, with an increasing depth. The pictures with particles for tracking are obviously taken in a two-dimensional manner. The microscope is not able to obtain a multiple depth focus, resulting in a picture partly focussed. The edge regions, are the regions with a sharp inclination, we thus loose focus in that region fast, when we try to obtain a large focal field. During particle tracking, the particles in these edge regions get excluded due to poor recognition of the program. Therefore, we obtain little to no tracked particles near the edge. However, we have the knowledge that the u displacement at the edge equals zero. We are thus able to extrapolate the fit towards the edge.

We do have to keep in mind that the behavior near the edge is an extrapolation, and we are not certain if any deviations from this extrapolation exist in the real membrane. We for example do not know if an exponential decrease exists near the edges as we have seen in the finite element model (Figure 47), indicating the clamped edges. The extrapolated region is indicated by the dotted line, in order to express these uncertainties.

From Figure 73 we obtain the comparison between the experimentally obtained (second sequence) and analytically approximated u displacement (supported). We obtain a very similar displacement function experimentally, as we have obtained analytically considering a simply supported two-dimensional representation, including 5 terms.

The experimental displacement u shows a shifted top towards the edge as compared to the analytical model. We have seen this slightly shifted top in the finite element u approximation, Figure 47. We can however state that the simply supported analytical model of the dogbone can very well predict the displacement u of the true dogbone membrane.

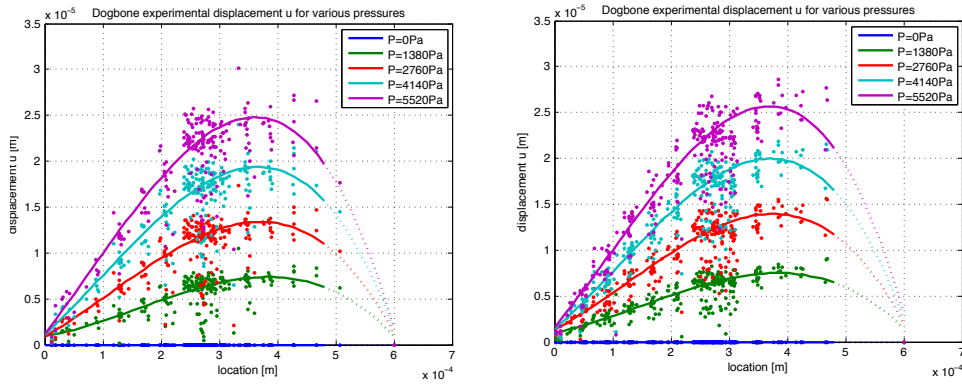


Figure 72: Experimental tracked particles for two different membranes in x -direction for the dogbone configuration. A polynome is used for fitting the data, containing three terms, including an extrapolated fit towards the edge. Notice that the tracked data shows a relatively big variation. However, we do obtain a noticeable trend, indicated by the fitted polynome.

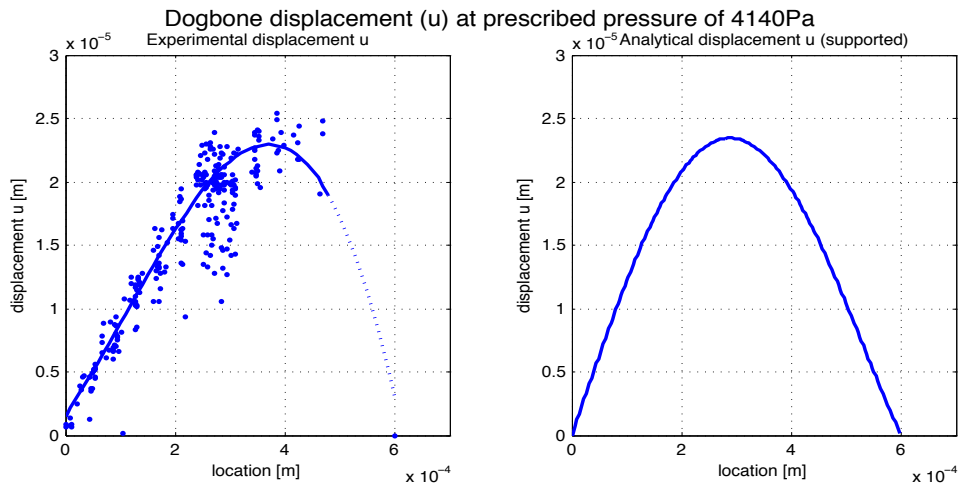


Figure 73: Experimentally obtained (left) and analytically simply supported approximated (right) u displacement. We obtain a very similar displacement function experimentally, as we have obtained analytically considering a simply supported two-dimensional representation, including 5 terms.

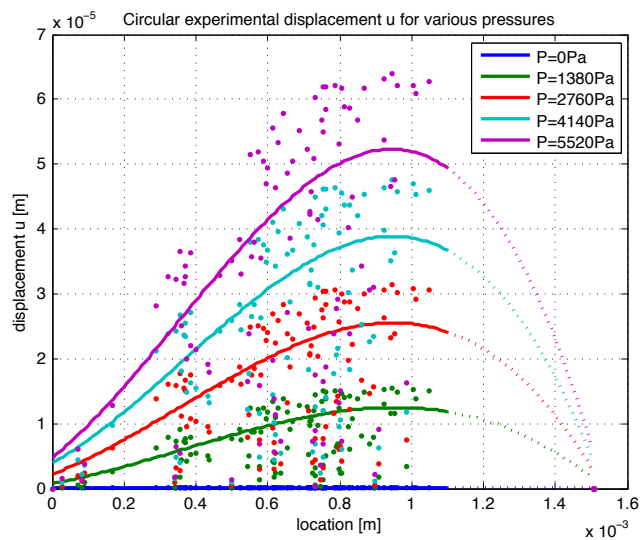


Figure 74: Experimentally tracked particles in radial direction for the circular membrane, including a fitted polynome, containing three terms. Notice that the variation in the tracked particles is even bigger for the circular membrane.

Figure 74 shows the experimental tracked particles in radial direction for the circular membrane, including a fitted polynome, containing three terms. Notice that the variation in the tracked particles is even bigger for the circular membrane. The big spread in tracked particles is due to the poor quality of the circular membrane pictures. The reflectance of the circular membrane and lighting of the microscope and camera results in pictures with a poor contrast when the membrane becomes inflated.

Furthermore, the circular membrane deflection increases even more rapidly with increasing pressure than the dogbone deflection, resulting in even a bigger challenge to obtain a sharp picture. For the circular membrane, only one sequence of pictures, and thus only one membrane could be evaluated, with the results being poor. The other two sequences of pictures resulted in little to no tracked particles.

The fitted curve (Figure 74) is obtained when first excluding data, which is in absolute sense larger than one-half the standard deviation of the initially drawn fit. Again, the dotted line represents the extrapolation of the fitted curve when including a zero displacement at the membrane's edges.

When we compare the experimentally obtained u displacement with the approximated u displacement of the simply supported analytical model (Figure 75), we obtain a resembling curve. The experimental fit shows again a slightly shifted top as compared to the analytically obtained radial displacement. Furthermore, we see a slightly large displacement predicted by the analytical model, with that keeping in mind that a lot of noise exists in the experimental data. We should however note that by no means real conclusions can be drawn from the experimental data of the circular membrane, and more study should be done on the true radial displacement of the circular membrane.

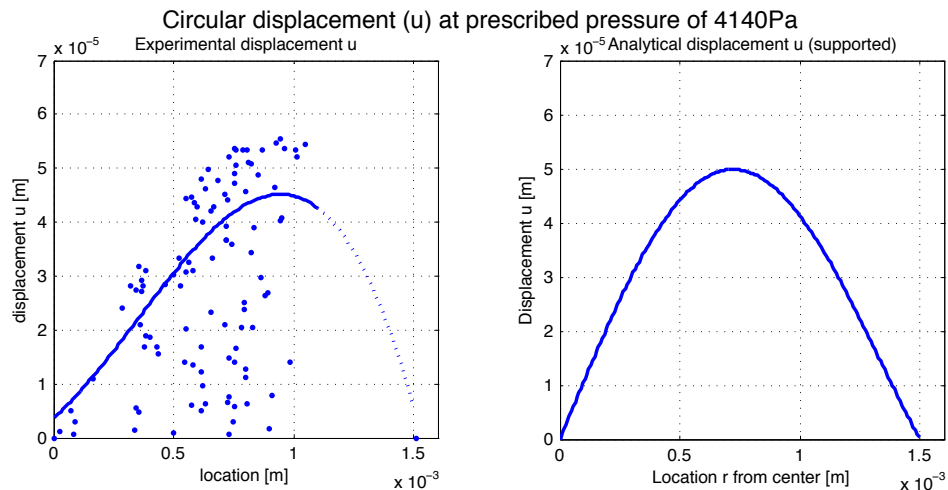


Figure 75: Experimentally obtained u displacement (left) with the approximated u displacement of the simply supported analytical model (right). Notice that we obtain a resembling curve in a resembling range. However due to the poor quality of the particle tracking (the particle spread is simply too large), no hard conclusions can be drawn from these results.

4.6 Discussion

Following this chapter, a few points of discussion should be addressed. Some discussion arises relating the experimental determination of the displacement field. Furthermore we should address the fact that during the derivation of the membrane behavior a uniform thickness membrane is considered, whereas anchoring of the cardiac muscle cells is assumed inside the grooves, where the strain can differ from the uniform membrane strain.

4.6.1 Experimental verification

The analytical approximation shows a small upward shift as compared to the experimental deflection (Figure 69), which could have several causes. The shift could be due to the fact that at processing the parameters cannot be monitored accurately. For example the young's modulus (stiffness) of the spin-coated PDMS layer cannot be determined exactly at processing. The stiffness of the PDMS layer appears to be dependent on the thickness of the layer and the way of processing. Furthermore, when using a spin-coating processing technique, most probably the stiffness of the PDMS also depends on the location on the wafer. Due to alignment of the polymer chains, the outer sections of the wafer obtain more aligned polymer chains, in contrary to the centre section where more cluttered chains are deposited [9]. A possible explanation for this shift could thus be a slightly stiffer actual membrane.

When we however adjust the young's modulus in the analytical simply supported simulation (Figure 76), we notice that mainly the pitch of the plot shifts. Which is to be expected, because we have an inverse cubic correlation between the young's modulus and the load-deflection relation.

We recall the introduction of Hooke's law for linear elastic isotropic materials (Eq. 3.27 and 3.28). Hooke's law states that extension is in direct proportion with applied load, for many soft materials however linear elastic models do not accurately describe the material behavior. These materials could be modelled with hyperelastic material models, which show a non-linear behavior between extension and applied load. It would be recommendable to try the introduction of a hyperelastic material model. A Neo-Hookean or Mooney-Rivlin material could be implemented in the applied analytical model, for accuracy purposes (Appendix 4).

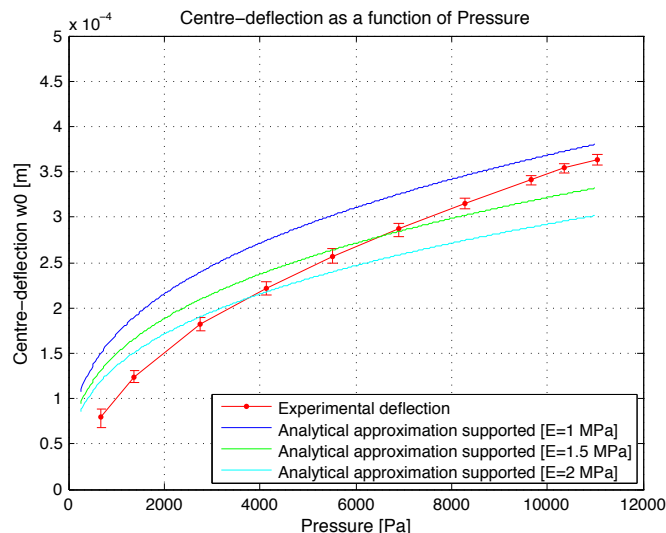


Figure 76: Experimental centre-deflection (red line), analytical approximated centre-deflection with Young's modulus equals 1MPa (blue line), analytical approximated centre-deflection with Young's modulus equals 1.5MPa (green line) and analytical approximated centre-deflection with Young's modulus equals 2MPa (cyan line) versus applied pressure. Notice that mainly the pitch of the plot shifts with increasing stiffness.

A second cause for the shift could be due to the experimental technique used. For the experiments, the centre of the membrane is visually determined. An offset from the actual centre of the membrane could result in a shifted load-deflection relation of the membrane. However, as the experiments are performed for several membranes (plotted including error bar), this shift will not be large enough to cause a shift as such. However, to exclude this factor, an experimental load-deflection study could be done with the determination of the deflection by side-view.

Furthermore, the shift could also be due to the fore mentioned definition of deflection and corresponding membrane compliancy. We make a comparison solely on the centre-deflection of the membrane. However, the actual comparison should be made according to the total deflection of the membrane. The deflection shape is dependent on many variables. We for instance model the behavior of the membrane by a distributed load, for simplification reasons. The true membrane obviously is subjected to a follower load, leading to a more globular deflected membrane. One could imagine the centre-deflection of a more globular shaped membrane to be lower than the centre-deflection of a more egg-shaped membrane. One should determine and compare the deflection by integration of the total deflection over the surface. However, to be able to do that first the total deflected shape of the membrane should be determined experimentally.

When we consider the displacement u , determined experimentally, we have seen some major difficulties, leading to experimental results from which no hard conclusions can be drawn. For a better tracking of the particles several sequences of pictures could be made, taking a different focal area per sequence in order to obtain more tracked particles. When more particles are tracked a trend will probably become more apparent, and the edge effects will probably also become visible.

4.6.2 Groove strain

Another point of discussion is that the strain in the grooves is of main concern, while we so far have only determined the overall (leading) membrane strain. The strain in the grooves however directly affects the cell stretch, when assuming anchoring of the cells inside the grooves. As can be witnessed from Figure 77, this strain is not equal to the leading membrane strain. For simplification reasons the calculation of the axial strain inside the grooves here is done with use of the finite element model (Appendix 1).

We have seen that the axial strain of a thin membrane is almost solely due to the stretch of the membrane, when considering a pressure of approximately 3 kPa per unit area or more. To calculate the transverse strain inside a groove we consider one building block of the membrane. The leading membrane strain taken is 0.25, which follows if we take a prescribed displacement of the right side of the building block of 10 microns. The left side is taken to be a symmetry axis.

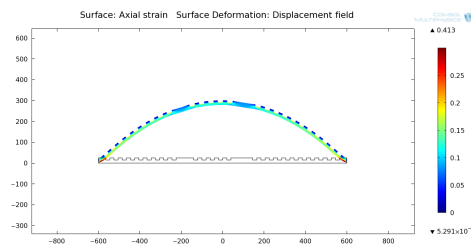


Figure 77: Image of the axial strain in the dogbone membrane as approximated numerically. Notice that the strain inside the grooves does not equal to the leading membrane strain.

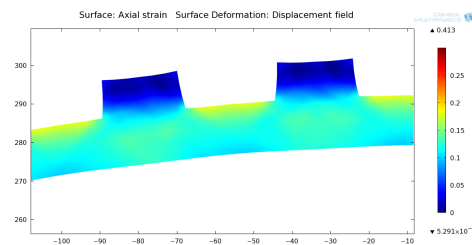


Figure 78: Close-up of Figure 77. Notice that the bulk material blocks on top of the membrane constrict the top part of the membrane underneath these blocks, resulting in a higher strain inside the grooves.

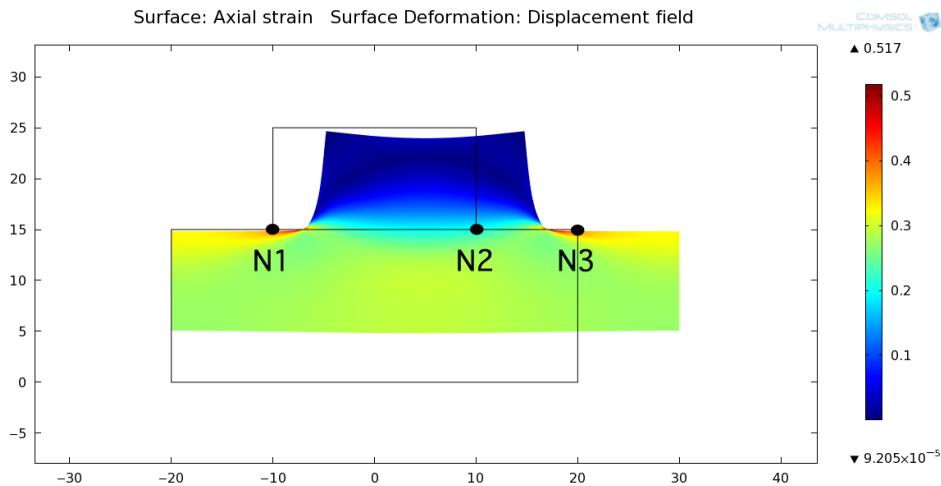


Figure 79: Single element of the dogbone membrane, strain differences can be calculated from the nodal displacements.

The bulk material blocks on top of the membrane constrict the top part of the membrane underneath these blocks. However, the total displacement of this slice of material has to be equal to the displacement of the rest of the membrane, for continuity reasons. Therefore the material between these constricted parts, have to take up the extra strain the block constricts. The effect of the bulk material on top of the membrane, on the strain inside the grooves, is determined by the nodal displacement of the three corner points (N1, N2 and N3 in Figure 79). The nodal displacement of the three points is show in Table 1.

Table 1: Nodal displacement of one element of the dogbone membrane, when the right boundary is subjected to an displacement of 10μm.			
	Node 1	Node 2	Node 3
Nodal Displacement	3.1 μm	6.9 μm	10 μm

The relation between the leading membrane strain and the strain inside the grooves (the attachment area for the cardiomyocytes), can be defined as:

$$\epsilon_a(groove) = \frac{\left(\frac{Lo}{2} + \Delta L * \frac{6.2}{10}\right) - \frac{Lo}{2}}{\frac{Lo}{2}} \quad 4.57$$

$$\epsilon_a(groove) = \frac{31}{25} \epsilon_a = 1.24 \epsilon_a \quad 4.58$$

This modifies the pressure-strain relation to the relation shown in Figure 80.

¹ Prescribed displacement

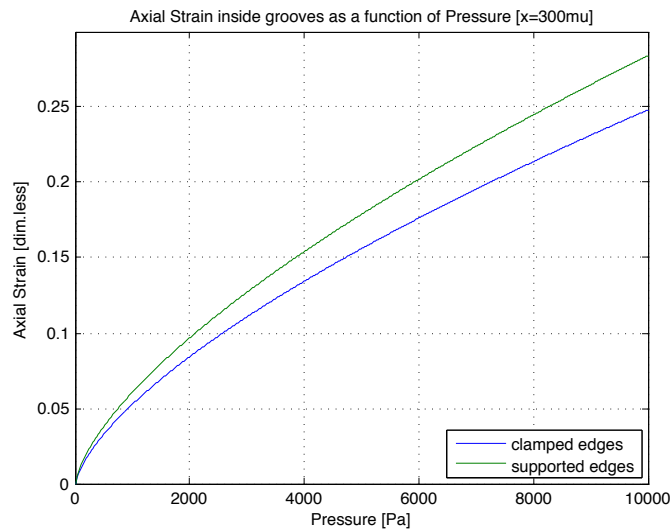


Figure 80: Modified load-strain relation. This graph shows the strain inside the grooves. Notice that the analytical approximation gives resembling values with the Finite Element approximation.

Notice that this analytical approximation gives resembling values with the Finite Element approximation. The analytical simply supported approximation gives a strain inside the groove at an applied pressure of 5 kPa of approximately 0.175 versus the strain given by the Finite Element approximation of approximately 0.18. We choose to describe the behavior of the membrane by the simply supported analytical model, for the reason that its results show the highest similarity with both the finite element model and the experimental values.

We assume here that the ratio groove strain over leading membrane strain versus pressure behaves linearly. For a more accurate definition of the groove strain with respect to the overall membrane strain, one could use a weight method. Determining the constricting role of the block material on top of the membrane by their relative weight.

The same is done for the transverse strain in the circular membrane, as we can see (and imagine) that for the transverse strain in the circular membrane a similar effect occurs (Figure 81). The effect however is not as big as for the axial strain in the dogbone, which also became apparent from the established uniform representation (Appendix 3). The multi-axial strain that exists in the circular membrane and the round constriction leads to this lower effect of the grooves. The deflection of the membrane depends on the extension in two directions, the transverse direction and the radial direction.

At the edges the transverse strain equals zero, because of the rigid connection. The material in between the grooves will therefore not get pulled apart as fierce as in the dogbone membrane where the axial strain is barely constricted.

For the strain in radial direction (Figure 82), the material in between the grooves acts as ribs, adding extra stiffness to the structure. Because the orientation of these ribs is in the direction of the strain considered, the cutouts will barely affect the membrane motion in this direction, as we can see from Figure 82.

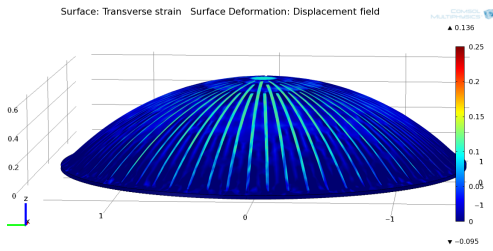


Figure 81: Transverse strain of the circular membrane. Notice that for the transverse strain in the circular membrane a similar effect occurs as for the axial strain in the dogbone membrane. Bulk material on top constricts the strain of the membrane.

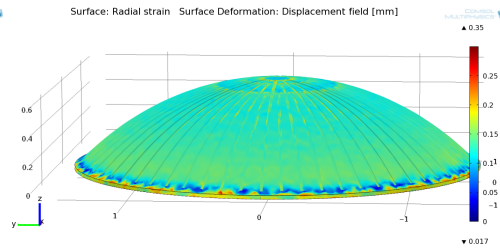


Figure 82: Strain in radial direction of the circular membrane. Notice that no constricting effect occurs in radial direction.

The overall membrane strain in radial direction thus equals the membrane strain inside the grooves. We can thus obtain the radial strain directly from Figure 61, where the radial strain is presented for the analytical simply supported membrane. The highest strain value is considered, as we want to prevent overstretching of the cardiac muscle cells. Figure 83 shows this ceiling value of radial strain and the modified transverse strain. From nodal displacement in the finite element model, the factor relating the overall membrane strain to the groove strain appeared to be 1.16:

$$\epsilon_i(\text{groove}) = 1.16\epsilon_i \tag{4.59}$$

From Figure 83 we obtain the strain inside the grooves that the cardiac muscle cells will be subjected to (assuming anchoring inside the grooves, cross-ref paragraaf in intro), as function of the applied pressure.

Notice that when considering pure strain inside the grooves, that the transverse strain resembles the radial strain in a better manner. However, we should take into account that the transverse strain still varies largely over the membrane. The radial strain thus resembles the maximal transverse strain, near the centre of the membrane. The cells on the outer regions of the membrane will not receive an equal strain in transverse and longitudinal direction. They will be subjected to a larger strain in the longitudinal direction as compared to the transverse direction.

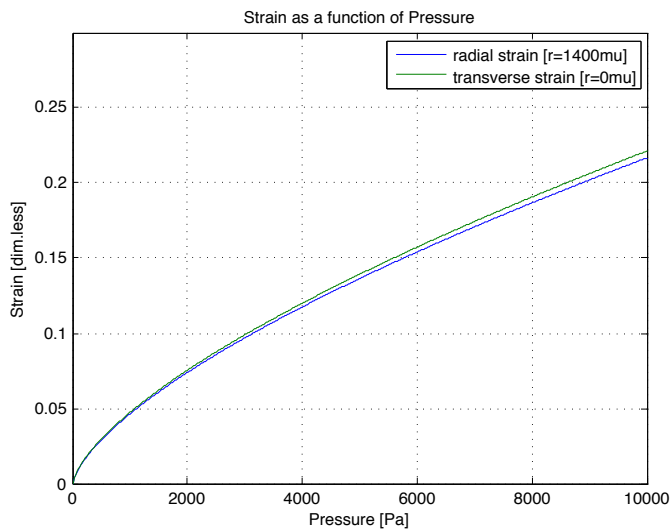


Figure 83: Radial (blue line) and transverse (green line) strain inside the grooves of the circular membrane as function of applied pressure. Notice that when considering pure strain inside the grooves, that the maximum transverse strain resembles the radial strain.

4.7 Conclusions

From the outcomes of the analytical model with various boundary conditions (Figure 45, Figure 46 and Figure 48 in Section 4.4.1) in comparison with the results of the numerical model (Figure 42 and Figure 47 in Section 4.4.1) and the experimental data (Figure 43 in Section 4.4.1, Figure 69 in Section 4.5.2 and Figure 72 and Figure 73 in Section 4.5.3), we are able to conclude that a simply supported analytical model, considering a two-dimensional, $16.5\mu\text{m}$ thickness representation properly describes the dogbone membrane behavior. For this model we assume a linear elastic homogeneous isotropic material, from which we have seen that the error with the experimentally determined values remains small. The determination of the membrane behavior by means of a potential energy method has shown to provide correct outcomes. However, the right trial function, and boundary conditions are essential. Both the in plane displacement u and the deflection play a big role in the accuracy of the analytical outcome. The trial in plane displacement function shows to have a big effect on the strain outcomes.

Furthermore, for an increased accuracy in the description of the edge effects in this potential energy also the shear deformations due to transverse forces could be implemented. For this application there is no necessity of including these deformations. We assume that the cardiac muscle cells attach inside the grooves, the shear deformation occurs only in the small region near the edges where the actual membrane leaves under a zero tangent. When including these shear deformations, one should also apply the formulation of clamped boundaries, as they introduce the effect.

Similarly, from the outcomes of the analytical model with various boundary conditions (Figure 54, Figure 55, Figure 57 and Figure 59 in Section 4.4.2) in comparison with the results of the numerical model (Figure 56, Figure 58 and Figure 60 in Section 4.4.2) and the experimental data (Figure 52 in Section 4.4.2, Figure 71 in Section 4.5.2 and Figure 74 and Figure 75 in Section 4.5.3), a three-dimensional, round the edges supported analytical model, properly describes the behavior of the circular membrane. Here we consider a $21.5\mu\text{m}$ thickness representation, assuming a linear elastic homogeneous isotropic material.

We can state that the membrane behavior of both membrane configurations depends mainly on the extensional energy density. When lower ($<3\text{kPa}$) pressure is applied, extensional and bending strain energy determines the membrane's behavior. However, when applying larger amounts of pressure, the bending strain energy fails to participate in the membrane's behavior. This is due to the fact that the membrane has a very small thickness to area ratio, and the deflection is very large.

In the dogbone membrane, the axial strain (transverse on the cardiomyocytes) shows a nice homogeneous distribution. This will result in a similarity in transverse stretch of all the cells situated on the membrane. The cells are considered fully anchored, and plated in a monolayer. The radial strain, introducing a longitudinal stretch of the cells, of the circular membrane is also nicely homogenous distributed. However, the transverse strain (Figure 84) increases towards the centre of the circular membrane. The transverse strain (on the bottom of the grooves) in the centre of the membrane resembles the radial strain. This will result in equally stretched cardiomyocytes longitudinally and transversally in the central region of the membrane. However, the cardiomyocytes in the outer regions of the membrane will barely receive transverse stretch, although their longitudinal stretch will be equal to the centrally plated cells.

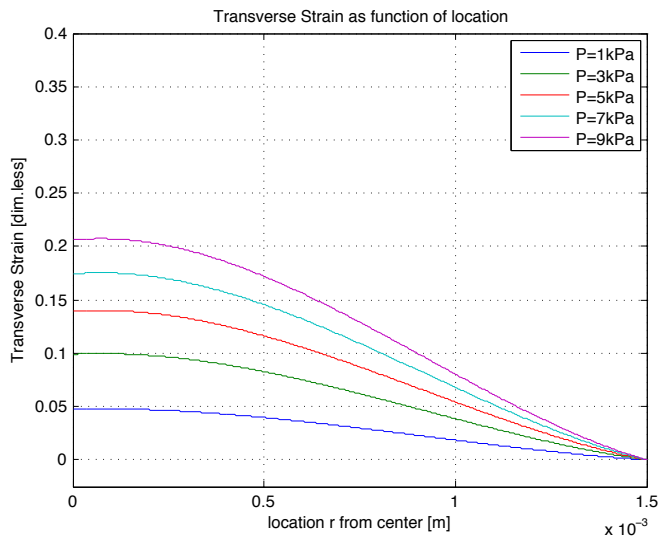


Figure 84: Transverse strain inside the grooves of the circular membrane. Notice that the transverse strain is not uniform for the entire membrane, a strain gradient exists along the radial coordinate.

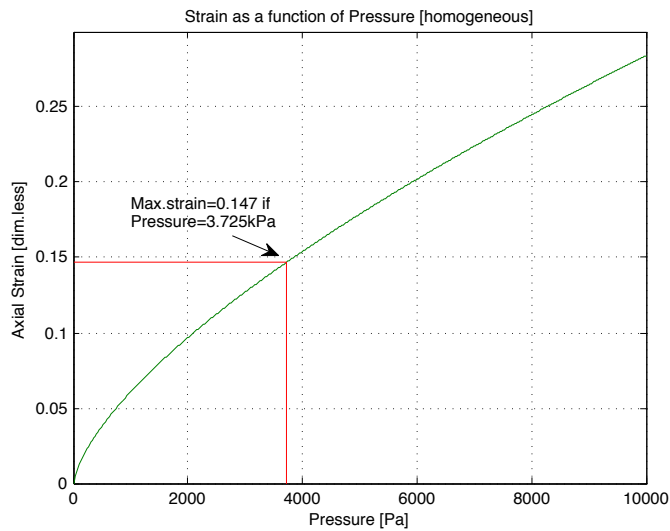


Figure 85: Axial strain as function of pressure for the dogbone membrane. A pressure of 3.735kPa should be applied in order to obtain a strain of 14.7% on the cardiomyocytes.

From Figure 85 we observe that when we consider the dogbone membrane, we will need to apply 3.725kPa to obtain the desired amount of strain of 14.7% on the cardiomyocytes situated in the grooves of the membrane (Section 2.4).

Figure 86 however shows that for the circular membrane, to obtain the same desired amount of strain of 14.7%, we should apply a much higher amount of pressure. To obtain the same stretch of the cells on the circular membrane as the cells on the dogbone membrane, a pressure of 5.375kPa should be applied.

Whereas both membranes are produced for simultaneous stretching, in order to see the difference between multi-axial loading and uni-axial loading under equal conditions, we notice that cells in that case on one or the other membrane do not obtain the right amount of strain.

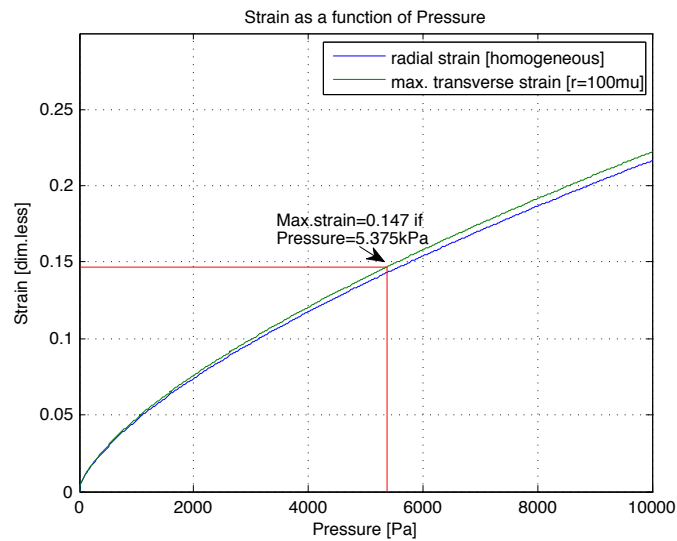


Figure 86: Radial (blue line) and transverse (green line) strain as function of pressure for the circular membrane. A pressure of maximum 5.375 kPa should be applied in order to obtain a maximal strain of 14.7% on the cardiomyocytes.

We thus conclude that the pressure protocol should depend on the membrane configuration implemented in the experiment. Furthermore, when we consider the ventricular volume – time relationship, presented in Figure 87, ideally the pressure protocol should match this particular course. In Figure 87 the red line represents the volume of the left ventricle over time. The time-span is not mentioned in this figure, as it depends on the heart frequency. When we consider a relatively standard human adult heart frequency in rest of 1 Hz (60 beats per minute), we can conclude that approximately two-third of the time-span of one second per heartbeat the heart is filling, and one-third of the time the heart is ejecting.

Moreover, both filling and ejection phase show an exponential upstroke function and an exponential down stroke function. Widely stated, the left ventricle volume shows a blunted block-function over time. For preliminary testing implementation of a block-function including some build-in delay will approach the *in vivo* left ventricle volume over time relation. For experiments including dogbone membranes a block-function with an absolute peak pressure of no more than 3.725 kPa should be introduced, whereas for experiments including circular membranes a block-function with an absolute peak pressure of no more than 5.375 kPa should be introduced.

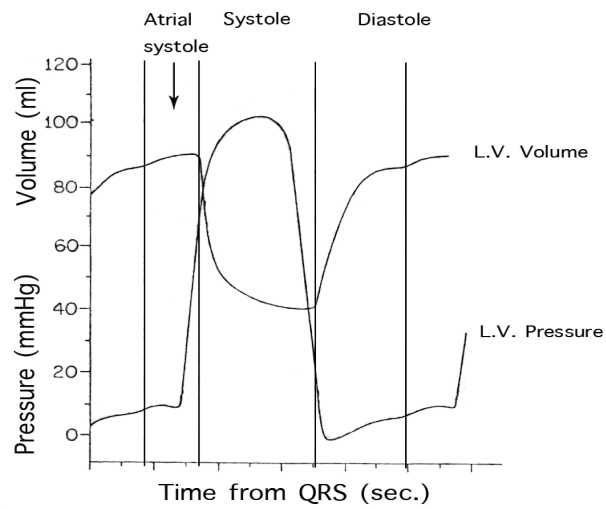


Figure 87: Left ventricle behavior, the red line denotes the left ventricular volume. Notice that that approximately two-third of the time-span of one second per heartbeat the heart is filling, and one-third of the time the heart is ejecting. We can model this left ventricular volume behavior by a blunted block-function over time, related to the heart frequency.

PART IV : PRELIMINARY EXPERIMENTS

5 Preliminary Experiments

In this chapter some preliminary results regarding stretched cardiomyocytes will be discussed. Because of the preliminary nature of these experiments, and a poorly optimized process, we are not able to draw any hard conclusions from the results regarding the developed loading protocol. These preliminary experiments are done in terms of verification of the principle of stretching anchored cardiomyocytes in vitro by inflation of the substrate.

Materials and methods of testing are described in Section 5.1. In Section 5.2 some preliminary results are presented. Section 5.3 shows some discussion points considering the experimental methods and the results, and finally in Section 5.4 the conclusions considering the outcomes of the preliminary experiments are discussed.

5.1 Materials and Methods

5.1.1 Construct preparation

Primarily the Cytostretch chips were plasma treated by electric glow discharge to ensure a hydrophilic membrane surface, for easy fluid access. The chips were subsequently coated with a 20% fibronectin solution (40 μ l fibronectin, 160 μ l DPBS-) and incubated for at least one hour.

Human embryonic stem cells were cultured under standard conditions (with feeders to support renewal). Subsequently the scaled up hES cells were cocultured with endoderm-2 cells to extensively induce differentiation into cardiomyocytes. The cocultures were incubated at 37 degrees celcius and at a 5% CO₂ concentration. Beating areas on at least 12-day cocultures were selected and dissociated by cutting[55], whereupon the beating areas were dissected in plane in order to obtain beating lumps with little thickness. The beating lumps were plated on the fibronectin-coated chips (washed by DPBS-) including BPEL cell medium for nutrition.

The chips were incubated without stretching for 48 hours minimum in order to obtain cardiomyocyte anchorage on the PDMS membrane.

5.1.2 Experimental setup

After 48 hours of incubation, the chips were positioned in the stretch setup. The stretch setup consists of a chip-holder, developed for 6 chips (Figure 88). Due to the big tolerance on the chips, the holder is designed to clamp the chips between two metal blocks (Figure 89). This ensures that any chip can fit into the chip-holder. Due to the fact that the medium fluid container is small, it was decided to use an under pressure (creating vacuum) in order to create more rather volume in this container. Because we have seen that up from approximately 3kPa the bending term does not contribute to the total strain energy of the membrane, we can state that an applied over pressure will result in the same membrane strain as an equally applied under pressure. Furthermore, under pressure will pull the chip downwards onto the lower part of the chip-holder, combined with rubber o-rings the under pressure will make the airflow up to the membrane airtight (Figure 89). Two holes are created halfway in plane in the lower section of the chip-holder, leading to the holes underneath the chips inside the o-rings, for the passing of air. At the other end from the entering of the holes, a hole is created perpendicular to the first two holes, connecting the first to and enabling a linkage to a pressure sensor for measuring the actual pressure underneath the membranes.

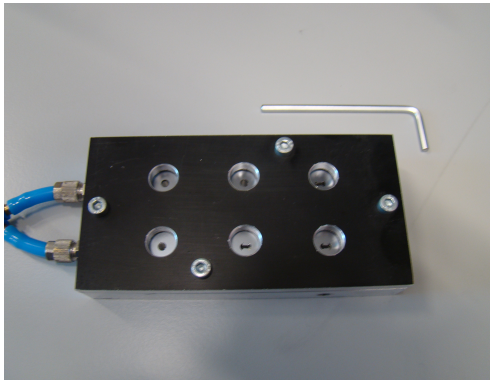


Figure 88: Chip-holder, developed for 6 chips. The holder is designed to clamp the chips between two metal blocks, to ensure that any chip fits in the holder. The two metal parts are joined together with hexagon socket head screws.

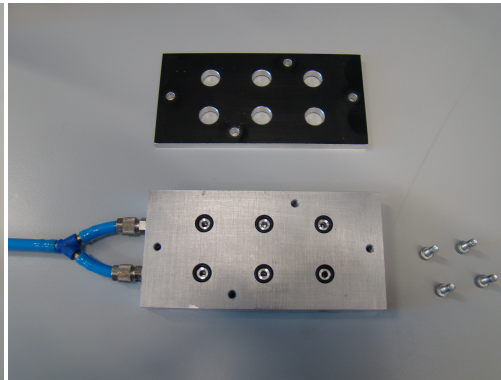


Figure 89: Chip-holder opened up. The o-rings ensure an airtight fit. Furthermore, the screws are not centrally aligned in order to reduce pressure on the outer chips.

The upper part of the chip-holder will ensure a tight fix, and will keep the chips in place. This upper part contains slightly larger holes to accommodate for the medium fluid containers. The holes surround the fluid containers exactly for a nice alignment of the chips with the suction holes. The upper half of the chip-holder is attached to the lower half by 4 hexagon socket head screws (Figure 88). The central two, are not exactly centrally aligned in order to reduce pressure on the silicon parts of the outer chips. For the experiments the hexagon socket head screws were cautiously fixed in order not to pulverize the silicon chips. The entire chip-holder is placed in the incubator for experiments (Figure 95).

The two air holes are lead to one tube, which can be disconnected just behind the y-splitting, in order to easily remove the chip-holder from the incubator. The air tube runs through a hole in the backside of the incubator towards the mechanical part of the experimental setup situated on top of the incubator. The air tube runs towards a solenoid valve (Figure 90), an electromechanical valve suitable for liquid or gas. A solenoid valve is a induction valve, which operates by means of a magnet and a coil. An electric current in the coil creates a magnetic field, which draws a piston up inside the coil, pulling with it a diaphragm that normally closes off the airflow. The lift of the diaphragm mechanically opens the valve. Solenoid valves offer fast switching, a long service life, a low control power and a compact design, useful for this application. The solenoid valve runs on 24 Volt.

Airflow towards the solenoid valve is controlled by a manual regulated analogue flow-regulator (Figure 91). With this regulator the airflow from the valve towards a vacuum chamber can be regulated, in order to obtain the correct negative peak pressure just before the valve closes. This means that when we introduce a higher heart-frequency, the regulator should be further opened in order to obtain the same negative peak pressure. As mentioned, the flow regulator is linked to a vacuum chamber (Figure 92). This chamber is implemented in order to maintain a constant pressure. Simple pumps do not have the possibility to ensure a steady pressure. However, when introducing a vacuum chamber between the pump and the valve, we introduce a pressure buffer. The vacuum chamber is obviously connected to a pump (aquarium pump, Figure 92), which creates a vacuum inside the vacuum chamber. The pump operates on normal line current.

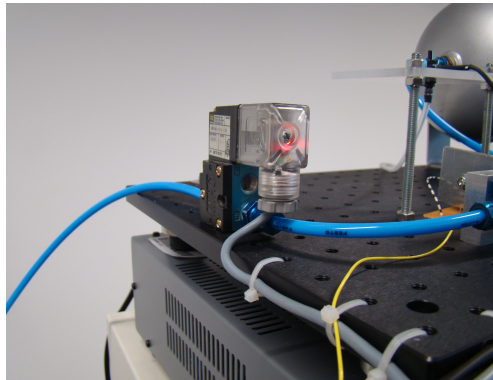


Figure 90: Solenoid valve, controlled by the Labview program. The solenoid valve opens and closes corresponding to a heart frequency of 1Hz.



Figure 91: Manual analogue flow regulator (centrally situated in the image, blue box with grey turning wheel). The flow regulator is adjusted until the right absolute peak pressure is obtained (read out on computer screen).

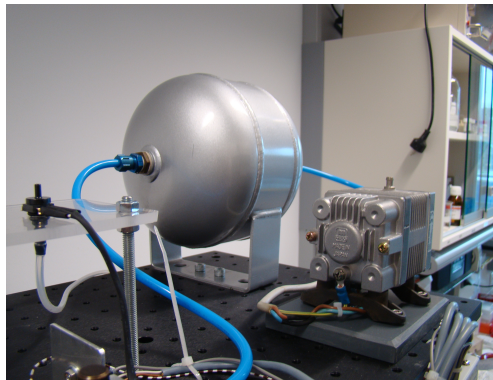


Figure 92: Sensor for pressure readout (left), vacuum chamber for maintenance of a constant pressure (centre) and the aquarium pump for creating the vacuum (right).

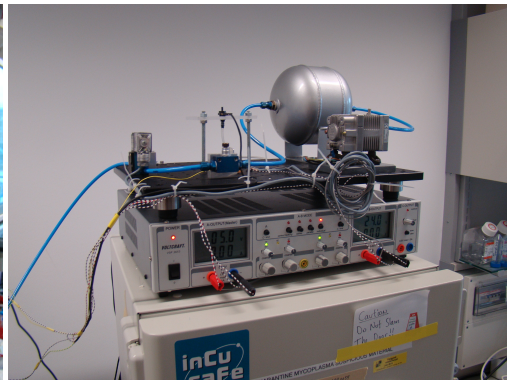


Figure 93: The entire mechanics of the experimental setup, including power supply.

The solenoid valve is controlled via a data acquisition system. The digital port of the DAQ is used to control the solenoid valve. However, as the digital port of the DAQ only generates 8.5mA of current, a Darlington transistor (TIP132) is used to amplify the signal from the DAQ towards the solenoid valve. A Darlington transistor circuit is a compound transistor circuit, which consists of two transistors in which the collectors are tied together and the emitter of the first or input transistor is directly coupled to the base of the second or output transistor. The Darlington amplifies the signal twice, creating a DC (direct current) current gain of typically 500 to 15000, creating enough current to operate the solenoid valve[56].

The analogue port of the DAQ is connected to an integrated silicon pressure sensor (MPXV4006C6T1, Figure 94). This sensor operates on 5V, and is able to measure pressures between 0 and 6kPa. The sensor measures relative pressures, therefore reversed implementation will result in the measurement of negative pressures up to 6kPa. The choice for this sensor (0-6kPa) has been made due to its great accuracy. For later disease modelling, other sensors are present, which can be directly integrated. The total electrical scheme is presented in Appendix 5.

The data acquisition system (DAQ) is connected to a windows computer (Figure 95), for sensor readout and valve control in Labview. A block function is introduced in the Labview program, controlling the solenoid valve. Chosen is to use a block function in order to maintain a tempered valve control. Furthermore, due to the delay in the valve and tubes running to the chip-holder the block function will smoothen, and a function corresponding to the left ventricle volume-time relation will originate (Figure 96). The Labview program is programmed to save three cycles every half to three hours (time-span can be adjusted in the program). Moreover, the program constantly shows the introduced heart-rhythm, 1 hertz

(60 times per minute), and the absolute pressure-difference over the membranes. The pressure difference is calculated from the typical offset of the sensor (0.265 V) and the sensitivity (0,766 V/kPa) (Appendix 6)[57].

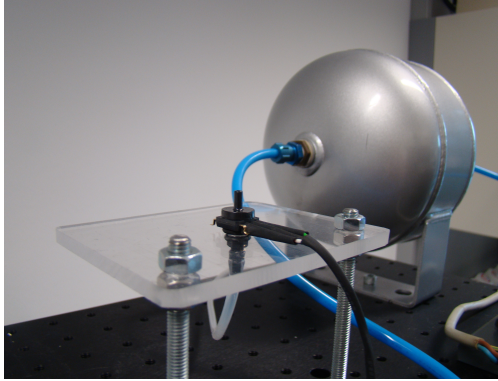


Figure 94: Foreground: pressure sensor, connected to the air holes underneath the chips, for an accurate pressure readout.



Figure 95: The entire experimental setup. The chip-holder is placed in the incubator situated underneath the experimental setup's mechanical part. Control and readout is done by means of a laptop with Labview.

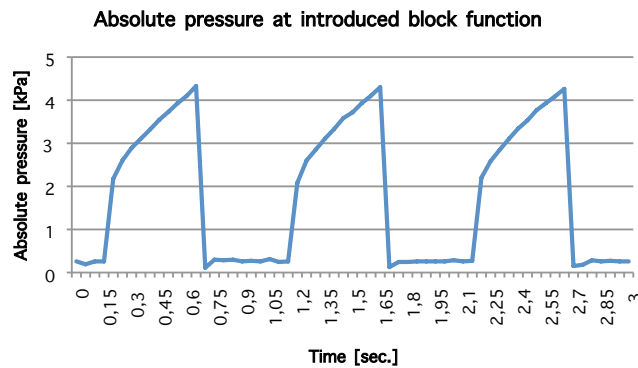


Figure 96: Sensor readout. Notice that the introduced block function gets blunted in the upstroke, however when the valve is opened, the pressure drops back to atmospheric pressure immediately.

5.2 Results

5.2.1 First set of experiments

The first experiment was set up solely out of circular membranes, to which a negative pressure of approximately 5.3 kPa was applied. This experiment was performed over a time span of 5 days, subsequent to 3 days of anchoring in the incubator without loading.

After 5 days the first experiment failed due to a lack in fluids. When cells are plated in a normal well plate they incubate in large amounts of nutritious medium. The Cytostretch chips, however, contain a small medium container, surrounding the membrane. The volume of this container is as such, that the fluid condenses out of the container too fast. To obtain a reasonable fluid level, extra units with fluid were placed in between the chips, on top of the chip-holder for extra humidity. This however did not solve the problem of condensation of the medium. Together with a non-tight fit of the applied lid, the fluid condensed too fast, and left a highly concentrated (minerals) fluid on the cells, leading to cell death. Although the first experiment did not lead to any results concerning maturation enhancement, it was considered a prosperous experiment. The cells did not appear to be agitated by the movement of the substrate and remained attached during the entire 5 days of testing. Furthermore, the sensor obtained a steady pressure curve during the experiment, indicating a correct function of the experimental setup (Figure 97-Figure 100).

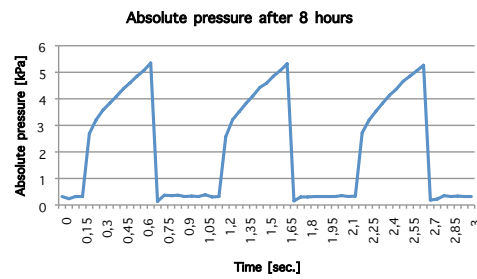


Figure 97: Sensor readout of three cycles after 8 hours.

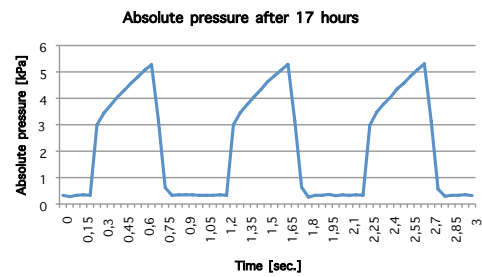


Figure 98: Sensor readout of three cycles after 17 hours. Notice that the peak pressure maintains a constant value.

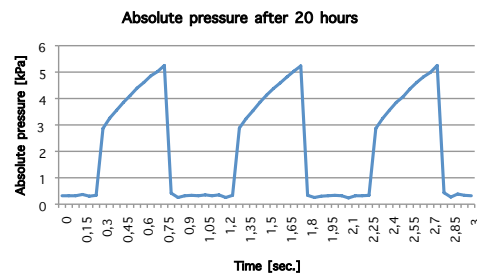


Figure 99: Sensor readout of three cycles after 20 hours. Notice that the peak pressure maintains a constant value.

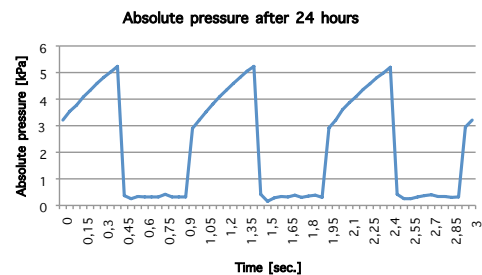


Figure 100: Sensor readout of three cycles after 24 hours. Notice that the peak pressure maintains a constant value. Furthermore, notice that somewhere along the experiment the block function got shifted.

Notice the small shift of the graph in Figure 100, which is related to sudden irregularities in the control of the solenoid valve. The pressure diagram occasionally shows an irregularity, as can be witnessed in Figure 101. A shortened block diagram is introduced to the solenoid valve, resulting in some kind of heart fluttering for the cardiac myocytes. This will however have little to no effect on the cardiac myocytes, as these irregularities also occur in a healthy heart. Furthermore, we witness an offset. Zero pressure, thus atmospheric pressure, is set from the sensor offset (when the valve is closed). We can however see from Figure 97 to Figure 100 the sensor does not have this typical offset in pressure differential; it appears to be slightly higher.

5.2.2 Second set of experiments

Due to the inconvenience of removal of the entire tube through the hole in the back of the incubator, before the second set of tests a link was created near to the y-junction (near the chip-holder). From the initial pressure diagram (Figure 102) it became evident that there was leakage around this link. The absolute peak pressure was a lot lower and a big pressure loss occurred when the valve was open. For the realization of an airtight link, parafilm was wrapped around the link. Furthermore, the flow regulator was adjusted to obtain the right amount of pressure underneath the membrane (approx. 3.7 kPa due to the implementation of the dogbone membranes). Apparently however, some air leakage still occurred. The parafilm slowly sealed the leakage, creating eventually an airtight fit. This resulted in a slow increase in negative pressure underneath the membranes (Figure 103).

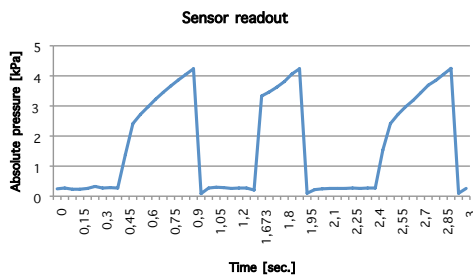


Figure 101: Irregularity in the pressure diagram. A shortened block diagram is introduced to the solenoid valve. Labview occasionally shows these irregularities in outgoing signals.

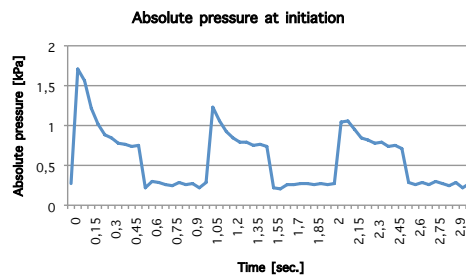


Figure 102: Initial pressure diagram in the second set of experiments. Notice that the chip-holder cannot keep the pressure, indicating an air leakage.

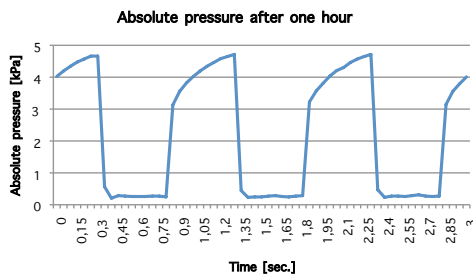


Figure 103: Sensor readout after one hour. Notice that the pressure has risen drastically, indicating slow closure of the leakage.

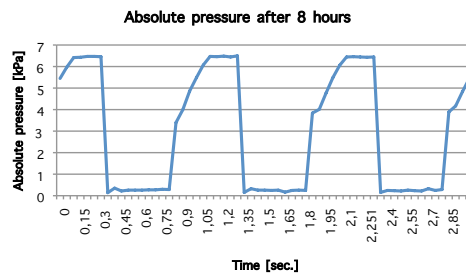


Figure 104: Sensor readout after 8 hours. Notice the further increased pressure up to the ceiling value measurable by the sensor. Moreover, notice that the ceiling value is slightly higher than expected ($>6kPa$). This is due to the slightly higher offset than typical for this sensor. Furthermore, the operating voltage could have been slightly higher than 5Volt.

After 8 hours, the pressure reached the maximum measuring value of the sensor (Figure 104). The pressure increased up to an approximate maximum pressure of $7kPa$. The cardiac myocytes reacted negative to the increased pressure protocol; all beating areas detached. The cardiac myocytes however did remain alive. Subsequently the measurement setup was turned of, to provide an opportunity for the beating areas to reattach.

The second set of tests also revealed a major problem with the experimental setup. Considering the humidity and oxygen rich airflow in the incubator, aluminium is used as material for the chip-holder, a relatively oxidation stable material. However, due to contact with other materials, oxidation did occur (Figure 105 and Figure 106). Oxidation particles travelling through the incubator destroyed the cells.



Figure 105: Bottom view of the chip-holder, the contact with another metal in the incubator initiated corrosion.

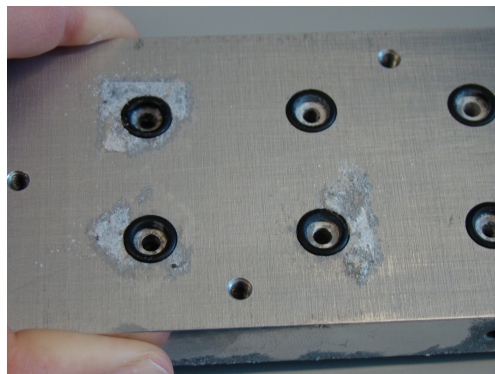


Figure 106: Top view of the bottom part of the chip holder. The corrosion has also immigrated towards the upper side of the chip holder, near the chips. Oxidation particles floating through the air are able to destroy the cardiomyocytes.

5.3 Discussion

Following the preliminary experiments, a few points of discussion should be considered. Primarily we should address the fact that initially a block function is introduced into the solenoid valve. Although the block function smoothens due to delay in the opening valve in the concaving motion of the membrane, the closing of the valve, and introducing atmospheric pressure at the membrane occurs very suddenly. This introduces a fast snap back to atmospheric pressure at valve closing (Figure 96). We have however concluded that the true left-ventricle volume-time function shows both an exponential behavior during the filling stage as well as during the contraction stage. The introduced block function is thus not able to properly describe ejection of the left ventricle.

Furthermore, due to atrial systole, the filling stage consists of two subsequent exponential functions. Primarily, a filling phase due to under pressure that originates in the left ventricle subsequent to ejection, and secondly an additional filling phase due to the ejection of blood from the left atrium into the ventricle.

Moreover, the filling phase takes up approximately twice the amount of time with respect to the ejection phase. For a proper introduction of the left ventricular behavior to the *in vitro* cultured cardiomyocytes, we should approach the correct volume-time relation. This means that longer phases of vacuum (stretching) should be implemented, with respect to zero pressure phases. The solenoid valve will not be able to switch frequently enough to realise a solid exponential increase in the two phases, following a smooth exponential decrease in pressure. A solution in realising the exact left-ventricular volume behavior, is the substitution of the solenoid valve by a flow-regulator, controlled by the Labview program. Furthermore, a feedback loop could be introduced, measuring the true pressure-differential value over the membrane (sensor), comparing this value with the introduced pressure, and creating a feedback to the flow-regulator.

When we review the pressure curves obtained from the first experiments (Figure 97-Figure 100), it is indicated that the typical offset of the sensor does not agree with the actual offset of the sensor. The result is that when we tune the manual analogue flow-regulator to the correct absolute peak pressure, the pressure difference between the stretched membrane, and the relaxed membrane is slightly smaller than initially meant. For an easy tuning of the absolute peak pressure the offset should be tuned to obtain a zero value at zero difference between the outside pressure and the pressure underneath the membrane. Furthermore, the supply voltage should be exactly 5 *Volt*.

The sensor measures the pressure differential between the outside air (atmospheric pressure), and the pressure underneath the membrane. We actually are interested to know the pressure differential over the membrane. On top of the membrane fluid is situated, leading to an increased pressure on top of the membrane. When we calculate the additional pressure this fluid puts on the membrane, we are able to see that it is negligible compared to atmospheric pressure existing at sea level (approx. $100kPa$).

Specifications:

Water density:	1 g/cm ³
Container radius:	0.5 cm
Container height:	0.5 cm

Calculations:

$$V = \pi r^2 h = 0.3927 \text{ cm}^3 \quad 5.1$$

$$A = \pi r^2 = 0.7854 \text{ cm}^2 \quad 5.2$$

$$P_{\text{column}} = \frac{\text{Mass}}{\text{Area}} = 50 \text{ Pa} (N / m^3) = 0.05 \text{ kPa} \quad 5.3$$

To recover an airtight valve - chip-holder connection, the introduced link has been replaced by a more rigid connection. The earlier connection contained a connection by sliding the tube over a ridged end, and realising fixation by a screwed on cap. The other side of the connection contained a little metal tube with an inner o-ring, the pressure tube was positioned inside the metal tube, with the o-ring realising an airtight connection. This connection will possibly remain airtight when an overpressure is introduced, pressing the pressure tube against the o-ring. However, when a negative pressure is introduced, the pressure tube will become slightly smaller in diameter, resulting in an air leakage at the o-ring. The new introduced linkage consists of double ridged-end connection, resulting in an airtight link able to be disconnected.

For the first set of experiments, the cardiomyocytes were plated on the Cytostretch chips in lumps. Entire beating areas were cut from the primary substrate, and plated as whole on the membranes. Each membrane subsequently contained one contracting outgrowth. Resulting this plating method were contracting outgrowths, which only attached to the membrane by a small lower section. The strain of the membrane will only be taken up by this lower section of the contracting outgrowth. Although we assume that the cardiomyocytes in a contracting outgrowth communicate, it is not likely that the stretching of connecting cells will affect the maturation of the non-stretched cells. In order to broaden the contact plane of the contraction outgrowth with the membrane, in the second set of experiments the cells were split to obtain flat beating areas. However, still cells maintain to be out of reach for the membrane to transfer strain. For a proper experiment execution, the cells should be situated on the membrane in a monolayer. This monolayer can be obtained by plating after trypsinization; cutting the beating areas into a single cell solution with use of trypsin, a dissociation enzyme present in the digestive tract. Consequences could however be decreased cell viability.

5.4 Conclusions

The conclusion regarding the preliminary experiments have been split up in conclusion regarding the experimental setup and conclusion regarding the results considering the effect on the cardiac myocytes.

5.4.1 Experimental setup

We have witnessed that the incubator environment accommodates for oxidation processes. The humidity and various metal components present commences oxidation processes even with metals, which are, relatively oxidation stable. We are thus able to conclude that non-metal experimental setup components should be used for placement inside the incubator.

Furthermore, the low medium container of the Cytostretch chip introduces problems considering the cells humidity and mineral concentration. A suitable lid appears to be essential for the maintenance of a proper fluid solution for the cardiac myocyte survival. Moreover, the chip-holder should accommodate for additional placement of fluid surrounding the chips for extra moistening.

The experimental setup has shown to maintain a steady absolute peak pressure during the entire experiment. However, we should note that occasionally a heart rhythm fluctuation occurs due to a Labview control flaw.

5.4.2 Cardiac myocyte results

From the initial experiments it was concluded that the moving substrate has no detrimental impact on the cardiac myocytes' attachment. The cardiac myocytes remained anchored to the moving substrate over a long period of time ($>120h$). We can therefore carefully state that substrate movement mimics some of the cardiac myocyte environment *in vivo*. Furthermore we are able to conclude that PDMS is a proper substrate for cardiac myocyte anchorage, and the material can withstand long-term extensive stretching, without permanently deforming.

Moreover a conclusion can be drawn relating the pressure protocol. From the failed second set of experiments we have seen that at larger pressures (approx. $7kPa$) the cardiac myocytes detach. From the first set of experiments we have however seen, that with the calculated loading conditions, the cardiac myocytes remain attached. We are thus able to conclude that the derived pressure protocol in Chapter 4 is in the right range. However, to obtain hard conclusion considering the pressure protocol, experiments should be performed with mono-layered cardiac myocytes and varying pressure protocols, and the maturation of the cells should be assessed.

PART V: CONCLUDING

6 Conclusions and Recommendations

In this chapter we recapitulate all conclusions and recommendations considering this project. The concluding remarks relating to the outcomes of the study objectives, presented in Section 1.3 are discussed in Section 6.1:

- Gain insight in the strain cardiomyocytes have to endure *in vivo*.
- Determine the membrane behavior of both Cytostretch configurations, in order to determine how the amount of applied pressure relates to membrane stretch.

Furthermore, the conclusions will be presented considering the preliminary experiments discussed in Chapter 5. Finally recommendations for future work considering the Cytostretch project will be presented in Section 6.2.

6.1 Conclusions

6.1.1 Left ventricle mechanics

The strain cardiomyocytes endure *in vivo* has been determined from the derivation of left ventricle mechanics. The left ventricle is the largest, most muscular part of the heart, and cells situated in the left ventricle wall will endure the largest strains.

For the calculations of the left ventricle mechanics, we can conclude that the left ventricle can be assumed to be a rotationally symmetric thick-walled structure, build-up out of a fibrous structure embedded in soft incompressible material.

As a result of evolution, and from previous anatomical fiber angle findings [30] we can assume that the left ventricular fiber stress can be considered homogeneously distributed over the wall. The normal heart myofiber structure and geometry will adapt, until load is evenly distributed. Furthermore, the fiber direction related to a homogeneous stress distribution corresponds with experimentally derived values [40]. Thus the conclusion can be made that the left ventricular fiber stress (and corresponding fiber strain) can be approximated by a single value. For the determination of a proper loading protocol for the Cytostretch experiments we are thus able to consider one strain value for the cardiomyocytes.

We can conclude from the left ventricle calculations (Chapter 2), that when assuming this homogeneous stress distribution, the fiber stress as a function ventricle pressure depends mainly on the ratio of cavity volume over wall volume. Moreover, we can conclude that the shape of the left ventricular representation is of minor importance.

The relation between fiber stress and cavity volume leads to the fiber strain with use of the principle of conservation of energy. The conclusion can be drawn that the left ventricle mechanics can be approximated by the simple approximations of:

$$\frac{\sigma_f}{P_{lv}} = 1 + 3 \frac{V_{lv}}{V_w} \quad 2.35$$

$$\Delta \varepsilon_f = \frac{1}{3} \Delta \ln \left(1 + 3 \frac{V_{lv}}{V_w} \right) \quad 2.43$$

In Equations 2.35 and 2.43, σ_r is the left ventricular fiber stress, P_v the left ventricular pressure. V_v is the left ventricular cavity volume, V_w the left ventricular wall volume and $\Delta\epsilon$ the natural fiber strain.

The accuracy of Equation 2.32 is essential for the derivation of accurate fiber stress and strain. We have seen that the error in the equation is expressed by the term V_{err} in Equation 2.31.

$$V_{sh} = \frac{3\Delta P(V + V_{err})}{\sigma_f} \quad 2.31$$

$$\frac{\Delta P}{\sigma_f} = \frac{V_{sh}}{3V} \quad 2.32$$

This error term equals zero if the volume is closed with a finite radius or the derivative dr/dz is zero at the boundary. This, however, is not the case at the basal boundary of the left-ventricle, where the basal boundary is open without the derivative dr/dz being zero at that boundary.

The left-ventricle can be seen as a prolate ellipsoid, being cut-off at the upper end, with a long to short axis ratio of 2 or more [43]. If we consider a minor axis of $2R$ and a major to minor axis ratio of a , with the centre at the origin and cut-off at $z=z_{max}$. For $a \geq 2$, a typical ellipsoid, resembling the shape of the left ventricle, we obtain an error of less than 2.78%. We can thus conclude that the volume accuracy lies within 2.78 percent. And the effect on the fiber stress is less than 8.34 percent.

The calculations of the left ventricular fiber strain in Section 2.2.3 lead to the conclusion that for a healthy adult heart the absolute strain between end systole and end diastole equals an approximate 14.7 percent.

Salameh *et al.* [50] uni-axially strained cardiomyocytes at three different strain values, 5%, 10% and 20%. 24-hour cyclic mechanical stretch resulted in an increased percentage of cells with an elongated phenotype. They discovered that the percentage of elongated cells was dependent on the intensity of the stretch, 10% and 20% stretch generated significantly more elongated cells than 5% stretch. There was no significant difference in percentage of elongated cells between 10 and 20% stretch. From this we are able to make the statement that the left ventricle calculations lead to reasonable fiber strains, applicable for the Cytostretch experiments.

6.1.2 Membrane mechanics

We are able to conclude that a simply supported analytical model, considering a two-dimensional, $16.5\mu m$ thickness representation describes the dogbone membrane behavior properly. For this model we assume a linear elastic homogeneous isotropic material, from which we have seen that the error with the experimentally determined values remains small. The determination of the membrane behavior by means of a potential energy method has shown to provide correct outcomes. However, the right trial function, and boundary conditions are essential. We can state that both the in plane displacement u and the deflection play a big role in the accuracy of the analytical outcome. The trial in plane displacement functions show to have a big effect on the strain outcomes, whereas the trial deflection displacement functions influence both in plane and out of plane displacements to a large extend.

Similarly, a three-dimensional, analytical mode supported at the edge, describes the behavior of the circular membrane properly. Here we are able to consider a $21.5\mu m$ thickness representation, assuming a linear elastic homogeneous isotropic material.

We can furthermore state that the membrane behavior of both membrane configurations depends mainly on the extensional energy density. When lower ($<3kPa$) pressure is applied, extensional and bending strain energy determines the membrane's behavior. However, when applying larger amounts of pressure, the bending strain energy fails to participate in the

membrane's behavior. This is due to the fact that the membrane has a very small thickness to area ratio, and the deflection is very large.

In the dogbone membrane, the axial strain (transverse on the cardiomyocytes) shows to be nicely homogeneously distributed. This will result in a similarity in transverse stretch of all the cells situated on the membrane. However, in the circular membrane the transverse strain increases towards the centre. The transverse strain (on the bottom of the grooves) in the centre of the membrane resembles the radial strain. This will result in cardiomyocytes equally stretched longitudinally and transversally in the central region of the membrane. However, the cardiomyocytes in the outer regions of the membrane will barely receive transverse stretch, although their longitudinal stretch will be equal to the centrally plated cells.

We can conclude that when we consider the dogbone membrane, we will need to apply 3.725kPa to obtain the desired amount of strain of 14.7% on the cardiomyocytes situated in the grooves of the membrane (Section 2.4). For the circular membrane, to obtain the same desired amount of strain of 14.7%, a pressure of 5.375kPa needs to be applied.

The pressure protocol must be adjusted to the membrane configuration implemented in the experiment. From a typical ventricular volume – time relationship, we can conclude that approximately two-third of the time-span of one second per heartbeat the heart is filling, and one-third of the time the heart is ejecting. Moreover, both filling and ejection phase show an exponential upstroke function and an exponential down stroke function. Widely stated, the left ventricle volume shows a blunted block-function over time. For preliminary testing implementation of a block-function including some build-in delay will approach the *in vivo* left ventricle volume over time relation. For experiments including dogbone membranes a block-function with an absolute peak pressure of no more than 3.725kPa should be introduced, whereas for experiments including circular membranes a block-function with an absolute peak pressure of no more than 5.375kPa should be introduced.

6.1.3 Preliminary experiments

We can conclude that the experimental setup maintains a steady absolute peak pressure during the entire experiment.

Furthermore, we are able to conclude that the moving substrate does not bother the cardiac myocytes. The cardiac myocytes remained anchored to the moving substrate over a long period of time. We can therefore carefully state that substrate movement mimics some of the cardiac myocyte environment *in vivo*. Furthermore we are able to conclude that PDMS is a proper substrate for cardiac myocyte anchorage, and the material can withstand long-term extreme stretching, without permanently deforming.

Moreover a conclusion can be drawn relating the pressure protocol. From the failed second set of experiments we have seen that at larger pressures (7kPa) than determined the cardiac myocytes detach. From the first set of experiments we have however seen, that with the calculated loading conditions, the cardiac myocytes remain attached over a long period of time. We can thus conclude that the derived pressure protocol in Chapter 4 is in the correct range.

6.1.4 Overall conclusions

The fact that the moving substrate has no detrimental impact on the cardiomyocytes proves that the Cytostretch project has great potential. However, we are able to state that for proper determination of the effect of the separate strain components (longitudinal and transverse) attention should be paid to the Cytostretch configurations. The outcomes of the analytical model described in Chapter 4 lead to the conclusion that the circular configuration does not meet the demands. Although we have not considered transverse strain in the human left ventricle model described in Chapter 2, out of evolution considerations, we can state that equal to the longitudinal cardiac muscle stress, the transverse muscle stress will be likewise homogeneously distributed. This homogeneity will only be obtained in the centre section of the circular membrane.

Furthermore, for a proper determination of the effect of the separate strain components (longitudinal and transverse), both strain directions and the combined two should be tested

simultaneously, meaning that the both the circular as well as the dogbone configuration including anchored cells should be incorporated in the stretch setup at the same time to ensure equal conditions. From Chapter 4 we can draw the conclusion that with the current dimensions this will not be feasible.

Equally, issues are encountered with the current proposed interconnect design for the circular membrane. The helical formed interconnects maintain function due to uncoiling when the membrane is pulled into a concave state. However, the rigidity of the coils will affect the strain in the membrane, the transverse strain will damp out as a result of the added interconnects, leaving the circular chip to be a uni-directional stretching device. From this we can conclude that in the current state, the circular membrane is not suitable for proper multi-directional cardiomyocyte stretching.

The dogbone configuration on the other hand shows great potential for its purpose, namely uni-directional cardiomyocyte stretching, when the cells do indeed anchor in the desired direction on the centre-section of the membrane. From the numerical approximations presented in Appendix 1 we can conclude that the centre section of the dogbone membrane does inflate cylindrically as desired, resulting in strain in solely one direction.

6.2 Recommendations

6.2.1 Left ventricle mechanics

We should note that the left ventricular fiber strain is calculated for a healthy adult heart, as there is much MRI (magnetic resonance imaging) data available containing cavity and wall volume measures. The cardiomyocytes, used for the experiments, are however in a much lower maturation stage. From literature it is assumed that the left ventricular cavity volume over wall volume is in a specific range, valid for any stage of development [33]. It is assumed that the left ventricle wall growth is proportional to the left ventricular cavity increase during development. For a validation of the derived strain values the above statement should be checked. Left ventricular cavity and wall measures should be considered for embryonic hearts.

Furthermore, the development of cavity volume over wall volume should be analyzed in order to determine whether this ratio stays uniform. This assessment could for example be performed by observation of MRI data at several developmental stages of the human heart. When non-uniformity exists in the cavity volume over wall volume ratio, this should be taken into account, pressure during experimental testing should be varied over time.

Although the outcome of the calculations seems reasonable, we should take into account that various simplifications have been made in order to describe the mechanics of the left ventricle with reduced calculation time. Biological tissue contains many structural components. In the derivation of the left ventricle mechanics, the material is assumed as a fluid-fiber continuum, as the incompressible fluid like material and muscle fibers are the most distinct components. The next component, which provides consistency of the left ventricle material, is collagen. Collagen exists in the left ventricular wall in a matrix structure, and could have effect on the left ventricular fiber mechanics. For increased accuracy a fluid-fiber-collagen continuum could be considered in the derivation of the left ventricular strain.

Chadwick *et al.* [38] described the left ventricle mechanics according to the model of Arts *et al.* [32] with an additional collagen matrix, compared the two material models [36-38] and discovered that the contribution of the collagen matrix to the elasticity of the material is critically dependent on the helical pitch angle of the collagen matrix, the effect shows to be maximal when the pitch angle of the collagen matrix equals that of the muscle fiber (Section 2.2). Moreover, the collagen matrix appears to affect stiffness in end systole as well as end diastole (reference is taken at dead volume 45ml). The elongation between end systole and the reference volume (dead volume) deviates by less than 8 percent from the elongation between end diastole and reference volume when assuming homogeneity in fiber strain over the wall. Incorporation of collagen in the material model could thus result in a lowered fiber strain by a maximal 8 percent.

6.2.2 Membrane mechanics

For enhanced accuracy of the membrane behavior and with that an optimized pressure protocol, future work lies in the optimization of the analytical model describing the membrane behavior. Below, areas for future work on the membrane model are presented, to increase accuracy.

We have seen that for a proper description of the edge effects in the potential energy of the membranes also the shear deformations due to transverse forces should be taken into account. For future work, new calculations could be performed including the transverse forces, for further clarification of the edge effects. When including these shear deformations, one should also apply the formulation of clamped boundaries, as they introduce the effect.

We have noticed that analytical approximation shows a small upward shift as compared to the experimental deflection, which could have several causes. We have also noticed that it is likely that some of the shift is caused by ill prediction of the stiffness of the PDMS membrane. For a better accuracy of the analytical model, the exact stiffness of the membrane is essential. Therefore, future work on this project should include the exact determination of the membrane parameters.

There is a possibility that a linear elastic material model simply cannot model the PDMS membrane accurately. It would be recommendable to introduce a hyperelastic material model. A Neo-Hookean or Mooney-Rivlin material could be implemented in the applied analytical model (Appendix 4).

In the membrane experiments the centre of the membrane is visually determined. An offset from the actual centre of the membrane could result in a shifted load-deflection relation of the membrane. To exclude this factor, an experimental load-deflection study could be done with the determination of the deflection by side-view.

Furthermore, the shift could also be due to the definition of deflection and corresponding membrane compliancy. We make a comparison solely on the centre-deflection of the membrane. However, the actual comparison should be made according to the total deflection of the membrane. The deflected shape depends on many variables. We for instance model the behavior of the membrane by a distributed load, for simplification reasons. The true membrane obviously is subjected to a follower load, leading to a more globular deflected membrane. One could imagine the centre-deflection of a more globular shaped membrane to be lower than the centre-deflection of a more egg-shaped membrane. Future work lies in the determination of the membrane deflection, by describing the entire deflection of the membrane. Which could be realized by determination and comparison of the deflection by integration of the total deflection over the surface. To be able to do that the total deflected shape of the membrane should also be determined experimentally.

When we consider the displacement u , determined experimentally, we have seen some major difficulties, leading to experimental results from which no hard conclusions can be drawn. For further validation of the displacement field in the analytical model, it is highly recommended to extensively determine the displacement u of the membrane. For an accurate tracking of the particles several sequences of pictures could be made, taking a different focal area per sequence in order to obtain more tracked particles. When more particles are tracked a trend will probably become more apparent and the edge effects will probably also become visible.

We have seen that due to the desire of the cardiomyocytes to anchor in corners, the strain in the grooves is of main concern, while we so far have only determined the overall (leading) membrane strain. We have also witnessed that this strain is not equal to the leading membrane strain. In the derivation of the groove strain we have assumed that the ratio of groove strain over leading membrane strain versus pressure behaves linearly. It is recommended to analyze this statement of linearity. The examination of the relation between groove strain and overall membrane strain could include the usage of a weight method, leading to the determination of the constricting role of the block material on top of the membrane by their relative weight.

6.2.3 Preliminary experiments

We have observed that the incubator environment promotes oxidation processes. The humidity and various metal components present cause oxidation processes even of metals, which are relatively oxidation stable. For future work on the Cytostretch chip-holder non-metal components should be used for placement inside the incubator.

Furthermore, the low medium container of the Cytostretch chip introduces problems concerning the cells' humidity and mineral concentration. A suitable lid appears to be essential for the maintenance of a proper fluid solution for the cardiac myocyte survival. Moreover, the chip-holder should accommodate for additional placement of fluid surrounding the chips for extra moistening. Recommended is to ensure humidity for the cardiomyocytes at all times. Ideas for future work is either the enlargement of the medium container situated on the chip, or the development of a fluid-container incorporated in the chip-holder and a suitable lid.

We have seen that occasionally a heart rhythm fluctuation occurs due to a Labview control flaw. For a better control of the stretch protocol, the source of these fluctuations should be analyzed.

Moreover, to obtain hard conclusions concerning the pressure protocol, experiments should be preformed with mono-layered cardiac myocytes and varying pressure protocols, from which the maturation of the cells should be assessed.

6.2.4 Overall recommendations

It is highly recommended to assess new membrane configurations and dimensions. First of all it is highly preferable to have two membrane configurations, which can be strained in the same setup with equal loading conditions. When narrowing the dogbone membrane down to a central width of approximately $850\mu m$, or increasing the circular membrane with a factor of approximately 2, an equal pressure protocol can be applied.

Furthermore, another solution for multi-axial loading should be investigated. The transverse strain on the circular membrane is far from uniform, and with the proposed interconnect design the transverse strain will approach zero. Recommended is to assess the potential of a squared membrane with centrally located grooves or fibronectin coating.

The preliminary experiments showed great potential for further testing. Future research should be done in assessing the pressure protocol. When it appears that cell stretch increases the cells' maturity stage, one could vary the applied loading protocol in order to determine whether the derived protocol is optimal.

During this study, assumed is the anchorage of cardiomyocytes in the corners of the grooves, as analyzed in earlier studies (Section 1.2.2). A future study objective could be the determination of the exact anchorage location of the cardiomyocytes. The outcome could be incorporated in the development of the loading protocol, where currently the cell strain is assumed to be equal to the membrane strain inside the grooves. Moreover, it is recommended that the effect of the cardiomyocytes and vice versa is determined. A negligible effect is expected of the cardiomyocytes on the PDMS membrane, as the stiffness of PDMS is in the order of two magnitudes higher. However, the PDMS will therefore restrict the cardiomyocytes in contraction. A related future research topic is therefore lowering the stiffness of PDMS, which can be realized by one of the methods mentioned in Section 1.2.1. During this study, the development of a lower stiffness PDMS membrane is already initiated.

Furthermore, to obtain a more homogeneous strain distribution inside the grooves, it would be recommendable to analyze the optimal groove width to "in between groove" width ratio. Expected would be, when increasing this ratio, and thus decreasing the effect of "dead" material on top of the membrane, the groove strain will become more homogeneous.

Recommended for further work on the Cytostretch chips, is to simplify future chip scaling. On one hand this could be realized by decreasing the tolerance on the chips, for an easy implementation of the chips in a scaling and stretching device. Then a chip-holder could be produced in which the chips can be easily clicked in and out. This will create a more rigid connection and lowering the probability of crushing the silicone chip during clamping. Furthermore it will become less labour intensive and easier to move the chips, resulting in less medium spill. On the other hand, this could be realized by rigidly connecting several chips, which can be stretched simultaneously. During this study, investigation of the last method already started.

Bibliography

1. Radisic, M., H. Park, H. Shing, T. Consi, F. Schoen, R. Langer, L. Freed, and G. Vunjak-Novakovic, *Functional assembly of engineered myocardium by electrical stimulation of cardiac myocytes cultured on scaffolds*. Proceedings of the National Academy of Sciences of the United States of America, 2004. **101**(52): p. 18129.
2. Braam, S.R., *Human embryonic stem cells: Advancing biology and cardiogenesis towards functional applications*, in *Anatomy and Embryology*2010, Leiden University Medical Center: Leiden. p. 170.
3. Parker, K., J. Tan, C. Chen, and L. Tung, *Myofibrillar architecture in engineered cardiac myocytes*. Circulation research, 2008.
4. Feinberg, A., A. Feigel, S. Shevkopyas, S. Sheehy, G. Whitesides, and K. Parker, *Muscular thin films for building actuators and powering devices*. Science, 2007. **317**(5843): p. 1366.
5. Fujii, T., *PDMS-based microfluidic devices for biomedical applications*. Microelectronic Engineering, 2002. **61**: p. 907-914.
6. Leclerc, E., Y. Sakai, and T. Fujii, *Cell culture in 3-dimensional microfluidic structure of PDMS (polydimethylsiloxane)*. Biomedical microdevices, 2003. **5**(2): p. 109-114.
7. Leclerc, E., Y. Sakai, and T. Fujii, *Microfluidic PDMS (Polydimethylsiloxane) Bioreactor for Large Scale Culture of Hepatocytes*. Biotechnology progress, 2004. **20**(3): p. 750-755.
8. van Kooten, T., J. Whitesides, and A. von Recum, *Influence of silicone (PDMS) surface texture on human skin fibroblast proliferation as determined by cell cycle analysis*. Journal of Biomedical Materials Research Part B: Applied Biomaterials, 1998. **43**(1): p. 1-14.
9. Liu, M., J. Sun, Y. Sun, C. Bock, and Q. Chen, *Thickness-dependent mechanical properties of polydimethylsiloxane membranes*. Journal of Micromechanics and Microengineering, 2009. **19**: p. 035028.
10. Thangawng, A., R. Ruoff, M. Swartz, and M. Glucksberg, *An ultra-thin PDMS membrane as a bio/micro/nano interface: fabrication and characterization*. Biomedical microdevices, 2007. **9**(4): p. 587-595.
11. Mata, A., A. Fleischman, and S. Roy, *Characterization of polydimethylsiloxane (PDMS) properties for biomedical micro/nanosystems*. Biomedical microdevices, 2005. **7**(4): p. 281-293.
12. Schneider, F., T. Fellner, J. Wilde, and U. Wallrabe, *Mechanical properties of silicones for MEMS*. Journal of Micromechanics and Microengineering, 2008. **18**: p. 065008.
13. Mark, J. and Knovel, *Polymer data handbook*1999: Oxford University Press New York.
14. Ruoslahti, E., *Fibronectin*. Journal of Oral Pathology & Medicine, 1981. **10**(1): p. 3-13.
15. Parker, K., A. BROCK, C. BRANGWYNNE, R. MANNIX, N. WANG, E. OSTUNI, N. GEISSE, J. ADAMS, G. WHITESIDES, and D. INGBER, *Directional control of lamellipodia extension by constraining cell shape and orienting cell tractional forces*. The FASEB Journal, 2002. **16**(10): p. 1195.
16. Parkazad, S.K., *A stretchable Multi-Electrode Array (MEA) for cardio-toxicity drug screening applications*, in *Electrical Engineering*2010, TU Delft: Delft. p. 54.
17. Huisman, R., P. Sipkema, N. Westerhof, and G. Elzinga, *Comparison of models used to calculate left ventricular wall force*. Medical and Biological Engineering and Computing, 1980. **18**(2): p. 133-144.
18. Sandler, H. and H. Dodge, *Left ventricular tension and stress in man*. Circulation research, 1963. **13**(2): p. 91.
19. Mirsky, I., *Left ventricular stresses in the intact human heart*. Biophysical journal, 1969. **9**(2): p. 189-208.
20. Wong, A. and P. Rautaharju, *Stress distribution within the left ventricular wall approximated as a thick ellipsoidal shell* 1*. American Heart Journal, 1968. **75**(5): p. 649-662.
21. Falsetti, H., R. Mates, C. GRANT, D. GREENE, and I. BUNNELL, *Left ventricular wall stress calculated from one-plane cineangiography: an approach to force-velocity analysis in man*. Circulation research, 1970. **26**(1): p. 71.
22. Wong, A., *Myocardial mechanics: application of sliding-filament theory to isovolumic concentration of the left ventricle*. Journal of biomechanics, 1973. **6**(5): p. 565-581.
23. Mirsky, I., *Ventricular and arterial wall stresses based on large deformation analyses*. Biophysical journal, 1973. **13**(11): p. 1141-1159.
24. Janz, R., *Estimation of local myocardial stress*. American Journal of Physiology- Heart and Circulatory Physiology, 1982. **242**(5): p. H875.

25. Chaudhry, H., B. Bukiet, A. Davis, and T. FINDLEY, *Stresses and strains in the left ventricular wall approximated as a thick conical shell using large deformation theory*. J. Biol. Systems, 1996.
26. Chaudhry, H., B. Bukiet, T. Findley, and A. Ritter, *Stresses and strains in the passive left ventricle*. Journal of Biological Systems, 1996. **4**(4): p. 535-554.
27. Chaudhry, H., B. Bukiet, and T. Regan, *Dynamic stresses and strains in the left ventricular wall based on large deformation theory*. International Journal of Non-Linear Mechanics, 1997. **32**(3): p. 621-631.
28. Taber, L., *On a nonlinear theory for muscle shells: part ii: application to the beating left ventricle*. Journal of Biomechanical Engineering, 1991. **113**: p. 63.
29. Feit, T., *Diastolic pressure-volume relations and distribution of pressure and fiber extension across the wall of a model left ventricle*. Biophysical journal, 1979. **28**(1): p. 143-166.
30. Streeter Jr, D. and W. Hanna, *Engineering mechanics for successive states in canine left ventricular myocardium: II. Fiber angle and sarcomere length*. Circulation research, 1973. **33**(6): p. 656.
31. Streeter Jr, D., H. Spotnitz, D. Patel, J. ROSS Jr, and E. Sonnenblick, *Fiber orientation in the canine left ventricle during diastole and systole*. Circulation research, 1969. **24**(3): p. 339.
32. Arts, T., R. Reneman, and P. Veenstra, *A model of the mechanics of the left ventricle*. Annals of biomedical engineering, 1979. **7**(3): p. 299-318.
33. Arts, T., P. Bovendeerd, T. Delhaas, and F. Prinzen, *Modeling the relation between cardiac pump function and myofiber mechanics*. Journal of biomechanics, 2003. **36**(5): p. 731-736.
34. Arts, T. and R. Reneman, *Dynamics of left ventricular wall and mitral valve mechanics--a model study*. Journal of biomechanics, 1989. **22**(3): p. 261-271.
35. Arts, T., P. Veenstra, and R. Reneman, *Epicardial deformation and left ventricular wall mechanisms during ejection in the dog*. American Journal of Physiology- Heart and Circulatory Physiology, 1982. **243**(3): p. H379.
36. Aldroubi, A. and R. Chadwick, *On the uniqueness of quasi-static solutions of some linear models of left ventricular mechanics*. Mathematical biosciences, 1990. **99**(2): p. 195-203.
37. Chadwick, R., *Mechanics of the left ventricle*. Biophysical journal, 1982. **39**(3): p. 279-288.
38. Ohayon, J. and R. Chadwick, *Effects of collagen microstructure on the mechanics of the left ventricle*. Biophysical journal, 1988. **54**(6): p. 1077-1088.
39. Mirsky, I., *Elastic properties of the myocardium: a quantitative approach with physiological and clinical applications*. Handbook of Physiology. The Cardiovascular System. The Heart, 1979: p. 497-531.
40. Waldman, L., D. Nosan, F. Villarreal, and J. Covell, *Relation between transmural deformation and local myofiber direction in canine left ventricle*. Circulation research, 1988. **63**(3): p. 550.
41. Ubbink, S., P. Bovendeerd, T. Delhaas, T. Arts, and F. van de Vosse, *Towards model-based analysis of cardiac MR tagging data: relation between left ventricular shear strain and myofiber orientation*. Medical image analysis, 2006. **10**(4): p. 632-641.
42. Bovendeerd, P., T. Arts, J. Huyghe, D. Van Campen, and R. Reneman, *Dependence of local left ventricular wall mechanics on myocardial fiber orientation: a model study*. Journal of biomechanics, 1992. **25**(10): p. 1129-1140.
43. Arts, T., P. Bovendeerd, F. Prinzen, and R. Reneman, *Relation between left ventricular cavity pressure and volume and systolic fiber stress and strain in the wall*. Biophysical journal, 1991. **59**(1): p. 93-102.
44. Rutter, J., *Geometry of curves*2000: Chapman & Hall/CRC.
45. Busemann, H., *Convex surfaces*1958: Interscience publishers.
46. Regen, D., *Myocardial stress equations: Fiberstresses of the prolate spheroid**. Journal of theoretical biology, 1984. **109**(2): p. 191-215.
47. Weisstein, E.W. *Prolate Spheroid*. Available from: <http://mathworld.wolfram.com/ProlateSpheroid.html>.
48. Weisstein, E.W. *Ellipsoid*. Available from: <http://mathworld.wolfram.com/Ellipsoid.html>.
49. Bentea, E. *Ellipsoidal cap*. 2006; Available from: <http://www.codecogs.com>.
50. Salameh, A., A. Wustmann, S. Karl, K. Blanke, D. Apel, D. Rojas-Gomez, H. Franke, F. Mohr, J. Janousek, and S. Dhein, *Cyclic Mechanical Stretch Induces Cardiomyocyte Orientation and Polarization of the Gap Junction Protein Connexin43*. Circulation research, 2010.
51. Blaauwendraad, J., *Plates and Fem: Surprises and Pitfalls*2010: Springer Verlag.
52. Timoshenko, S., S. Woinowsky-Krieger, and S. Woinowsky, *Theory of plates and shells* 1959: McGraw-Hill New York.
53. Senturia, S., *Microsystem design* 2001: Springer Netherlands.
54. Rogers S.S., W.T.A., Zhao X. and Lu J.R., *Precise Particle Tracking Against a Complicated Background: Polynomial Fitting with Gaussian Weight*. Physical Biology, 2007. **4**(3): p. 220-227.
55. Mummery, C., D. Ward, and R. Passier, *Differentiation of Human Embryonic Stem Cells to Cardiomyocytes by Coculture with Endoderm in Serum Free Medium*. 2004.
56. *STMicroelectronics*. Available from: <http://www.st.com>.
57. *Freescale Semiconductor*. [cited 2004; Available from: <http://www.freescale.com>].

PART VI: APPENDICES

APPENDIX 1 NUMERICAL MODEL

For the numerical model use is made of the finite element package of COMSOL multiphysics 4.0a. For all the numerical models a linear-elastic material model is applied, except for the model used in Appendix 4 for which a Neo-Hookean material model is implemented.

For the numerical model the following material parameters are set (equal to the material parameters introduced in the analytical model):

Young's modulus:	1MPa
Density:	960kg/m ³
Poisson's ratio:	0.499

For the determination of the deflection, displacement and strain values and graphs, use is made of numerical models consisting of shell elements (Figure 107 and Figure 108). Shell elements describe the behavior of a very thin membrane most accurately, as they are able to divide the thickness of the membrane into many elements. Furthermore, solid elements when they become too thin do not have the capability to derive differential equations between the two thickness points of an element, and an error occurs. Shell elements do have the ability to derive these equations for the description of very thin elements.

When we however want to implement the grooves, for example the determination of the thickness of the uniform representation (Appendix 3), we have to apply solid elements. The models containing solid elements are solely used to find a relation between a uniform thickness representation and true grooved membrane (Figure 109 and Figure 110).

For the visualization of the possibility to use two-dimensional representations in the case of the dogbone membrane, two-dimensional models are used with solid elements (Figure 111 and Figure 112). This model is also solely used for visual purposes. For both the three-dimensional solid models as the two-dimensional solid models a mapped and subsequently swept mesh is introduced, to make sure that the solid contains more than one thickness element. By mapping a 5 element thick mesh is introduced.

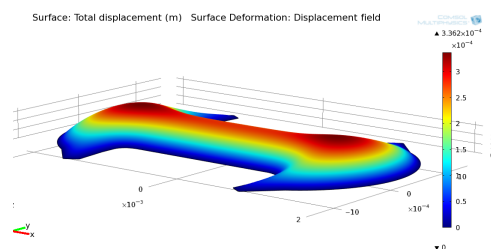


Figure 107: Uniform thickness representation of the dogbone; a numerical model build up from shell elements.

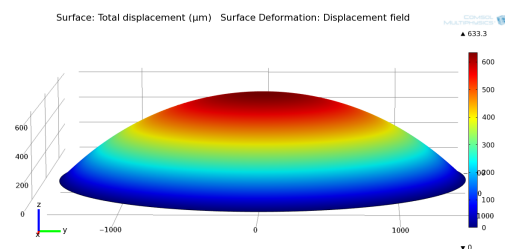


Figure 108: Uniform thickness representation of the circular membrane; a numerical model build up from shell elements.

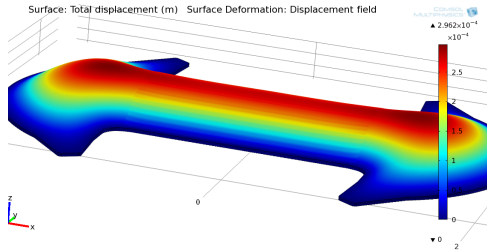


Figure 109: Grooved membrane including true dimension of the dogbone; a numerical model build up from solid elements (5 thickness elements). This model is solely used for visualization purposes.

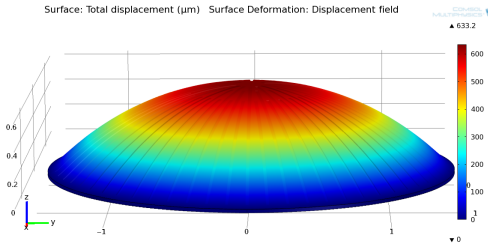


Figure 110: Grooved membrane including true dimension of the circular membrane; a numerical model build up from solid elements (5 thickness elements), solely used for visualization purposes.

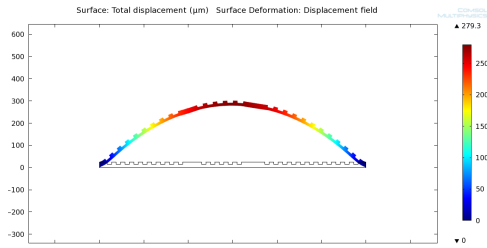


Figure 111: Grooved two-dimensional representation of the dogbone; a numerical model build up from solid elements (5 thickness elements). This model is solely used for visualization purposes.

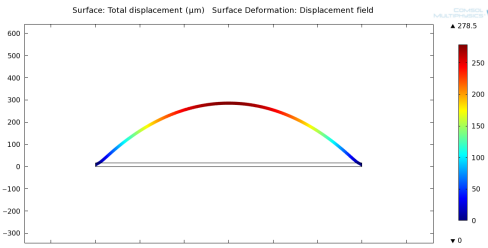


Figure 112: Two-dimensional uniform thickness representation of the dogbone; a numerical model build up from solid elements (5 thickness elements). This model is solely used for visualization purposes.

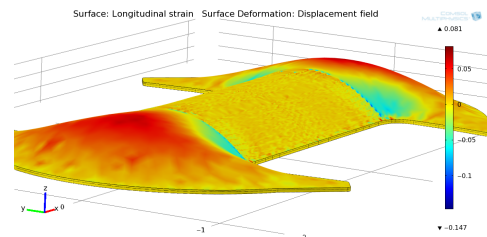


Figure 113: Longitudinal strain in the dogbone membrane, notice that the strain over the long axis of the membrane indeed equals zero in the centre section of the membrane. Therefore, we are able to model the behavior of the centre section of the dogbone membrane two-dimensional.

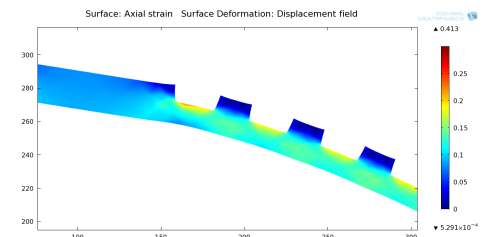


Figure 114: Close-up of the groove strain of the dogbone membrane. Notice the constricting role of the “dead” material on top of the membrane, resulting in higher strain values inside the grooves. Furthermore, notice the non-uniformity of this groove strain.

APPENDIX 2 ADDITIONAL PLATE CALCULATIONS

The proof of Equation 3.60 can be done most easily by calculating back from Equation 3.60 to 3.59:

$$W_{\text{bending \& twisting}} = \frac{D}{2} \iint \left\{ \left(\frac{\partial^2 w}{\partial x^2} + \frac{\partial^2 w}{\partial y^2} \right)^2 - 2(1-\nu) \left[\frac{\partial^2 w}{\partial x^2} \frac{\partial^2 w}{\partial y^2} - \left(\frac{\partial^2 w}{\partial x \partial y} \right)^2 \right] \right\} dx dy \quad \text{A2.1}$$

When we now write out the entire equation, we obtain:

$$W_{\text{bending \& twisting}} = \frac{D}{2} \iint \left\{ \left(\frac{\partial^2 w}{\partial x^2} \right)^2 + \left(\frac{\partial^2 w}{\partial y^2} \right)^2 + 2 \frac{\partial^2 w}{\partial x^2} \frac{\partial^2 w}{\partial y^2} - 2 \frac{\partial^2 w}{\partial x^2} \frac{\partial^2 w}{\partial y^2} + 2 \left(\frac{\partial^2 w}{\partial x \partial y} \right)^2 + 2\nu \frac{\partial^2 w}{\partial x^2} \frac{\partial^2 w}{\partial y^2} - 2\nu \left(\frac{\partial^2 w}{\partial x \partial y} \right)^2 \right\} dx dy \quad \text{A2.2}$$

$$W_{\text{bending \& twisting}} = \frac{D}{2} \iint \left\{ \left(\frac{\partial^2 w}{\partial x^2} \right)^2 + \left(\frac{\partial^2 w}{\partial y^2} \right)^2 + 2\nu \left(\frac{\partial^2 w}{\partial x^2} \frac{\partial^2 w}{\partial y^2} \right) + 2(1-\nu) \left(\frac{\partial^2 w}{\partial x \partial y} \right)^2 \right\} dx dy \quad \text{A2.3}$$

Equation A2.3 again is equal to Equation 3.59.

APPENDIX 3 MEMBRANE THICKNESS

For the analytical calculations, simplifications have to be made. We assume a uniform thickness representation of the grooved membrane. The behavior, however, of the uniform representation should match the real membrane configuration for a good accuracy of the outcomes. The thickness of the uniform representation should be so, that the behavior of the uniform representation approaches the behavior of the membrane configuration including grooves.

In the dogbone membrane with longitudinal grooves, the leading bulk material is the lower part of the membrane (the bottom $15\mu\text{m}$ of the total $25\mu\text{m}$ thickness). The additional material (top parts of the membrane) has got little effect on the deflection of the membrane. The extra blocks of material have a small constricting role in the stretching of the membrane. They act mainly as dead material on top of the $15\mu\text{m}$ thick membrane, as can be seen in Figure 113.

The overall membrane strain and deflection of the dogbone membrane with longitudinal grooves is analytical approximated as a two-dimensional problem considering the material area, only taken as a continuous membrane. For the determination of the thickness of the membrane considered in the calculations of the analytical model, we compare the deflection and overall membrane strain of the finite element model with and without grooves, and vary the thickness of the membrane without grooves. For the dogbone membrane, a similarity in central deflection and overall membrane strain has been found at a thickness of approximately $16,5\mu\text{m}$ for the membrane without grooves (Figure 114 - Figure 117).

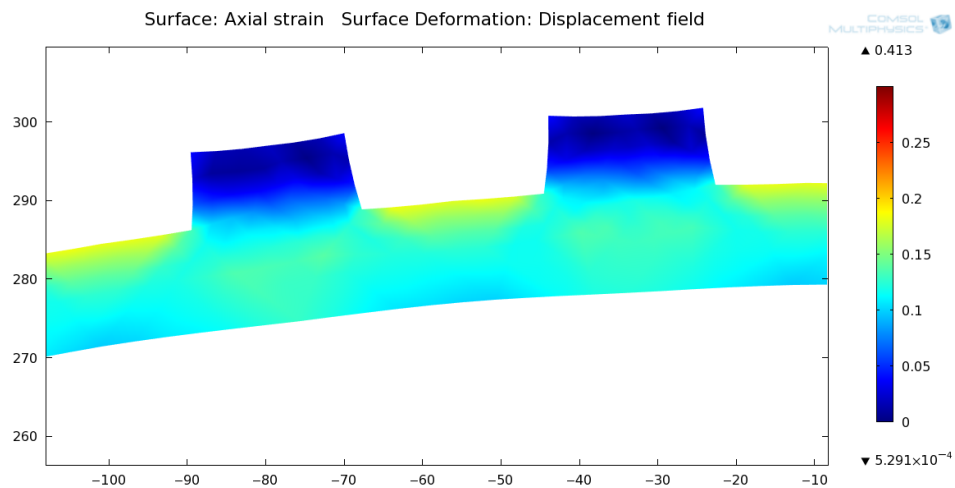


Figure 115: Close-up of the two-dimensional representation of the dogbone membrane, indicating that the material underneath the grooves mainly causes the leading membrane behavior. The tops of the grooves mainly act as dead material on top of the membrane; they do however have a small constricting role.

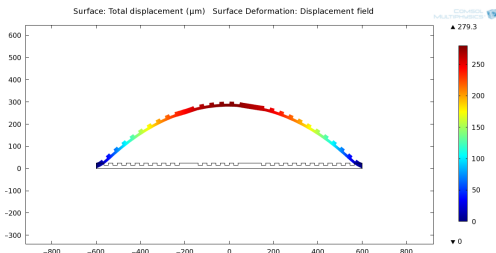


Figure 116: Two-dimensional representation of the dogbone membrane with the correct dimensions (including grooves). Notice that the deflection resembles the deflection of the $16.5\mu\text{m}$ uniform thickness representation (Figure 115).

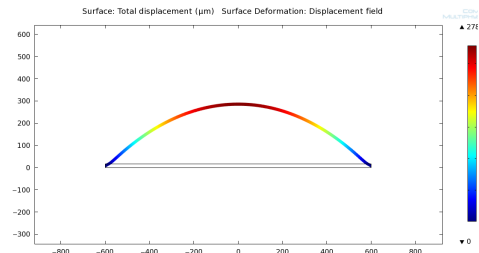


Figure 117: Two-dimensional uniform $16.5\mu\text{m}$ thickness representation of the dogbone membrane. Notice that the deflection resembles the deflection of the 2D representation including grooves (Figure 114).

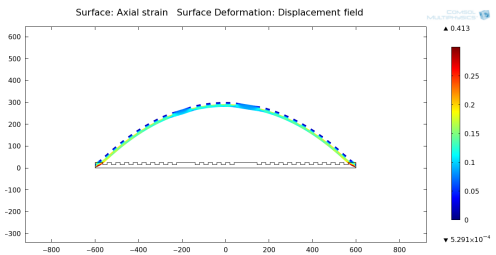


Figure 118: Two-dimensional representation of the dogbone membrane with the correct dimensions (including grooves). Notice that also the leading axial strain resembles the axial strain of the $16.5\mu\text{m}$ uniform thickness representation (Figure 117).

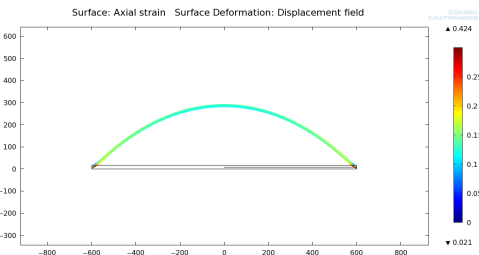


Figure 119: Two-dimensional uniform $16.5\mu\text{m}$ thickness representation of the dogbone membrane. Notice that also the axial strain resembles the leading axial strain of the 2D representation including grooves (Figure 116).

Notice that not only there is a similarity in the deflection of the $16.5\mu\text{m}$ thick uniform membrane and the original membrane with grooves, but also overall strain in both membranes shows to be similar. We are thus able to model the grooved membrane with a uniform $16.5\mu\text{m}$ thick membrane.

Figure 118 shows the deflection comparison as function of pressure. Notice that the deflection shows this similarity for a wide range of pressures.

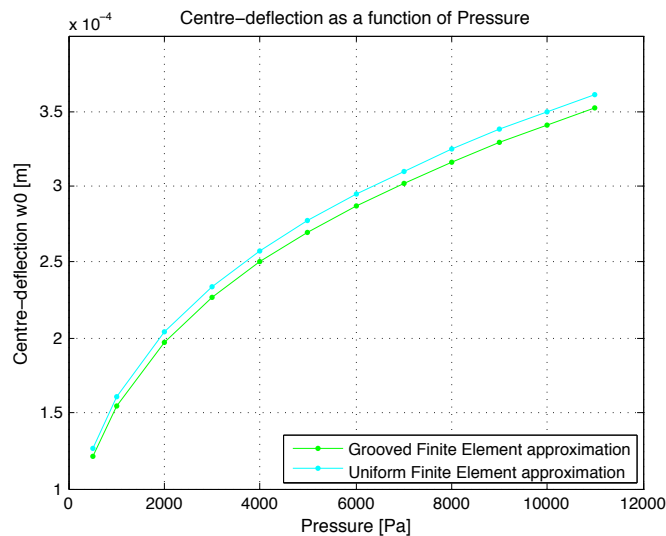


Figure 120: Deflection of the 2D representation of the dogbone including grooves (green line), and the deflection of the uniform $16.5\mu\text{m}$ thickness representation of the dogbone (cyan line), notice the nice correspondence between the two.

For the circular membrane, the grooves are situated radial. Notice from Figure 81 that the influence of the material between the grooves differs from that of the dogbone

configuration. The material between the grooves plays a bigger role in the behavior of the membrane. The material strips account for an equal share in taking up strain, thus playing a big constricting role on the uniform material underneath. For simplification reasons in the analytical approximation we are able to consider the membrane uniform with a thickness of $21.5\mu\text{m}$ (Figure 119 - Figure 123).

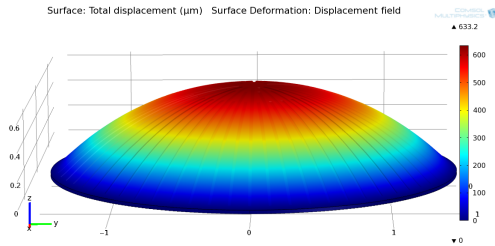


Figure 121: Three-dimensional representation of the circular membrane with the correct dimensions (including grooves). Notice that the deflection resembles the deflection of the $21.5\mu\text{m}$ uniform thickness representation (Figure 120).

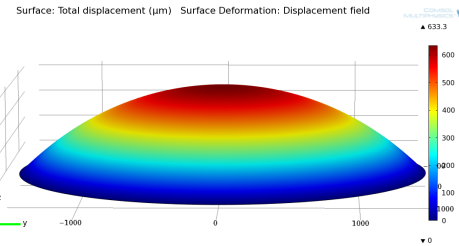


Figure 122: Three-dimensional uniform $21.5\mu\text{m}$ thickness representation of the circular membrane. Notice that the deflection resembles the deflection of the 3D representation including grooves (Figure 119).

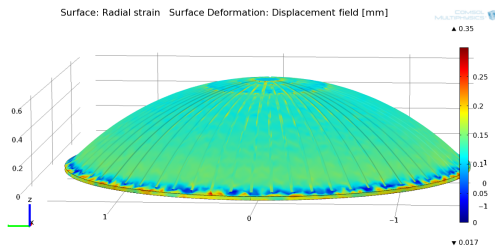


Figure 123: Three-dimensional representation of the circular membrane with the correct dimensions (including grooves). Notice that also the radial strain resembles the radial strain of the $21.5\mu\text{m}$ uniform thickness representation (Figure 122).

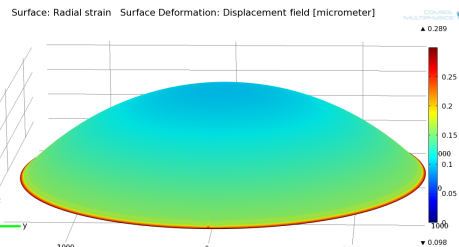


Figure 124: Three-dimensional uniform $21.5\mu\text{m}$ thickness representation of the circular membrane. Notice that also the radial strain resembles the radial strain of the 3D representation including grooves (Figure 121).

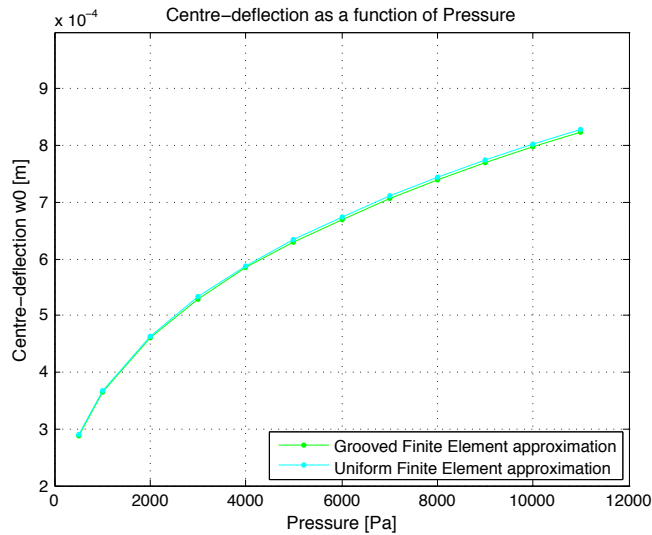


Figure 125: Deflection of the 2D representation of the circular membrane including grooves (green line), and the deflection of the uniform $21.5\mu\text{m}$ thickness representation of the circular membrane (cyan line), notice the nice correspondence between the two.

APPENDIX 4 HYPERELASTICITY

Here we introduce a hyperelastic material model, Neo-Hookean, in the numerical model for the dogbone membrane. With this introduction in the numerical model, and by comparison with the experimental deflection, more insight is gained in the material behavior of the membrane. We reduce the error, but still obtain some error in the pitch.

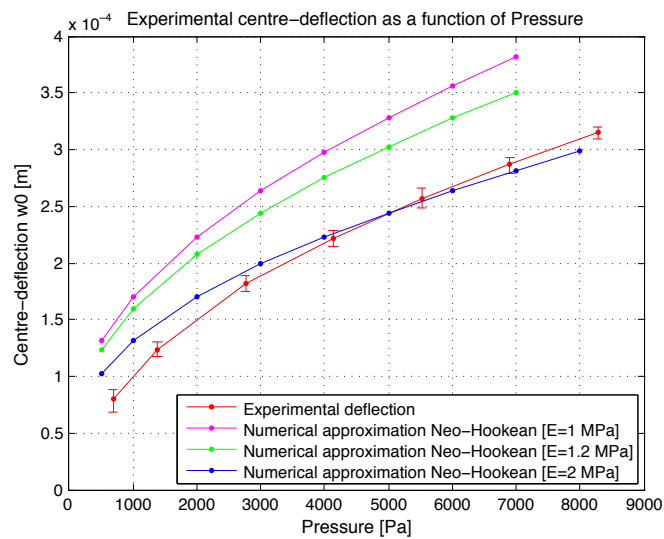


Figure 126: Experimental centre-deflection (red line), Neo-Hookean numerical approximation with $E=1\text{MPa}$ (magenta line), Neo-Hookean numerical approximation $E=1.2\text{MPa}$ (green line) and Neo-Hookean numerical approximation $E=2\text{MPa}$ (blue line) as function of applied pressure. Notice that the application of a hyperelastic material model also mainly changes the pitch angle.

In Figure 124 we assume an elastic, homogeneous, isotropic material. The stiffness of a Neo-Hookean material model is expressed in terms of lame-constants, and is proportional to the youngs-modulus in the following manner:

$$\mu = G = \frac{E}{2(1 + \nu)} \quad \text{A4.1}$$

$$\lambda = \frac{G(E - 2G)}{3G - E} \quad \text{A4.2}$$

Thus for the three cases represented in Figure 124 we obtain the following lame's constants:

$E_1 = 1\text{MPa}$	$\mu_1 = 333.56\text{kPa}$
	$\lambda_1 = 166.45\text{MPa}$
$E_2 = 1.2\text{MPa}$	$\mu_2 = 400.27\text{kPa}$
	$\lambda_2 = 197.4\text{MPa}$
$E_3 = 2\text{MPa}$	$\mu_3 = 667.11\text{kPa}$
	$\lambda_3 = 333.95\text{MPa}$

It could be interesting to implement a hyperelastic material model in the current analytical model. With a hyperelastic material model we are able to reduce some of the error, however, with a Neo-Hookean material model we do still obtain some error in the load-deflection behavior. More research should be done on the material description of the membranes, to be able to accurately describe the mechanics of the membranes.

APPENDIX 5 CIRCUIT DIAGRAM

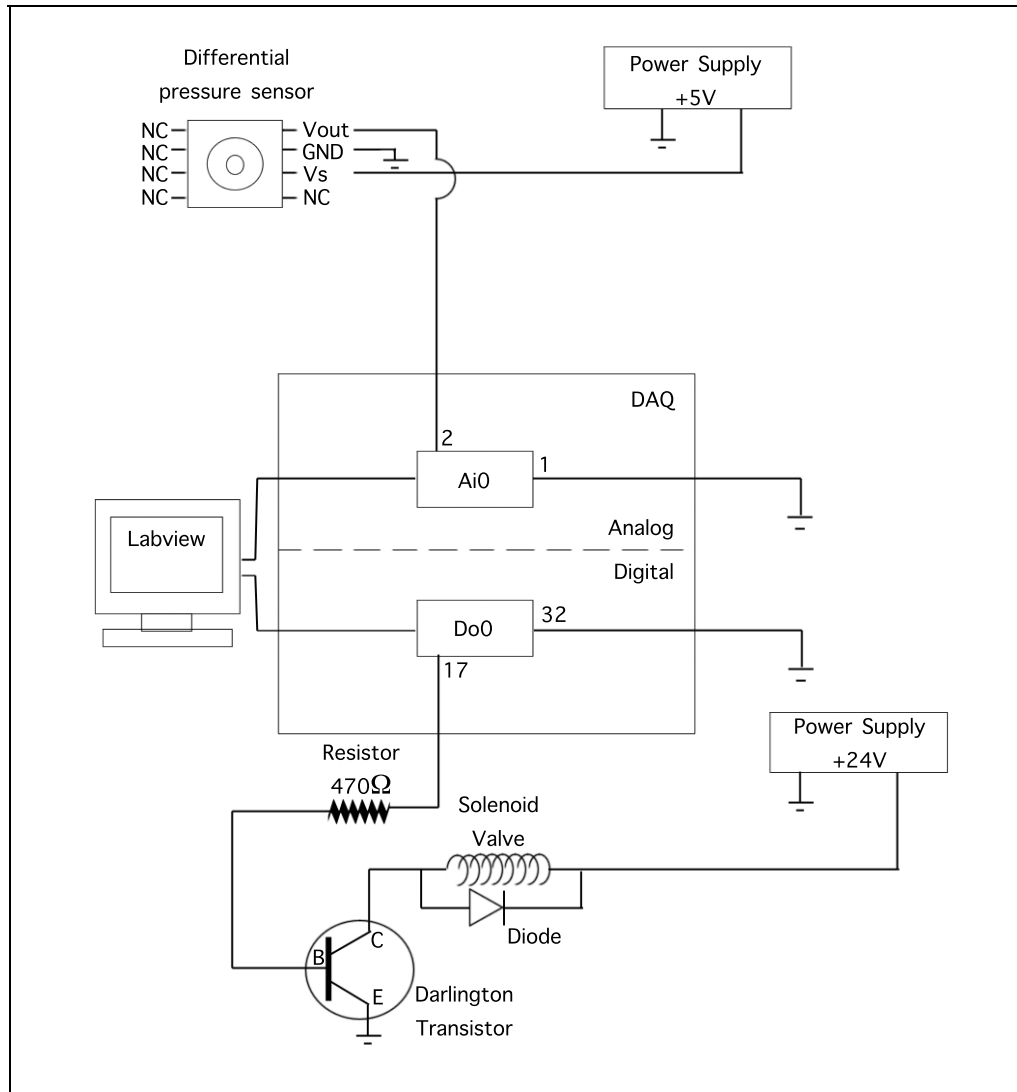


Figure 127: Circuit diagram of the experimental setup. The numbers at the data acquisition input and output are the input and output ports used. The data acquisition is done by means of a Texas Instruments DAQ, connected via USB to the computer. The resistor and transistor are implemented in order to be able to operate the solenoid valve.

APPENDIX 6 SENSOR DATA

Table 2: Operating Characteristics (VS = 5.0 Vdc, TA = 25°C unless otherwise noted, P1 > P2)					
Characteristic	Symbol	Min.	Typ.	Max.	Unit
Pressure Range	P _{OP}	0	-	6.0	kPa
				612	mm H ₂ O
Supply Voltage ¹	V _S	4.75	5.0	5.25	Vdc
Supply Current	I _S	-	-	10	mAdc
Full Scale Span ²	V _{FSS}	-	4.6	-	V
Offset ^{3,4}	V _{off}	0.152	0.265	0.378	V
Sensitivity	V/P	-	766	-	mV/kPa
			7.511		mV/mm H ₂ O
Accuracy ⁵	-	-	-	±2.46	%V _{FSS} with auto zero
				±5.0	%V _{FSS} without auto zero

[57]

¹ Device is ratiometric within this specified excitation range.

² Full Scale Span (V_{FSS}) is defined as the algebraic difference between the output voltage at full rated pressure and the output voltage at the minimum rated pressure.

³ Offset (V_{off}) is defined as the output voltage at the minimum rated pressure.

⁴ Auto Zero at Factory Installation: Due to the sensitivity of the MPXV4006, external mechanical stresses and mounting position can affect the zero pressure output reading. To obtain the 2.46% FSS accuracy, the device output must be "autozeroed" after installation. Autozeroing is defined as storing the zero pressure output reading and subtracting this from the device's output during normal operations. The specified accuracy assumes a maximum temperature change of ±5°C between autozero and measurement.

⁵ Accuracy (error budget) consists of the following:

Linearity: Output deviation from a straight-line relationship with pressure over the specified pressure range.

Temperature Hysteresis: Output deviation at any temperature within the operating temperature range, after the temperature is cycled to and from the minimum or maximum operating temperature points, with zero differential pressure applied.

Pressure Hysteresis: Output deviation at any pressure within the specified range, when this pressure is cycled to and from minimum or maximum rated pressure, at 25°C.

Offset Stability: Output deviation, after 1000 temperature cycles, -30 to 100°C, and 1.5 million pressure cycles, with minimum rated pressure applied.

TcSpan: Output deviation over the temperature range of 10° to 60°C, relative to 25°C.

TcOffset: Output deviation with minimum pressure applied, over the temperature range of 10° to 60°C, relative to 25°C.